Simulating charge transport near the passivated surface in LEGEND-200 HPGe detectors

Master Thesis in Physics

Samuel Hauser

Supervised by
Prof. Dr. Laura Baudis
Dr. Marta Babicz
Giovanna Saleh

June 25, 2026

Abstract

Neutrinoless double beta decay is a hypothetical lepton-number-violating process whose observation would provide evidence for physics beyond the Standard Model and establish that neutrinos are Majorana particles. The LEGEND experiment searches for this decay in ^{76}Ge using high-purity germanium (HPGe) detectors, which provide very good energy resolution and act simultaneously as source and detector. To reach the required sensitivity, a detailed understanding and suppression of backgrounds is essential, in particular through pulse shape discrimination. For this, pulse shape simulations are necessary.

In HPGe detectors, a passivated surface layer is added, separating the p+ and n+ contacts in order to reduce leakage currents. Charges moving through this region have a lower mobility compared to the transport in the bulk. When energy is deposited near the p+ contact the resulting electrons and holes may drift through this passivated surface, leading to delayed or incomplete charge collection and consequently a degraded signal. This is particularly relevant for α-induced background events, which originate at or near the p+ surface, resulting in charge clouds that propagate through the passivated region, thereby affecting pulse-shape characteristics and energy reconstruction.

Siggen is a simulation framework written in `C`, developed for field-calculations and pulse shape simulations (PSS) in HPGe detectors. EH-Drift is a siggen based simulation framework that allows the PSS of passivated surface events in HPGe detectors. However, waveform simulation is computationally expensive, requiring approximately 5 minutes per event on a GPU. In contrast, comparable signal generation in the Julia-based `SolidStateDetectors.jl` framework takes between 1 and 10 seconds, making SSD a promising alternative for large-scale simulation studies. In this work, we implemented the same conceptual approach in SSD as in EH-Drift. For various locations in the detector, close to the passivated surface as well as in the detector bulk, we compared between the two frameworks waveform residuals and their root mean square, the A/E parameter, defined as the maximum current amplitude divided by the deposited energy, and energy reconstruction, under the influence of different surface charge values. The studies were performed on a p-type point contact (PPC) detector and on an inverted coaxial point contact (ICPC) detector.

For the PPC detector, both frameworks reproduce the qualitative features of surface events, including slow pulse components, reduced charge collection, and suppressed A/E values near the passivated surface. However, sizeable quantitative differences remain close to the surface, mainly due to the different treatment of boundary conditions and the resulting electric field near the HPGe-LAr interface. For the inverted-coaxial point-contact detector, the agreement between the two frameworks is very good across the studied detector volume, however we were not able to reliably simulate events in the passivated surface.

Overall, SSD can reproduce the main qualitative behaviour of passivated-surface simulations known from EH-Drift. Remaining differences, especially for ICPC detectors, motivate further studies of boundary-condition modelling and validation with dedicated alpha-source measurements.

Acknowledgements

I want to thank the LEGEND group at the University of Zurich for their constant support throughout this project. Especially, I would like to thank Giovanna Saleh for her constant support with questions surrounding PSS, Dr. Marta Babicz for her guidance and giving feedback throughout the thesis, and all the other group members for giving helpful inputs in the sub-group meetings. I also want to thank Prof. Laura Baudis for giving me the opportunity to work on this exciting project and creating a welcoming atmosphere in the group. Further members of the LEGEND colaboration I especially want to thank are Dr. Felix Hagemann and Dr. David Hervaz Aguilar for giving me very helpful technical support with SSD, Prof. Julieta Gruszko and Dr. Kevin Bhimani with their explanations of EH-Drift and their inputs for surface modelling in EH-Drift. I also want to thank everybody who gave feedback in the Analysis calls.

Contents

List of Figures

List of Tables

Introduction

Neutrinos are elementary particles in the Standard Model that provide one of the clearest indications that the Standard Model is incomplete. In particular, it is still an open question whether neutrinos are Dirac particles, like the charged fermions, or Majorana particles, in which case the neutrino would be identical to its own antiparticle. Answering this question is one of the central goals of modern neutrino physics.

A particularly important experimental probe of the Majorana nature of neutrinos is the search for neutrinoless double beta decay. This hypothetical nuclear process violates lepton number by two units and would produce two electrons without the emission of neutrinos. Its observation would demonstrate that lepton number is not conserved and would establish that neutrinos are Majorana particles, or at least that lepton-number-violating physics exists. Neutrinoless double beta decay is therefore directly connected to fundamental questions about the origin of neutrino mass and the structure of physics beyond the Standard Model.

This thesis is situated in the context of the LEGEND experiment, which searches for neutrinoless double beta decay of ^{76}Ge using high-purity germanium detectors. These detectors act simultaneously as source and detector material, providing excellent energy resolution and high detection efficiency for events occurring inside the active detector volume. LEGEND-200 operates enriched germanium detectors in liquid argon and aims to strongly reduce the background level compared to previous germanium-based searches. LEGEND-1000 is planned as the next phase and pursues two main goals: increasing the active detector mass and further reducing the background level. Together, these improvements are intended to increase the half-life sensitivity to neutrinoless double beta decay in ^{76}Ge.

A central challenge in neutrinoless double beta decay searches is the suppression and understanding of backgrounds in the region of interest around the Q-value of ^{76}Ge. Since the expected signal rate is extremely small, even rare background processes can limit the sensitivity of the experiment. In LEGEND, several complementary background-rejection methods are used. One important method is pulse shape discrimination, which exploits the shape of the measured charge pulses. Different event classes can produce different pulse shapes depending on the position and topology of the energy deposition inside the detector.

Pulse shape discrimination requires a detailed understanding of charge transport in high-purity germanium detectors. When energy is deposited in the detector, electron-hole pairs are created and drift through the crystal under the influence of the electric field. Their motion induces a signal on the readout electrode. The resulting waveform depends on the detector geometry, impurity distribution, bias voltage, charge-cloud evolution, and the treatment of surfaces and contacts. Events close to passivated detector surfaces can experience modified drift conditions. This can lead to delayed or incomplete charge collection and therefore to pulse shapes that differ from those of events in the detector bulk.

Surface events are especially relevant for alpha-induced backgrounds. Alpha particles have a short range in germanium and therefore deposit their energy close to detector surfaces. If such events occur near the passivated surface, the resulting charge carriers may drift through regions of weak or distorted electric field. This can produce slow pulse components, degraded reconstructed energies, and altered pulse shape parameters. A reliable simulation of these events is therefore important for understanding alpha backgrounds and for interpreting pulse shape discrimination in LEGEND.

This thesis studies pulse shape simulations of events close to passivated surfaces in high-purity germanium detectors. The main goal is to compare simulations performed with `SolidStateDetectors.jl` (SSD) to simulations performed with EH-Drift, a framework used to describe passivated-surface charge transport. Both software are publicly available (link to SSD, link to EH-Drift) and free to use. As part of this work, a similar approach to surface-drift simulation as in EH-Drift was implemented in SSD. The comparison is carried out for detector geometries relevant to the LEGEND experiment, with particular emphasis on p-type point-contact detectors and inverted-coaxial point-contact detectors.

The comparison between SSD and EH-Drift is performed both at the level of detector simulation and at the level of pulse shape simulation. The detector simulation includes the calculation of the electric potential and electric field. This is important because the treatment of detector boundaries and dielectric interfaces can affect the electric field close to the passivated surface. The pulse shape comparison is based on simulated charge pulses and derived observables, including activeness (energy collection efficiency), the A/E parameter, defined as the ratio of maximum current amplitude and deposited energy, waveform residuals, and their root mean square.

The structure of this thesis is as follows.

Chapter 1 introduces the neutrino-physics context of the work, with emphasis on neutrino masses, Majorana neutrinos, and neutrinoless double beta decay. Chapter 2 describes the LEGEND experiment, focusing on LEGEND-200, the use of high-purity germanium detectors, the experimental setup, the electronics chain, and energy calibration. Chapter 3 discusses backgrounds in LEGEND-200 and introduces pulse shape discrimination, including relevant PSD parameters and the pulse shape signatures of different background classes, with emphasis on alpha backgrounds. Chapter 4 introduces pulse shape simulation and describes the physical and detector parameters that influence simulated waveforms. It also presents the two simulation frameworks used in this work, SSD and EH-Drift, and explains the implementation of passivated surface simulations in SSD. Chapter 5 describes the methodology used to compare SSD and EH-Drift, including the detector simulations, pulse shape simulations, and comparison observables. Chapter 6 presents the results of the studies performed. Finally, Chapter 7 summarizes the main findings and discusses possible future work, including validation with experimental surface-event data and further improvements of the surface-drift simulation model.

Chapter 1

Neutrino physics

1.1 Fermi's theory of the beta decay

In the late 1920s, the microscopic structure of matter was only partially understood. It was known that the electron and proton are constituents of the atom, but the internal structure of the atomic nucleus, and consequently the mechanisms that govern nuclear processes, were unclear. This lack of theoretical understanding became evident when James Chadwick studied nuclear beta decay in 1914. At the time, beta decay was assumed to be a two-body process in which a neutron transforms into a proton while emitting a single electron. In a nucleus with mass number $A = Z + N$ where Z and N denote the number of protons and neutrons, respectively, this process increases the proton number by one unit and can be written as:

$$(A, Z) \longrightarrow (A, Z + 1) + e^-$$

The assumption that this process was a two-body decay meant that the kinetic energy of the detected electrons would form a mono-energetic peak, as it would only carry the mass difference between daughter and mother nucleus. However, what was observed was a continuous spectrum. Nils Bohr tried to explain this anomaly by suggesting that energy conservation might have a statistical nature. In contrast, Wolfgang Pauli proposed in 1930 a third, undetected particle which later was called the neutrino. According to his hypothesis, this third particle would be emitted during the beta decay from the mother nucleus, together with the electron:

$$n \longrightarrow p + e^- + \bar{\nu}_e \tag{1.1.1}$$

A three-body decay would explain the continuous energy spectrum since the kinetic energy of the electron would not be fixed by the mass difference between mother and daugther nucleus anymore. Pauli's proposal of a third particle resolved the apparent violation of energy conservation, but did not yet provide a theory of the decay process. This step was taken by Enrico Fermi, who incorporated the neutrino into a quantitative description of beta decay.

In his theory, Fermi described beta decay as a point-like interaction between four fermions using creation and annihilation operators, without any mediating particles. In this theory, the amplitude for the beta decay is expressed in a vector-structure, meaning it does not violate parity [1]:

$$\mathcal{M} = \frac{G_F}{\sqrt{2}}(\bar{\psi_p}\gamma^\mu\psi_n)(\bar{\psi_e}\gamma_\mu\psi_{\bar{\nu}}) = \frac{G_F}{\sqrt{2}}\left(J^\mu_{\text{had}}J_{\mu,\text{lep}}\right) \tag{1.1.2}$$

In this expression $G_F \approx 1/(300\text{GeV})^2$ is the Fermi-constant, $\psi_{p,e,n,\bar{\nu}}$ denote the Dirac spinor fields describing the spin-1/2 fermions (proton, electron, neutron, and anti-neutrino), and γ^μ

are the Dirac gamma matrices that ensure a Lorentz-covariant coupling of the hadronic and leptonic currents J^{μ}_{had} and $J_{\mu,\text{lep}}$. The vector structure in equation 1.1.2 means that parity should be conserved in weak interactions, since a pure vector current is invariant under parity transformations. This turned out to be a problem later and will be addressed in section 1.2.

1.2 Parity violation and the chiral structure of the weak interaction

In the early 1950s, the so-called $\tau - \theta$ puzzle led physicists to believe that parity might not be conserved. Two identical, charged mesons, the τ and θ were observed to decay differently:

$$\tau^+ \longrightarrow \pi^+\pi^+\pi^- \rightarrow \text{odd parity}$$
$$\theta^+ \longrightarrow \pi^+\pi^0 \rightarrow \text{even parity}$$

This led Lee and Yang to propose an experiment, later conducted by Chieng-Shiung Wu, to study the decay of polarized ^{60}Co atoms. She placed the atoms in a magnetic field, such that their spins would be aligned. A strong asymmetry in the emission direction of the electrons emitted in the β^- decay was observed. In particular, significantly more electrons were emitted in the opposite direction of the ^{60}Co spin, which was strong evidence that parity is not conserved in weak interactions.

These experimental observations motivated physicists to reformulate Fermi's theory of the weak interaction [1]. Equation 1.1.2 was not compatible with these observations since it only contains a vector current. Feynman, Gell-Mann, Marshak and Sudarshan solved this issue by expressing the weak current as the sum of a vector and axial-vector current. This resulted in the following expression for the matrix element for the beta decay:

$$\mathcal{M} = \frac{G_F}{\sqrt{2}}[\bar{u}_p\gamma^\mu(g_V - g_A\gamma^5)u_n][\bar{u}_e\gamma_\mu(\mathbb{I} - \gamma_5)u_{\nu_e}] = \frac{4G_F}{\sqrt{2}}(V^\mu_{pn} - A^\mu_{pn})(V_{e\,\nu_e,\mu} - A_{e\,\nu_e,\mu}) \quad (1.2.1)$$

where in the last equality the projection operator $P_L = \frac{1}{2}(\mathbb{I} - \gamma^5)$ was used, to write the hadronic and leptonic interaction currents as a sum of vector and axial vector terms. In equation 1.2.1 g_V and g_A denote vector and axial-vector coupling constants, u_i ($\bar{u}_i$) the Dirac spinors for particle (anti-particle) i, V^μ the hadronic and leptonic vector currents, and A^μ the hadronic and leptonic axial vector currents. This theory predicts that electrons emitted in the β-decay of a nucleus are preferentially left-handed polarized, which is consistent with the experimental observations of Wu.

In the $V - A$ theory the charged weak current only couples to left-handed fermions and right-handed antifermions. In the minimal SM only left-handed neutrino fields ν_L are introduced but no right-handed antineutrinos $\bar{\nu}_R$. A Dirac mass term would require both chiralities; therefore, in the absence of a right-handed neutrino field, ν_R, a Dirac mass term of the following form is not possible:

$$\mathcal{L}^{\text{mass}}_{\text{Dirac}} = -m_D\bar{\nu}_L\nu_R + \text{h.c} \quad (1.2.2)$$

Furthermore, no gauge-symmetric Majorana mass term can be constructed. Consequently, no mass-term can be written in the minimal $V - A$ framework and neutrinos are therefore predicted to be massless.

The observation of neutrino oscillations, discussed in section 1.3, implies non-zero neutrino masses and therefore contradicts the prediction of this theory that neutrinos are massless. Thus, the existence of neutrino masses requires an extension of the minimal SM.

1.3 Neutrino oscillations

Motivated by the mixing of the neutral kaons, mixing of neutrino flavour states was proposed in 1957 by Bruno Pontecorvo. Neutrino mixing is described by expressing the flavour eigenstates $(\nu_e, \nu_\mu, \nu_\tau)$ as a linear combination of the mass eigenstates (ν_1, ν_2, ν_3) [2]:

$$|\nu_\alpha\rangle = \sum_{i=1}^{3} U_{i\alpha} |\nu_i\rangle \tag{1.3.1}$$

where U is the unitary Pontecorvo-Maki–Nakagawa–Sakata (PMNS) matrix. In the case of three neutrino flavours, the standard parametrization of this matrix is in terms of three mixing angles θ_{ij} and a CP-violating phase δ.

$$U = \begin{pmatrix} 1 & 0 & 0 \\ 0 & \cos\theta_{23} & \sin\theta_{23} \\ 0 & -\sin\theta_{23} & \cos\theta_{23} \end{pmatrix} \begin{pmatrix} \cos\theta_{13} & 0 & \sin\theta_{13}e^{-i\delta} \\ 0 & 1 & 0 \\ -\sin\theta_{13}e^{i\delta} & 0 & \cos\theta_{13} \end{pmatrix} \begin{pmatrix} \cos\theta_{12} & \sin\theta_{12} & 0 \\ -\sin\theta_{12} & \cos\theta_{12} & 0 \\ 0 & 0 & 1 \end{pmatrix} \tag{1.3.2}$$

The mixing angles θ_{ij} determine how strongly the flavour eigenstates are mixed into the mass eigenstates, and therefore determine the amplitude of the oscillation probability in equation 1.3.4. Under a CP transformation a particle is replaced by its antiparticle and U is replaced by its complex conjugate U^*. This means that terms in equation 1.3.2 that include $e^{\pm i\delta}$ change sign, which eventually leads to different oscillation probabilities for neutrinos and antineutrinos.

When solving the Schrödinger equation for relativistic neutrinos in the mass eigenbasis, the results are plane wave solutions:

$$|\nu_i(t)\rangle = e^{-iE_i \cdot t} |\nu_i\rangle \tag{1.3.3}$$

This means that each mass eigenstate propagates over time with a complex phase that depends on its energy $E_i = \sqrt{m_i^2 + |\boldsymbol{p}|^2}$. Using the unitarity of the PMNS matrix one can derive an expression for the probability that a neutrino travelling with energy E over a distance L from production, will change flavour from α to β. If only two neutrino flavours are considered, the oscillation probability can be approximated with the following expression:

$$P_{\alpha\to\beta}(L, E) = \sin^2(2\theta)\sin^2\left(1.27\frac{\Delta m^2 L}{E}\right) \tag{1.3.4}$$

where Δm^2 is given in eV^2, L in km, and E in GeV. According to this equation, the oscillation frequency between two flavours is determined by the neutrinos energy, the mass difference of the two neutrino flavours, and the length over which the neutrino beam propagates. Thus, neutrino oscillations can only be observed if at least two neutrino falvours have non-zero masses. Experiments that measure neutrino oscillations are not sensitive to the absolute masses, but only to their squared differences.

Experimentally, neutrino oscillations are studied by measuring the flux of different neutrino flavours, and comparing it to the expected flux under the assumption of no neutrino oscillations.

Neutrino oscillations can be observed in solar, atmospheric, reactor, and accelerator neutrinos, each sensitive to different parameters in the PMNS matrix in equation 1.3.2.

The values of the neutrino mixing angles are obtained from global fits to solar, atmospheric, reactor, and accelerator neutrino oscillation data. Since the neutrino mass ordering is not yet unambiguously established, table 1.1 lists the best-fit values for both normal ordering (NO) and inverted ordering (IO), following the NuFIT 6.0 global analysis [3].

Parameter [°]	Normal ordering	Inverted ordering
θ_{12}	$33.68^{+0.73}_{-0.70}$	$33.68^{+0.73}_{-0.70}$
θ_{13}	$8.52^{+0.11}_{-0.11}$	$8.58^{+0.11}_{-0.11}$
θ_{23}	$48.5^{+0.7}_{-0.9}$	$48.6^{+0.7}_{-0.9}$

Table 1.1: Best-fit values of the neutrino mixing angles with 1σ uncertainties from the NuFIT 6.0 global analysis for normal ordering and inverted ordering [3].

According to equation 1.3.4, the observation of neutrino oscillations is direct evidence that neutrinos must be massive. Oscillation experiments are only able to measure the squared mass differences Δm^2_{ij} between mass eigenstates i and j. Consequently, the sign of Δm_{ij} is unknown, which leads to two possible mass hierarchies, the normal and inverted ordering, where it can only be determined with certainty that $m_2 > m_1$:

- normal mass ordering: $m_1 < m_2 < m_3$
- inverted mass ordering: $m_3 < m_1 < m_2$

The T2K experiment reports the following 2π-periodic, 3σ confidence intervals on the CP-violating phase δ for the two different mass-orderings [4]:

- $\delta \in [-3.41, -0.03]$ assuming normal mass ordering
- $\delta \in [-2.54, -0.32]$ assuming inverted mass ordering

These intervals indicate a preference for values of δ away from at least one of the CP-conserving cases $\delta = 0$ and $\delta = \pi$, thereby hinting at CP violation in the lepton sector. In particular, the preferred region lies near $\delta \approx -\pi/2$ (which is equivalent to $3\pi/2$), where the magnitude of CP-violating effects is large.

1.3.1 Direct measurement of neutrino masses

Neutrino masses can be directly measured [5] through the differential rate of a charged-current process involving a neutrino, which depends on the neutrino mass through the kinematic phase space factor. In beta decay, for example, the electron energy spectrum near its endpoint is modified by the neutrino mass, since energy–momentum conservation requires the neutrino to carry at least its rest energy. As a result, the shape of the electron spectrum close to the endpoint depends on the neutrino mass squared. Because the electron flavour state is a superposition of mass eigenstates, the measured spectrum is a sum over contributions weighted by $|U_{ei}|^2$. Thus, experiments are sensitive to the effective neutrino mass,

$$m_\beta^2 = \sum_i |U_{ei}|^2 \, m_i^2, \tag{1.3.5}$$

which can be extracted from analysing the region at the right end of the beta spectrum.

The most stringent direct constraint on m_β is currently provided by the KATRIN experiment, which measures the endpoint region of the molecular tritium β-decay spectrum. From an analysis of 259 days of data, KATRIN obtains an upper limit

$$m_\beta < 0.45 \text{ eV} \tag{1.3.6}$$

at 90% confidence level [6]. This represents the strongest laboratory-based bound on the effective electron-neutrino mass to date.

1.4 Neutrino detection

Neutrinos are detected via weak interactions, most prominently inverse beta decay (IBD) and elastic scattering processes. In IBD, an electron antineutrino interacts with a proton to produce a neutron and a positron, provided the neutrino energy exceeds a threshold of about 1.8 MeV [7]. Despite its small cross-section, this channel enabled the first experimental neutrino detection by Cowan and Reines using reactor antineutrinos, where the positron annihilation signal was observed via scintillation light.

Elastic scattering provides an alternative detection method through charged and neutral current interactions. In charged current interactions, the neutrino converts into its corresponding charged lepton, which can be detected directly. Experiments such as Borexino exploit this process by observing scintillation light from recoiling electrons, allowing precise measurements of solar neutrinos.

In neutral current interactions, the neutrino scatters off a target without changing flavor, transferring energy to the recoiling particle. A notable example is coherent elastic neutrino–nucleus scattering (CEνNS), where the neutrino interacts with the entire nucleus. Due to the very small recoil energies involved, such measurements require highly sensitive, low-background detectors. This process was first observed by the COHERENT collaboration in 2017 using a pion-decay neutrino source and scintillation detectors [8]. In 2024 the XENON collaboration observed ^{8}B neutrinos through CEνNS with the XENONnt experiment [9].

1.5 Neutrinoless double beta decay ($0\nu\beta\beta$)

1.5.1 Neutrino masses beyond the Standard Model

Because the minimal Standard Model contains only left-handed neutrino fields, the theory predicts massless neutrinos, as discussed in section 1.2. The observation of neutrino oscillations therefore requires an extension of the Standard Model, for which two possibilities exist [2]: If right-handed neutrino singlets are added, neutrinos can acquire Dirac masses through Yukawa couplings to the Higgs field. Alternatively, neutrinos may be Majorana particles, allowing lepton-number-violating mass terms.

To see how a neutrino mass could arise, consider the Dirac mass term for a fermion field

$$\mathcal{L}^D_{\text{mass}} = -m\bar{\nu}\nu. \tag{1.5.1}$$

Expressing the field in terms of its chiral components ν_L and ν_R gives

$$\mathcal{L}^D_{\text{mass}} = -m(\bar{\nu}_R\nu_L + \bar{\nu}_L\nu_R). \tag{1.5.2}$$

This expression shows explicitly that a Dirac mass term requires both left-handed and right-handed fields. In the minimal Standard Model, however, only the left-handed neutrino field ν_L is present. Consequently, a Dirac mass term cannot be constructed unless a right-handed neutrino field ν_R is introduced.

An alternative possibility is that neutrinos are Majorana particles, in which case the neutrino field is identical to its charge-conjugated field. A mass term can then be constructed using only left-handed fields by coupling the field to its charge conjugate $\nu_L^C = C\overline{\nu_L}^T$:

$$\mathcal{L}_{\text{mass}}^M = -\frac{1}{2} m \overline{\nu_L^C} \nu_L + \text{H.c.} \tag{1.5.3}$$

The lepton-number properties of the two mass terms can be seen from their behaviour under a global lepton-number transformation. A neutrino field with lepton number $L = 1$ transforms as $\nu_{L,R} \to e^{i\phi}\nu_{L,R}$, while its adjoint transforms as $\overline{\nu}_{L,R} \to e^{-i\phi}\overline{\nu}_{L,R}$. Therefore, the Dirac mass term conserves lepton number:

$$\overline{\nu_R}\nu_L \to e^{-i\phi}e^{i\phi}\overline{\nu_R}\nu_L = \overline{\nu_R}\nu_L,$$

For the Majorana term, however, the charge-conjugated field carries the opposite lepton number, $\nu_L^C \to e^{-i\phi}\nu_L^C$, so that $\overline{\nu_L^C} \to e^{i\phi}\overline{\nu_L^C}$. The Majorana mass term therefore transforms as

$$\overline{\nu_L^C}\nu_L \to e^{2i\phi}\overline{\nu_L^C}\nu_L.$$

and is not invariant under lepton-number transformations. It therefore violates total lepton number by two units, in contrast to a Dirac mass term.

If neutrinos are Majorana particles, the neutrino fields cannot be rephased freely, since such phase redefinitions would change the Majorana mass term. As a result, not all complex phases in the lepton mixing matrix can be absorbed into the field definitions. Compared to the Dirac case, two additional physical phases remain for three neutrino generations. The PMNS matrix then contains, in addition to the three mixing angles and the Dirac CP-violating phase δ, two Majorana phases, usually denoted by α_{21} and α_{31}. It can be parametrized as [10]:

$$V = U \cdot \text{diag}\Big(1, e^{i\alpha_{21}/2} e^{i\alpha_{31}/2}\Big), \tag{1.5.4}$$

where U denotes the standard PMNS matrix given in equation 1.3.2. Unlike the Dirac phase, the Majorana phases do not enter neutrino oscillation probabilities. However, they do contribute to the effective Majorana mass

$$m_{\beta\beta} = \left| \sum_i U_{ei}^2 m_i \right|. \tag{1.5.5}$$

which is relevant for neutrinoless double beta decay. Depending on the values of α_{21} and α_{31}, the individual mass-eigenstate contributions can interfere constructively or destructively. As a result, the value of $m_{\beta\beta}$ may be enhanced or partially cancelled even for fixed neutrino masses and mixing angles.

1.5.2 Two neutrino double beta decay

Double beta decay is a rare nuclear transition in which the charge of a nucleus changes by two units while the mass number remains unchanged. Double β^- decay, in which two neutrons are transformed into two protons, can occur in certain nuclei for which the corresponding single β^- decay is energetically forbidden.

The origin of this behaviour can be understood from the nuclear mass parabola at fixed mass number A. For a given nucleus, the proton number is Z and the neutron number is $N = A - Z$.

Nuclei with even Z and even N are referred to as even-even nuclei, whereas nuclei with odd Z and odd N are called odd-odd nuclei. Even-even nuclei are more strongly bound because nucleons tend to form pairs, while odd-odd nuclei contain one unpaired proton and one unpaired neutron and are therefore less strongly bound. In terms of the binding energy $B(A, Z)$, this means that even-even nuclei have a larger binding energy than their neighboring odd-odd isobars. Since the nuclear mass is related to the binding energy through

$$M(A, Z) \sim Zm_p + Nm_n - B(A, Z),$$

a larger binding energy corresponds to a lower nuclear mass. As a consequence, for even A the isobars split into two branches: a lower branch formed by the even-even nuclei and an upper branch formed by the odd-odd nuclei.

This splitting has important consequences for beta decay. A single β^- decay changes the proton number by one unit,

$$(A, Z) \to (A, Z + 1)$$

and is only possible if the daughter nucleus has a lower mass than the parent nucleus. For certain even-even nuclei, however, the neighboring odd-odd nucleus lies higher in mass,

$$M(A, Z + 1) > M(A, Z)$$

so that single β^- decay is energetically forbidden. At the same time, the next even-even isobar may lie lower in mass,

$$M(A, Z + 2) < M(A, Z)$$

which makes a transition with $\Delta Z = 2$ energetically allowed. In that case, the nucleus cannot decay through a single β^- transition to the intermediate odd-odd nucleus, but it can undergo double β^- decay to the next even-even nucleus:

$$(A, Z) \to (A, Z + 2) + 2e^- + 2\bar{\nu}_e \tag{1.5.6}$$

This situation is illustrated by the mass parabola in figure 1.1, which shows the approximate quadratic dependence of the nuclear mass on Z for fixed A and the separation into an even-even and an odd-odd branch due to pairing.

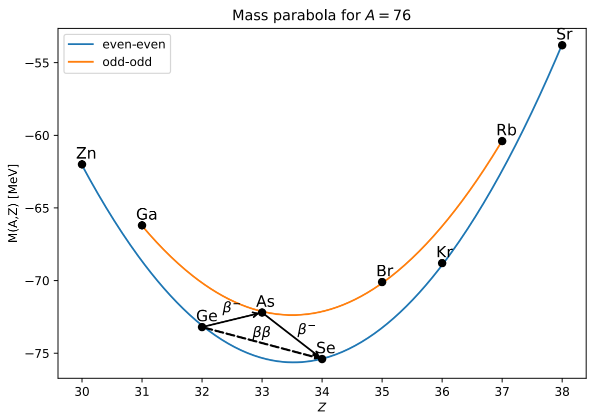

Figure 1.1: Schematic mass parabola for fixed mass number $A = 76$, illustrating how the pairing term splits the isobars into an even-even and an odd-odd branch. For suitable nuclei, single β^- decay to the intermediate odd-odd nucleus is energetically forbidden, while double beta decay to the next even-even nucleus is allowed. Figure adapted from [11].

The decay described by equation 1.5.6 is referred to as two-neutrino double beta decay ($2\nu\beta\beta$) and allowed within the SM. This process conserves total lepton number and can be viewed as a second-order weak process involving two simultaneous beta decays inside the nucleus. Because two weak vertices are involved, the decay rate is strongly suppressed and the half-lives are extremely long, typically in the range 10^{18}–10^{24} yr depending on the isotope. For ^{76}Ge, for example, the most precise half-life measurement yields a value of $T^{2\nu}_{1/2} = (2.022 \pm 0.018_{\text{stat}} \pm 0.038_{\text{syst}}) \times 10^{21}$ yr [12].

Neglecting the nuclear recoil, the total energy released in the decay is given by the difference of the atomic masses of the initial and final states:

$$Q_{\beta\beta} = M_{\text{atom}}(A, Z) - M_{\text{atom}}(A, Z + 2) \tag{1.5.7}$$

In $2\nu\beta\beta$ decay, this energy is shared among the two electrons and the two antineutrinos. Thus, measuring the kinetic energies of the emitted electrons yields a continuous spectrum.

1.5.3 Neutrinoless double-beta decay

If no neutrinos are emitted in $\beta\beta$ decay, the process is called neutrinoless double beta decay ($0\nu\beta\beta$ decay):

$$(A, Z) \to (A, Z + 2) + 2e^- \tag{1.5.8}$$

The observation of this decay would have the following implications: First, it would demonstrate that lepton number is not conserved. In the Standard Model, leptons are assigned a conserved quantum number L, with $L = +1$ for electrons and neutrinos and $L = -1$ for their antiparticles. The initial nuclear state in equation 1.5.8 carries no leptons and thus has total lepton number $L = 0$, while the final state contains two electrons with total lepton number $L = 2$. The process therefore violates lepton number conservation by two units ($\Delta L = 2$) and cannot occur within the Standard Model.

Second, according to the Schechter-Valle theorem [13], the observation of $0\nu\beta\beta$ decay would imply that neutrinos possess a Majorana mass term, i.e. that neutrinos are Majorana fermions.

The simplest and most commonly discussed mechanism for $0\nu\beta\beta$ decay is the exchange of light Majorana neutrinos between two standard weak-interaction vertices. In this case, the decay amplitude is proportional to $m_{\beta\beta}$. Other mechanisms are also possible in theories beyond the Standard Model, for example heavy Majorana neutrino exchange [14], right-handed weak currents [15], or supersymmetric contributions [16].

The Feynman diagrams in figure 1.2 illustrate why the Majorana nature of neutrinos is required in the light-neutrino exchange picture. At one weak-interaction vertex, an antineutrino is emitted together with an electron. For the process to proceed without neutrinos in the final state, this particle must be reabsorbed at the second vertex as a neutrino. This is only possible if neutrino and antineutrino are identical, i.e. if the neutrino is a Majorana particle.

In addition, the weak interaction couples predominantly to left-handed chirality states. The neutrino emitted at the first vertex is predominantly right-handed in helicity (since it is an antineutrino), whereas the neutrino absorbed at the second vertex must be left-handed. This requires a helicity flip in the virtual neutrino propagator, introducing a suppression proportional to the neutrino mass. This suppression is one reason why the expected $0\nu\beta\beta$ decay half-life is much longer than the corresponding $2\nu\beta\beta$ decay half-life.

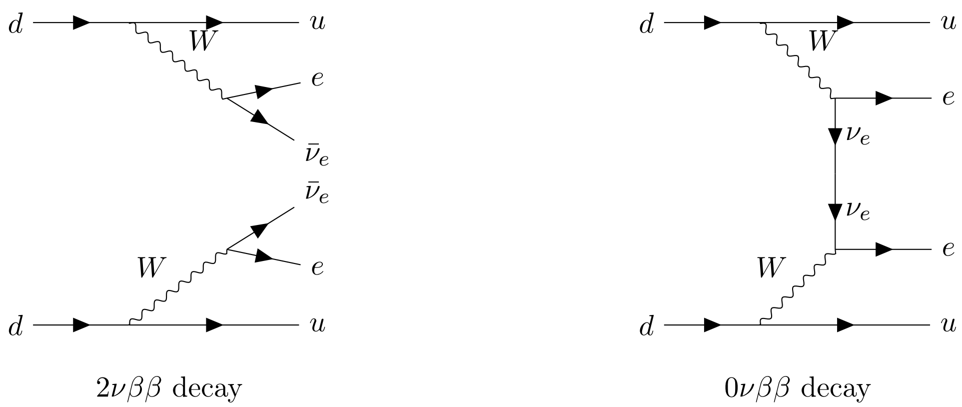

Figure 1.2: Comparison of double beta decay modes. Left: standard two-neutrino double beta decay ($2\nu\beta\beta$ decay), allowed in the Standard Model. Right: neutrinoless double beta decay ($0\nu\beta\beta$ decay), which requires Majorana neutrinos.

If the decay is mediated by light Majorana neutrino exchange, the relevant lepton-number-violating parameter is the effective Majorana mass $m_{\beta\beta}$ (equation 1.5.5). It characterizes the strength with which Majorana neutrino masses contribute to $0\nu\beta\beta$ decay. In this case, the half-life can be written as

$$\left(T_{1/2}^{0\nu}\right)^{-1} = G_{0\nu}\,|M_{0\nu}|^2\,\frac{|m_{\beta\beta}|^2}{m_e^2}, \tag{1.5.9}$$

where $G_{0\nu}$ is the phase-space factor and $M_{0\nu}$ is the nuclear matrix element. Because $m_{\beta\beta}$ is expected to be very small, the decay rate is strongly suppressed, leading to predicted half-lives typically above 10^{25} yr.

The dominant theoretical uncertainty in extracting a value for $m_{\beta\beta}$ from a measured $0\nu\beta\beta$ decay half-life arises from the nuclear matrix element $M_{0\nu}$. In contrast to the phase-space factor $G_{0\nu}$, which can be calculated rather precisely, present nuclear-structure calculations still show a spread of a factor of 2–3 in $M_{0\nu}$ [17, 18].

Equation 1.5.9 shows how $0\nu\beta\beta$ decay can provide information on the absolute neutrino mass scale: a measurement of the half-life, or a lower limit on it, can be translated into a value or upper bound on the effective Majorana mass $m_{\beta\beta}$. Since $m_{\beta\beta}$ depends on the neutrino masses m_i themselves, rather than only on the mass-squared differences measured in oscillation experiments, $0\nu\beta\beta$ decay is sensitive to the absolute neutrino mass scale.

1.5.4 Experimental searches

Experimental searches for neutrinoless double beta decay aim to detect the two electrons emitted in the decay and to reconstruct their summed kinetic energy. In contrast to $2\nu\beta\beta$ decay, where the energy is shared with two neutrinos, the absence of neutrinos in the final state implies that the full decay energy $Q_{\beta\beta}$ is carried by the electrons. Consequently, $0\nu\beta\beta$ decay would manifest itself as a monoenergetic peak in the summed electron energy spectrum at $Q_{\beta\beta}$.

Most experimental approaches search for this peak by measuring the total deposited energy of the event. In tracking experiments such as SuperNEMO, however, the two outgoing electrons can also be reconstructed individually, allowing their separate tracks and energies to be measured [19]. Tracking experiments are mentioned here for completeness, but will not be further discussed in this work.

The sensitivity of an experiment is commonly expressed in terms of the half-life $T^{0\nu}_{1/2}$. If a signal is observed, the measured event rate allows the determination of the half-life and, through equation 1.5.9, the extraction of the effective Majorana mass $m_{\beta\beta}$. In the absence of a signal, a lower limit on the half-life can be derived from the experimental exposure.

The experimental sensitivity depends on the exposure $M \cdot t$, where M is the detector mass and t the measurement time, as well as on the detection efficiency ε, the isotopic abundance a, and the background level B. In the ideal case of a background-free experiment, the sensitivity scales linearly with exposure, whereas in the background-dominated regime it scales only with the square root of the exposure:

$$T^{0\nu}_{1/2} \propto a \cdot \varepsilon \cdot \begin{cases} M \cdot t & \text{background-free} \\ \sqrt{\frac{M \cdot t}{B \cdot \Delta E}} & \text{with background} \end{cases} \tag{1.5.10}$$

where ΔE denotes the energy resolution of the detector. This shows the importance of achieving both large detector masses and extremely low background levels in $0\nu\beta\beta$ decay experiments. Thus, it is advantageous to operate in a background-free regime, where the sensitivity improves linearly with exposure.

A key requirement for a suitable isotope is that single β decay is energetically forbidden, while double beta decay is allowed. Typical isotopes used in current experiments include ^{76}Ge, ^{136}Xe, and ^{130}Te, which combine relatively large $Q_{\beta\beta}$ values with favorable nuclear properties.

A variety of experimental approaches are currently pursued, differing in detector technology, target isotope, and scalability. The most competitive limits on the half-life of neutrinoless double beta decay have been obtained in experiments using ^{76}Ge ^{136}Xe, and ^{130}Te providing complementary sensitivity. A comparison of representative results is given in Table 1.2.

Isotope	Experiment	$T^{0\nu}_{1/2}$ limit [yr]
^{76}Ge	GERDA Phase II [12]	$> 1.8 \times 10^{26}$
^{76}Ge	Majorana Demonstrator [20]	$> 8.3 \times 10^{25}$
^{136}Xe	EXO-200 [21]	$> 3.5 \times 10^{25}$
^{136}Xe	KamLAND-Zen [22]	$> 1.9 \times 10^{25}$
^{130}Te	CUORE [23]	$> 3.2 \times 10^{25}$

Table 1.2: Lower limits (90% confidence level) on the half-life of neutrinoless double beta decay for different isotopes. For CUORE a 90% Bayesian credible interval is quoted.

The results show that experiments using ^{76}Ge and ^{136}Xe currently provide the most stringent constraints, reaching sensitivities at the level of 10^{26} yr. While xenon-based experiments benefit from large target masses and scalability, germanium-based experiments achieve superior energy resolution and extremely low background levels, allowing operation close to the background-free regime.

The $2\nu\beta\beta$ decay produces a continuous summed electron energy spectrum extending up to $Q_{\beta\beta}$, but the spectrum is strongly suppressed near the endpoint. Owing to the excellent energy resolution of high-purity germanium (HPGe) detectors (of order 0.1% at $Q_{\beta\beta}$), only a fraction of $\sim 10^{-14}$ of $2\nu\beta\beta$ events fall into the 3σ region around $Q_{\beta\beta}$ [24]. Consequently, $2\nu\beta\beta$ decay does not significantly limit the sensitivity.

Further advantages of ^{76}Ge-based experiments include:

- the possibility to use the detector material simultaneously as source and detector, leading to high detection efficiency

- good radiopurity of HPGe crystals
- powerful background rejection through pulse shape discrimination
- the ability to achieve a low background index

These properties make ^{76}Ge one of the most favorable isotopes for high-resolution, low-background searches for $0\nu\beta\beta$ decay.

Building on the success of previous germanium-based experiments such as GERDA and the Majorana Demonstrator, the next generation of searches aims to significantly increase the detector mass while maintaining ultra-low background conditions. The Large Enriched Germanium Experiment (LEGEND) follows this strategy by combining large exposure with the excellent energy resolution and background suppression capabilities of HPGe detectors.

LEGEND is designed to operate in or near the background-free regime over its target exposure, thereby enabling a substantial improvement in sensitivity to the half-life of neutrinoless double beta decay in ^{76}Ge. This approach directly exploits the advantages of germanium detectors.

A central challenge for $0\nu\beta\beta$ experiments is the suppression of radioactive backgrounds, which can mimic or obscure the signal in the region of interest around $Q_{\beta\beta}$. In particular, α- and β-induced surface events, as well as γ interactions in the detector material and surrounding components, can contribute to the background level B. Achieving operation in the background-free regime therefore requires not only material radiopurity and shielding, but also powerful event discrimination techniques. In HPGe detectors, this is achieved through pulse shape discrimination (PSD, cf. chapter 3), which relies on the fact that different energy deposition topologies lead to characteristic differences in the measured signal shapes. The resulting differences in the shape of the detector signals allow for an efficient separation of signal-like and background-like events. The development and optimization of such pulse shape discrimination methods rely on a detailed understanding of the underlying signal formation processes. Pulse shape simulations (PSS, cf. chapter 4) provide a framework to model these processes and to predict the detector response for different event topologies. Such simulations are therefore an essential tool for the development and validation of PSD techniques and form the basis for the studies presented in this work.

Chapter 2

The LEGEND experiment

The Large Enriched Germanium Experiment for neutrinoless $\beta\beta$ decay (LEGEND) is a global collaboration that uses High Purity Germanium (HPGe) detectors, enrichted to about 90%, both as a source and detector, to search for $0\nu\beta\beta$ decay. In particular it aims at detecting the two emitted electrons in the hypothetical $0\nu\beta\beta$ decay in ^{76}Ge:

$$^{76}\mathrm{Ge} \longrightarrow ^{76}\mathrm{Se} + 2e^{-}. \tag{2.0.1}$$

The project consists of two stages: The first stage, LEGEND-200, aims to deploy 200 kg of detector material and started taking data in early 2023 and will be the focus in this work. The second stage, LEGEND-1000, aims to use 1000 kg of detector material and is planned to start in the early 2030s.

2.1 Experimental setup

The experiment is located at the Gran Sasso National Laboratories (LNGS) in Assergi, Italy. LNGS is an underground research center, where the surrounding rock shields against cosmic muons. The experimental setup is shown in Figure 2.1. The HPGe detectors are arranged in vertical strings inside a tank filled with $64\,\mathrm{m}^3$ of liquid argon (LAr) acting as a shield and, together with silicon photomultipliers (SiPMs), as a veto. The experiment operates at a temperature of 78 K to reduce electronics noise and thermal effects of charge carriers inside the detector.

The LAr cryostat is located inside a tank filled with $590\,\mathrm{m}^3$ of radiopure water to shield against neutrons and external γ radiation originating from the surrounding rock. In addition, the water tank is used as a Cherenkov medium which can detect muons with the help of 66 PMTs, acting as a veto.

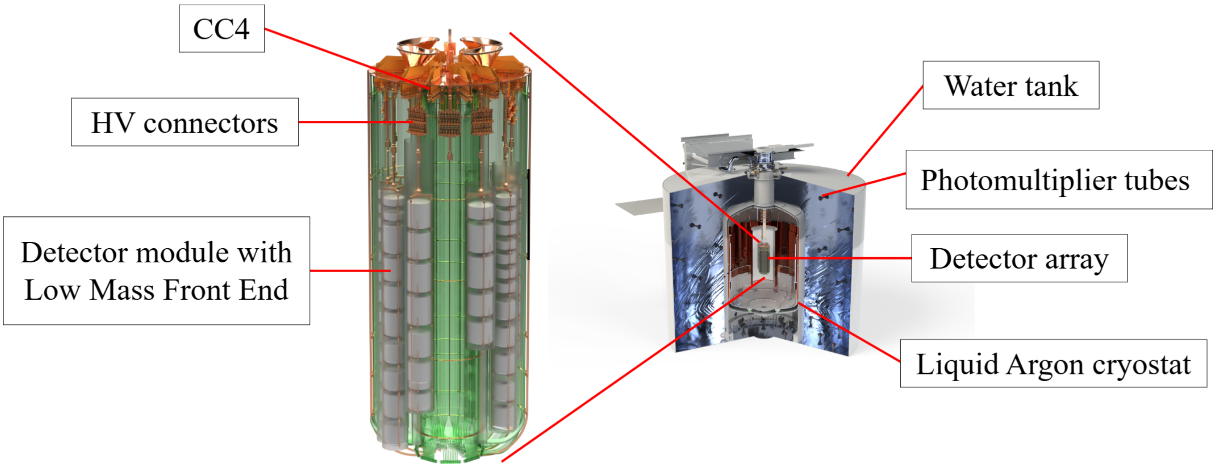

Figure 2.1: Experimental setup of LEGEND-200. The water cherenkov tank is used for muon veto, and it surrounds the cryostat filled with LAr. In the center are the arrays of detector modules. Figure taken from [25] and modified.

2.1.1 Liquid argon veto

The detector arrays are inside the LAr cryostat, surrounded by wavelength shifting reflectors (WLSR). The LAr serves three purposes:

1. As a refrigerant, which is important for the operating conditions
2. Shielding against background
3. Acting as a scintillation medium

The latter allows to identify γ backgrounds and acts as a veto for background rejection.

When radiation deposits energy in the LAr it ionizes some of the atoms, which produces scintillation light with a wavelength of 128 nm. Since the SiPMs are not able to directly detect this light, the WLSR absorb it and re-emit it at a wavelength of 450 nm making it detectable by the SiPMs. Thus, only scintillation light created between the detector array and the WLSR can be detected. A conceptual illustration of the WLSR is shown in figure 2.2

The SiPMs are located near the detector array where they detect the light emitted by the WLSR. A temporal coincidence between the signal in the germanium detectors and the scintillation in the surrounding LAr indicates that energy was both deposited inside and outside the detector and can therefore not be a $0\nu\beta\beta$ decay.

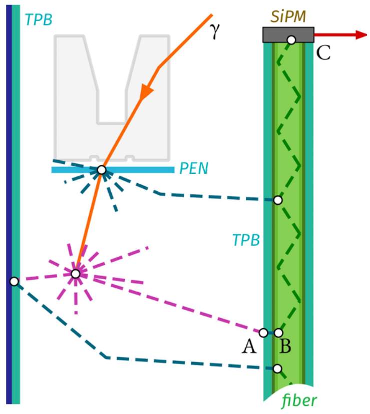

Figure 2.2: Schematic illustration of the wavelength-shifting reflectors used in the liquid argon veto. Scintillation light produced in LAr at 128 nm is absorbed by the wavelength-shifting material and re-emitted at longer wavelengths (around 450 nm), making it detectable by the SiPMs. Figure from [26].

2.1.2 Muon veto

Thanks to the underground location of the experiment, comsic muons are suppressed by a factor of 10^6 [27]. When residual cosmic muons travel through the water tank that surrounds the cryostat, they emit Cherenkov light, which is detected by the PMTs mounted to the inner walls of the water tank.

If, within a time interval of $\pm 1.75\,\mu$s, a signal is temporally coincident with a muon signal from the PMTs it will be flagged and removed in the data analysis [28]. The efficiency of this technique was demonstrated in GERDA, where a muon rejection efficiency of $> 99.99\,\%$ was achieved [29].

2.2 Germanium detectors

Germanium-76 is a stable isotope where $2\nu\beta\beta$ decay can occur. Since ordinary beta decay is kinematically forbidden and the decay has a $Q_{\beta\beta}$ value of 2039 keV, it is a suitable isotope for the search for $0\nu\beta\beta$ decay. This comparatively high Q-value lies above many prominent natural radioactive backgrounds and defines the endpoint of the continuous $2\nu\beta\beta$ decay spectrum, which falls steeply near $Q_{\beta\beta}$. As a result, a $0\nu\beta\beta$ decay signal would appear as a monoenergetic peak at $Q_{\beta\beta}$. Due to the excellent energy resolution of HPGe detectors, about 0.1% at $Q_{\beta\beta}$ [27], the strongly suppressed endpoint tail of the $2\nu\beta\beta$ spectrum gives a negligible contribution in the region of interest, as discussed in Section 1.5.4

Apart from being used as a source of double beta decays, the germanium crystals serve as detector due to their semiconductor properties, which are elaborated here:
By adding doping atoms to the semiconductor, the conductivity can be controlled. If doping atoms are added that have one less valence electron than germanium (such as boron), this creates a vacancy in the crystal structure, called hole. These holes behave like positively charged particles and can freely move in the semiconductor. Such a semiconductor is called p-type.
If a doping atom with one additional valence electron is added to the semiconductor, the excess electron can freely move and the semiconductor is called n-type.

By joinging a p- and n-type semiconductor a pn junction is created. Initially, the two regions are electrically neutral. Electrons diffuse from the n-type to the p-type region, and holes from the p-type to the n-type region. Around the region where the two semiconductor types are in contact an electric field is created which opposes the exchange of charge carriers. The charge carrier exchange proceeds up to the point where the created electric field exactly counteracts the diffusion and an equilibrium is formed. As a result, a region free of mobile charge carriers is created around the junction, called depletion region. The magnitude of the created electric field as well as the width of the depletion region depend on the impurity concentration used to form the two semiconductor types.

By further applying a bias voltage to the pn junction, one can control the flow of charge carriers across the contact zone, and therefore the potential difference across the depletion zone and its width. A schematic of a pn-junction and the dependence of the depletion width on applied bias voltage is depicted in figure 2.3.

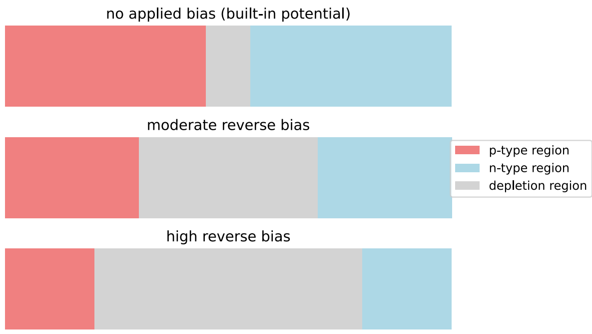

Figure 2.3: Schematic of a pn-junction operated under reverse bias showing the depletion width for different levels of applied voltages.

If a positive bias voltage is applied to the n-type material and a negative or zero voltage to the p-type material, the pn-junction is said to be operated under reverse bias. In this case the depletion zone and voltage increase with the applied bias voltage. If the detector is fully depleted, no charge carriers flow between p- and n-type regions.

2.2.1 HPGe detector production for LEGEND

The HPGe detectors used in LEGEND are produced with the Czochralski-method [30]. A small crystal seed is inserted in a heat resistant container, called crucible, and heated above the melting point of Ge, resulting in a homogeneous liquid. A crystal seed with known crystallographic orientation is placed on the melt and the crystal is slowly pulled upwards while rotating. The molten atoms at the interface between the seed and the molt solidify and adopt the same crystal structure as the crystal seed. The final crystal has a homogeneous crystal structure rather than random orientations. A schematic of the procedure is depicted in Figure 2.4.

The bulk of an HPGe detector consists of nearly intrinsic germanium with a very small concentration of electrically active residual impurities, of the order of ($10^{10}\,\mathrm{cm}^{-3}$). The net impurity concentration determines whether the material is effectively p-type or n-type. During crystal growth, the incorporation and segregation of these residual impurities leads to a spatially non-uniform impurity profile, which is often approximated by a variation along the crystal-growth direction. This impurity profile significantly affects the depletion voltage and the electric-field distribution inside the semiconductor.

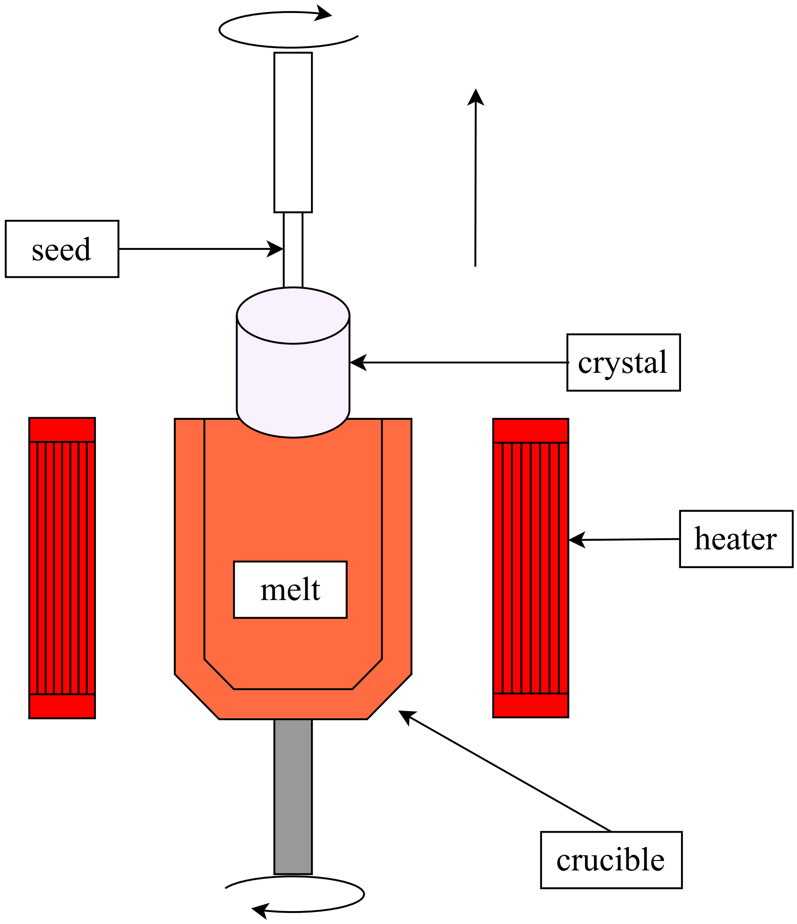

Figure 2.4: Schematic of the Czochraslki method, used in LEGEND to produce HPGe detectors. Figure adapted from [30].

The final, cylindrical crystals are then cut to produce one or more detector per crystal with various geometries. Afterwards, n+ and p+ contacts are added to create a diode structure so that an external bias voltage can be applied. The n+ contact is typically created by lithium diffusion and the p+ contact by boron implantation. Further applying a reverse bias voltage to the detector depletes the bulk of the detector of mobile charge carriers, which is crucial for the operation of HPGe detectors.

In LEGEND-200, several detector geometries are employed that are optimized for low-background operation and pulse shape discrimination. These include Broad Energy Germanium (BEGe) detectors, coaxial detectors, Inverted Coaxial Point Contact (ICPC), and p-type point contact (PPC) detectors. While coaxial detectors represent an earlier design with larger volumes, newer geometries such as BEGe and ICPC detectors are based on a point-contact configuration, which leads to strongly non-uniform electric fields and characteristic signal formation properties that are advantageous for background discrimination. BEGe detectors are relatively small and provide excellent energy resolution and pulse shape discrimination performance, whereas ICPC detectors allow for significantly larger detector masses while retaining similar signal characteristics.

2.2.2 P-type point contact (PPC) and inverted coaxial point contact (ICPC) detectors

In this section two detector geometries are discussed in detail, namely PPC and ICPC detectors, as they will be subject to the studies performed in this thesis. Their geometries are depicted in figure 2.5.

PPC detectors produced by Ortec

The geometry of Ortec PPC detectors consists of a cylinder stacked on top of a cone-shaped taper, and have a radius of $\sim 30\,\mathrm{mm}$ and height of $\sim 50\,\mathrm{mm}$. The n+ contact, which is $1-2\,\mathrm{mm}$ thick, surrounds the detector on the walls and the top. The p+ point contact has an approximately cylindrical shape with a radius of $\sim$ 1 mm and a height of $\sim 2\,\mathrm{mm}$. It is located at the center of the bottom plane. Since PPC detectors operate under reverse bias the voltage (typically between 1000 and 3000 V) is applied to the n+ contact, while the p+, where the signal is read out, is grounded.
At the bottom area between the p+ and n+ contact a passivation layer is added, usually made from non-crystalline amorphous germanium. This is done to prevent leakage current, i.e. charges moving fromt the n+ to the p+ contact.

ICPC detectors produced by Mirion

In LEGEND-1000 only ICPC detectors will be deployed, because their signals are better suited for analysis (cf. chapter 3). ICPC detectors are made of a p-type semiconductor, which, similarly to the PPC, has a $1-2$ mm thick n+ contact coating around the surface. At the bottom center the grounded p+ contact is located, whose dimensions vary significantly between each detector: its radius is between 1 and 12 mm, depending on the specific detector. A bias voltage of 2000 - 3000 V is applied to the n+ contact.
They typically have a diameter and height of around 80 mm. A large hole in the upper part, which varies in shape from detector to detector, extends into the bulk for around 40 mm. A circular ditch around the p+ contact, in addition to a passivated surface, mitigate the risk of leakage current.

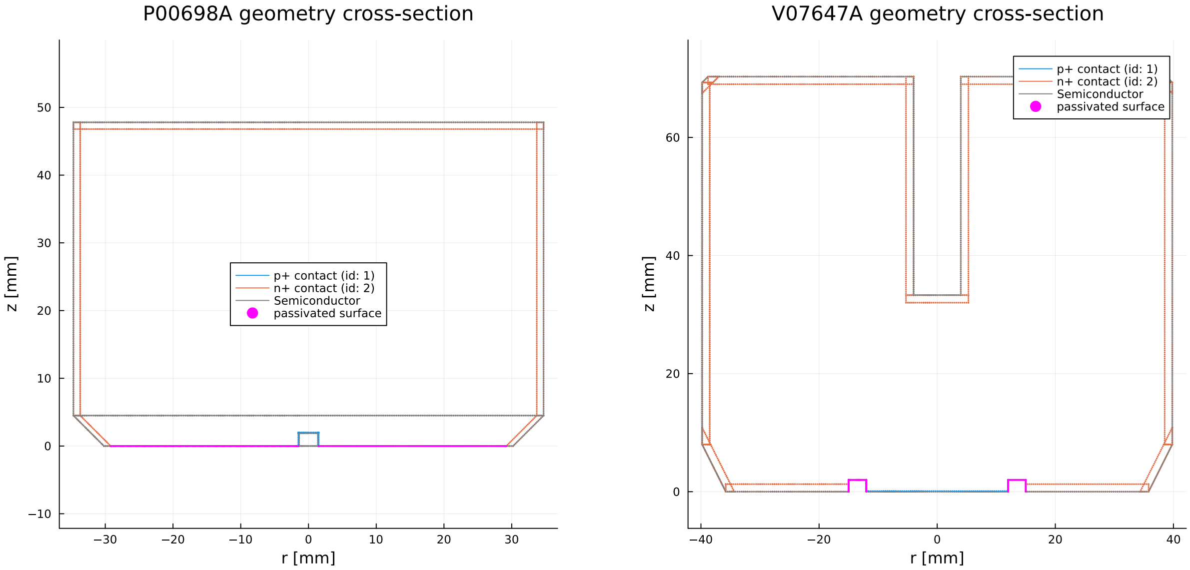

Figure 2.5: Cross-section of the geometry of PPC (left) and ICPC (right) detectors. The n+ contact is shown in orange with a thickness of ∼1 mm. The p+ contact is shown in blue at the bottom, with a thickness of ∼ 0.1 mm for PPCs and < 0.1 mm for ICPCs. PPC detectors have a small point-like p+ contact, which is seperated by a large passivated surface (magenta) from the n+ contact. ICPC detectors have a larger p+ contact with a smaller passivated surface along the circular ditch.

2.2.3 Crystal structure of germanium

Germanium crystals have a face-centered diamond-cubic lattice. Its unit cell is depicted in figure 2.6. Each germanium atom forms four covalent bonds in a tetrahedral arrangement with its nearest neighbours. This lattice gives rise to well-defined crystallographic directions, commonly denoted by the families ⟨100⟩, ⟨110⟩, and ⟨111⟩. They are commonly used to describe both crystal growth and charge transport properties.

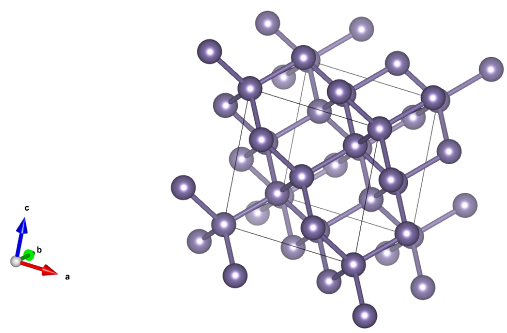

Figure 2.6: Unit cell of a germanium-crystal. Figure created with the software VESTA [31].

The crystal symmetry also influences the motion of charge carriers in germanium. Since the electronic band structure is direction-dependent, the mobility of electrons and holes, and consequently their motion, is anisotropic.

This anisotropy is relevant for HPGe detectors. In an isotropic semiconductor, one would expect the drift velocity to be parallel to the electric field and proportional to it through a scalar mobility. In germanium, however, the mobility is effectively direction dependent: the drift velocity depends not only on the magnitude of the electric field, but also on its orientation with respect to the crystal axes. Therefore, charge carriers generally do not drift exactly along electric-field lines. Instead, both the longitudinal and transverse components of the drift velocity depend on the local field direction in the crystal frame.

2.2.4 Signal formation

When radiation deposits energy in an HPGe detector, electrons of the semiconductor are moved from the valence band to the conduction band, leaving a vacancy in the valence band, called hole; thus creating an electron-hole pair. The hole behaves like a positively charged particle.

The band gap of germanium is comparatively small and temperature dependent. For the fundamental indirect band gap, a commonly used parametrisation is [32, 33]:

$$E_g(T) = 0.742 - \frac{4.8 \times 10^{-4} T^2}{T + 235}\,\mathrm{eV},$$

with T in kelvin. This gives $E_g \approx 0.73\,\mathrm{eV}$ at liquid-argon temperatures, for example $E_g(80\,\mathrm{K}) \approx 0.732\,\mathrm{eV}$. Nevertheless, the mean energy required to create one electron-hole pair in germanium is much larger, about $2.95\,\mathrm{eV}$. The reason is that only a fraction of the deposited energy is used to promote electrons across the band gap; a significant part is transferred to the lattice through phonon excitation [34].

The number of electron-hole pairs created by a single energy deposition is proportional to the amount of deposited energy. Since the detector is fully depleted the electric field inside the detector causes the created charge carriers to drift towards the contacts. If the detector is operated under reverse bias, the electrons move to the n+ contact and the holes move to the grounded p+ contact, where the signal is read out. The electric field determines for the most part the trajectory of the charge clouds, while thermal diffusion and self-repulsion add minor contributions. Self-repulsion is the effect of mutual Coulomb forces acting between charge carriers within the same charge cloud, leading to expansion.

The motion of charge carriers inside the detector induces charge on the electrodes. The charge on an electrode can be related to the electric flux through a closed surface surrounding the electrode using Gauss's law [35]:

$$Q = \varepsilon \oint_{S_k} \boldsymbol{E} \cdot \mathrm{d}\boldsymbol{S} \tag{2.2.1}$$

where S_k denotes a closed surface surrounding electrode k. A more convenient way to describe signal formation is the Shockley-Ramo theorem. For an electron-hole pair, the induced charge and current at electrode k can be expressed in terms of the weighting potential $W_k(\boldsymbol{x})$ and weighting field $\boldsymbol{E}_{W,k}(\boldsymbol{x}) = -\nabla W_k(\boldsymbol{x})$.

$$\begin{aligned} Q(t) &= q\left[W_k(\boldsymbol{x}_h(t)) - W_k(\boldsymbol{x}_e(t))\right] \\ I(t) &= -q\left[\boldsymbol{v}_h \cdot \boldsymbol{E}_{W,k}(\boldsymbol{x}_{\boldsymbol{h}}(t)) - \boldsymbol{v}_e \cdot \boldsymbol{E}_{W,k}(\boldsymbol{x}_e(t))\right] \end{aligned} \tag{2.2.2}$$

where $\boldsymbol{v}_{e/h}$ is the velocity of electrons/holes, q the absolute value of the elementary charge, and $x_{e/h}(t)$ are the electron/hole trajectories. The weighting potential is calculated by solving Laplace's equation with the readout electrode S_k set to one and all other electrodes to zero:

$$\begin{aligned} \Delta W_k(\boldsymbol{x}) &= 0 \\ W_k\big|_{S_k} &= 1 \\ W_k\big|_{S_{j\neq k}} &= 0. \end{aligned}$$

The charge Q is continuously induced while the electrons and holes are moving in the detector, until they are collected at the contacts. This results in a time dependent current pulse that is read out, whose integral is proportional to the deposited energy. Every waveform has a hole component and an electron component with each contributing with opposite sign to the signal.

The weighting potential determines the relative contribution of a charge carrier to the signal. Regions where the weighting potential has higher values, the signal contribution is stronger. For point-contact detectors, the weighting potential is strongly concentrated around the point-contact.

A signal may be created by two or more spatially seperated and independently moving charge clouds, called multi-site events (MSE), as opposed to single-site events (SSE), which result from single charge clouds. The two event topologies are depicted in Figure 2.7.

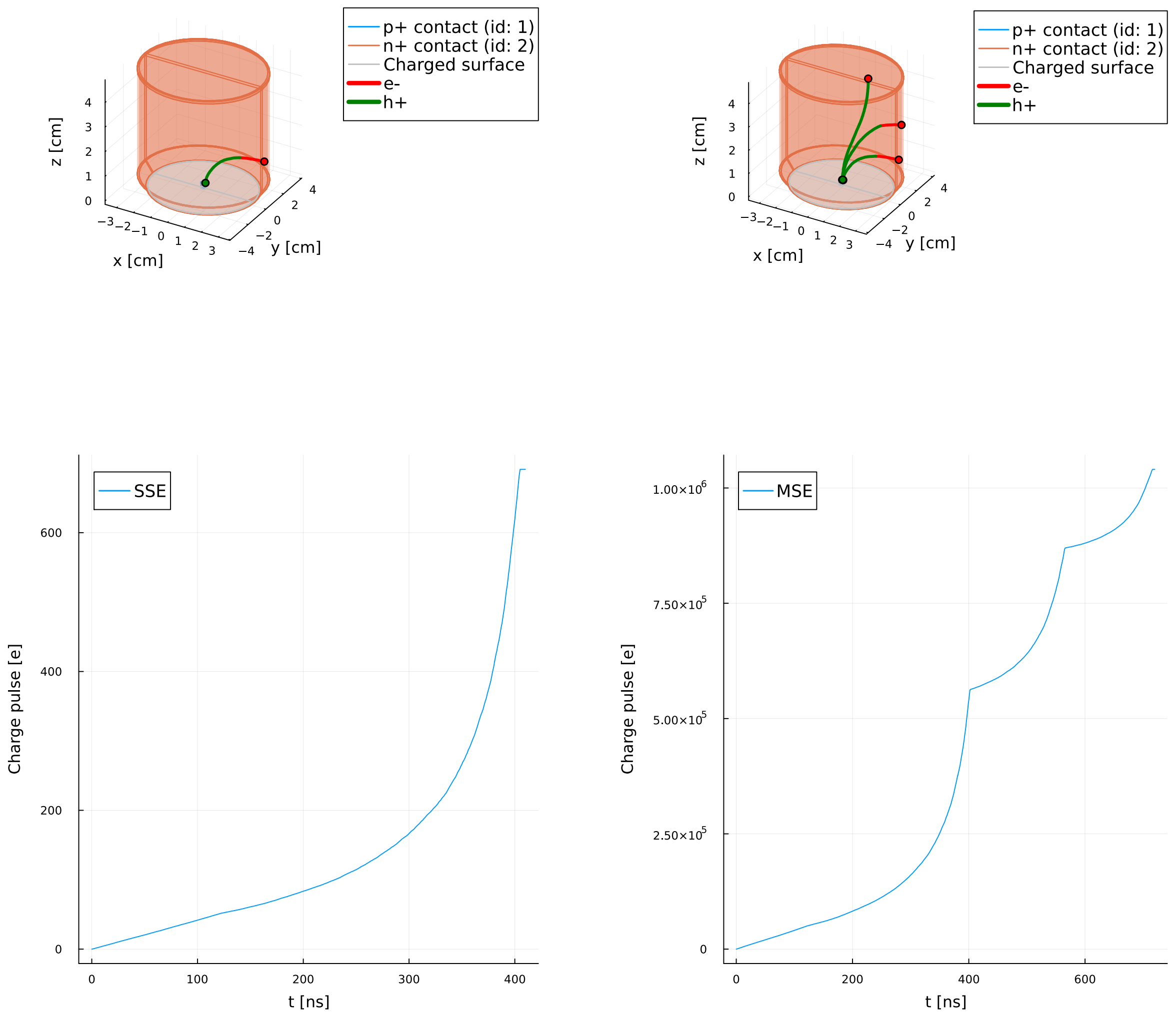

Figure 2.7: Simulated waveforms of a single-site event (left) vs. a multi-site event (right) of point-like energy depositions. The top figures show the drift paths of the electrons and holes, the bottom figures show the charge pulses induced at the p+ contact.

2.2.5 Surface charge effect

During the operation of HPGe detectors, electric charges may accumulate on the passivated surface. Since the passivated region is located between the p+ and n+ contacts, the resulting surface charge modifies the local electric potential and electric field, and consequently the depletion voltage. The sign and magnitude of surface charge during operation is unknown.

The influence of surface charge is particularly important in the vicinity of the passivated surface. Depending on its sign and magnitude, the surface charge can cause the electric field lines either to point away from or towards the passivated surface, thus determining whether more electrons or holes tend to drift into it.

These effects are especially relevant for PPC detectors because they have a large passivated surface close to the readout electrode. Surface charge can therefore alter pulse shapes, charge collection times, and the amount of charge collected from events occurring close to the passivated region.

The behaviour of the electric field for different surface charge values in a PPC detector is shown in figure 2.8.

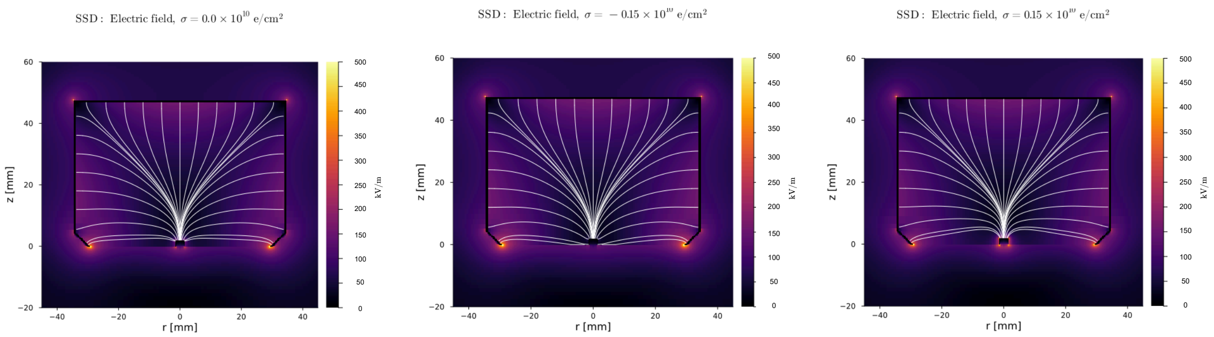

Figure 2.8: Electric field in a PPC detector (P00698A) with zero (left), negative (middle), and positive (right) surface charge σ in the passivated surface. Negative surface charge pulls the electric fieldlines towards the passivated region, while positive surface charge repells them. The electric field was calculated with the software `SolidStateDetectors.jl`.

2.3 Charge transport in HPGe detectors

The trajectories of charge clouds for the most part determine the shape of the induced signals. Thus, it is important to understand charge transport in HPGe detectors and be able to model it properly. Charge transport can be modelled with the continuity equation, which describes the time evolution of the number densities $n_{e/h}(\boldsymbol{x}, t)$ of electrons and holes [36]:

$$\frac{\partial n_{e/h}(\boldsymbol{x}, t)}{\partial t} = \boldsymbol{\nabla} \cdot \left(\underbrace{D_{e/h}(\boldsymbol{x}) \boldsymbol{\nabla} n_{e/h}(\boldsymbol{x}, t)}_{\text{diffusion}} - \underbrace{\mu_{e/h}(\boldsymbol{x}) n_{e/h}(\boldsymbol{x}, t) \boldsymbol{E}_{\text{tot}}(\boldsymbol{x})}_{\text{drift+self-repulsion}} \right) \tag{2.3.1}$$

In this equation $D_{e/h}(\boldsymbol{x})$ is the diffusion coefficient and $\mu_{e/h}(\boldsymbol{x})$ the mobility. The diffusion term describes the random macroscopic behaviour of charges due to of the charge carriers due to collisions and thermal effects. The drift + self-repulsion term dominates the equation and describes the movement of charge carriers due to an electric field $\boldsymbol{E}_{\text{tot}} = \boldsymbol{E}_{\text{det}} + \boldsymbol{E}_{\text{cloud}}$. The main contribution comes from the electric field $\boldsymbol{E}_{\text{det}}$ that is present in the detector. It depends on the bias voltage, impurity profile, and boundary conditions between detector surface and surroundings. The second order contribution $\boldsymbol{E}_{\text{cloud}}$ comes from the mutual Coulomb self-repulsion of equally charged carriers within a cloud. It depends on the charge cloud size and number of carriers within the cloud.

2.3.1 Charge drift in HPGe detectors

The most important contribution to the trajectory of the electrons and holes is the drift, which is driven by the electric field due to the applied bias voltage. In this section the contributions of diffusion and self-repulsion are neglected, which reduces Equation 2.3.1 to the following:

$$\frac{\partial n_{e/h}(\boldsymbol{x},t)}{\partial t} = -\nabla \cdot \underbrace{\left(\mu_{e/h}(\boldsymbol{x}) n_{e/h}(\boldsymbol{x},t) \boldsymbol{E}_{\text{det}}(\boldsymbol{x})\right)}_{\boldsymbol{j}_{\text{drift}}} \tag{2.3.2}$$

In equation 2.3.2 $\boldsymbol{j}_{\text{drift}} = q \cdot n_{e/h} \cdot \boldsymbol{v}_{e/h}$ is the current density, and the drift velocity can be identified to be:

$$\boldsymbol{v}_{e/h} = \mu_{e/h} \boldsymbol{E}_{\text{det}} \tag{2.3.3}$$

where $\mu_{e/h}$ is the mobility of electrons (negative sign) and holes (positive sign). Equation 2.3.3 is called *Ohmic behaviour* and its validity in germanium crystals depends on the crystal temperature and electric field strength. In particular, for the operating temperature in LEGEND-200 (78 K), equation 2.3.3 is valid for $E \leq 100$ V/cm.
However, if the temperature of electrons rises above the lattice temperature, as is the case in LEGEND, the drift velocity depends on the orientation of the crystal and is not parallel to the electric field anymore. This can be modelled with an anisotropic mobility for both electrons and holes.
Both the longitudinal (the component parallel to the electric field) as well as the transversal component (the component perpendicular to the electric field) depend on the orientation of the crystal with respect to the electric field. Along the principal axes of germanium, $\langle 100 \rangle$, $\langle 110 \rangle$, and $\langle 111 \rangle$, the drift velocity must be parallel to the electric field because the physics does not change when the crystal is rotated around any of the symmetry axes. This can only be the case if the transverse component of the drift velocity is zero. For each crystallographic direction l, the drift velocity can be computed with the empirical parametrization proposed by [37, 38]:

$$v_l = \frac{\mu_0 E}{(1 + (E/E_0)^\beta)^{1/\beta}} - \mu_n E \tag{2.3.4}$$

The temperature dependent parameters E_0 and β can be fitted to experimental data for all of the crystallographic directions. For low electric field strengths ($E \leq 100$ V/cm) the drift velocity v_l becomes independent of the symmetry axes and one recovers Equation 2.3.3.
The negative term $\mu_n E$ only holds for electrons and accounts for the Gunn-effect. The Gunn-effect is the decrease of the electron mobility at high electric field strengths. It is caused by electrons moving from the global minimum in the conduction band to a local minimum with smaller curvature. Since the effective mass is inversely proportional to the curvature of the conduction band this results in a higher effective mass and consequently decreases the mobility.

At electric field-strengths of ~ 1000 V/cm the drift velocities for both electrons and holes are of the order of 10^7 cm/s in Ge at 78 K [39] .

2.3.2 Charge cloud effects

In the rest-frame of the charge cloud itself, $\boldsymbol{E}_{\text{det}} = 0$ and Equation 2.3.1 only describes diffusion and self-repulsion. The diffusion coefficient $D = \mu \frac{k_B T}{q}$ follows from the Einstein-Smoluchowski

relation [40], with k_B being the Boltzmann-constant.
Note that the charge clouds are modelled as spherical charge distributions, and therefore inside the charge clouds there is an electric field according to Gauss' Law. When integrating over the charge cloud with radius R, this results in the following equation [36]:

$$q \int_\Omega \partial_t n(r,t) \mathrm{d}V = q \int_\Omega \left(\frac{D}{r^2} \partial_r (r^2 \partial_r n(r,t) - \mu \nabla \cdot (n(r,t)\boldsymbol{E}(r)) \right) \tag{2.3.5}$$

The first term on the right hand side in Equation 2.3.5 evaluates to the following:

$$q \int_\Omega \frac{D}{r^2} \partial_r \left(r^2 \partial_r n(r,t) \right) \mathrm{d}V = D \left(\partial_{RR} Q(R,t) - 2 \frac{\partial_R Q(R,t)}{R} \right) \tag{2.3.6}$$

where ∂_{RR} denotes the second partial derivative with respect to the charge cloud radius R. The second term can be calculated using Gauss's Law for the electric field, and the divergence theorem for the integral:

$$\int_\Omega \mu \boldsymbol{\nabla} \cdot (n(r,t)\boldsymbol{E}(r,t)) \, \mathrm{d}V = \frac{\mu}{4\pi R^2} \frac{\partial_R Q(R,t)}{Q(R,t)} \tag{2.3.7}$$

Finally, Equation 2.3.1 can be simplified to the following differential equation, that ignores drift and only describes diffusion and self-repulsion:

$$\partial_t Q(R,t) = \underbrace{D \left(\partial_{RR} Q(R,t) - 2 \frac{\partial_R Q(R,t)}{R} \right)}_{\text{diffusion}} - \underbrace{\frac{\mu}{4\pi R^2 Q(R,t)} \partial_R Q(R,t)}_{\text{self-repulsion}} \tag{2.3.8}$$

This equation does not have an analytic solution and [41] propose to analyze diffusion and self-repulsion independently.

Diffusion

The diffusion term in Equation 2.3.8 is simply the Laplace operator in spherical cooridinates without angular dependencies. Its solution depends on the initial conditions. Assuming a Gaussian distribution at $t = 0$ with $n(r, 0) \sim \mathcal{N}(0, \sigma_0)$, the charge concentration propagates as follows, with N being the total number of charges per cluster:

$$n^{\text{diff}}(r,t) = \frac{N}{[2\pi(\sigma_0 + 2Dt)]^{3/2}} \exp\left(-\frac{r^2}{2(\sigma_0^2 + 2Dt)} \right) \tag{2.3.9}$$

Equation 2.3.9 describes the radial propagation of a charge cluster, only subject to diffusion. It assumes a spherical cloud, with the density following a Gaussian distribution with variance $\sigma^2(t) = \sigma_0^2 + 2Dt$.

Self-repulsion

To describe self-repulsion, spherical charge clusters are assumed while neglecting diffusion and drift due to the external electric field. Equation 2.3.8 then reduces to:

$$\partial_t Q(r,t) = -\frac{\mu}{4\pi\varepsilon} \frac{Q(r,t)}{r^2} \partial_r Q(r,t) \tag{2.3.10}$$

This nonlinear first-order partial differential equation is homogeneous in both Q and r, and can be solved using a self-similar ansatz, which leads to the closed-form solution

$$Q(r,t) = \frac{4\pi\varepsilon}{3\mu} \frac{r^3}{t} \tag{2.3.11}$$

where $\varepsilon = \varepsilon_r \varepsilon_0$ is the absolute permittivity of germanium, with ε_r the relative dielectric constant and ε_0 the vacuum permittivity.

Equation 2.3.11 describes the spatial and temporal evolution of a spherical charge cloud, whose total charge remains constant. It allows to see how the radius of the charge cloud evolves as a function of time:

$$r(t) = \sqrt[3]{\frac{3\mu Q}{4\pi\varepsilon} t} \tag{2.3.12}$$

In figure 2.9 the evolution of the charge-cloud radius, as described by equation 2.3.12, are plotted for electron and hole clouds, assuming a deposited energy of $E = 2039\,\mathrm{keV}$. For the electron mobility $\mu_e = 3.6 \times 10^4\,\mathrm{cm}^2/(\mathrm{V\,s})$ and for holes $\mu_h = 4.2 \times 10^4\,\mathrm{cm}^2/(\mathrm{V\,s})$ was used [42].

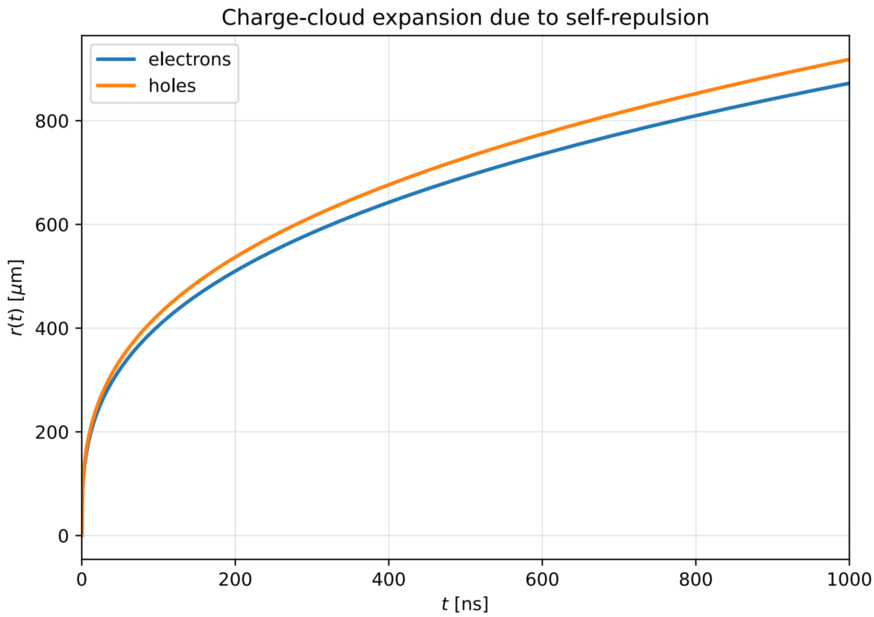

Figure 2.9: Illustration of how the radius of a charge cloud evolves over a time of 1000 ns, for electrons and holes, if drift and diffusion are neglected, based on equation 2.3.12. An initially deposited energy of $E = 2039\,\mathrm{keV}$ is assumed.

2.3.3 Charge trapping

The discussion in this section follows the treatment of charge trapping in germanium detectors presented in [43]. Charge trapping in germanium arises when drifting electrons or holes are captured by localized defect or impurity states in the crystal, including disordered regions produced during crystal growth, detector processing, or radiation damage. When this happens, the amount of free charge available to induce signal on the electrodes decreases while drifting, so the measured pulse height is reduced and the deposited energy is underestimated. In a simple picture, the surviving free charge decreases approximately exponentially with the total path traveled through the crystal, which is set by the density of trapping centers n and their capture cross section σ. For germanium, the relevant path length is not determined by drift motion alone: because the carrier thermal velocities ($1.7 \times 10^7\,\mathrm{cm/s}$ for electrons and $1.3 \times 10^7\,\mathrm{cm/s}$ for holes) at operating temperature are comparable to their drift velocities, thermal motion also contributes to the distance a carrier travels before collection. This is why charge trapping in Ge is more fundamentally described by the trapping product $(n\sigma)^{-1}$ rather than by a pure trapping time or a pure mean free drift length.

Electrons and holes are not trapped equally. In undamaged HPGe detectors, electron trapping is often stronger than hole trapping, whereas radiation-induced damage tends to enhance hole trapping more strongly and can eventually make it dominant. Since the probability of trapping increases with carrier path length, interactions occurring further from a collecting electrode generally suffer more incomplete charge collection, producing a depth-dependent bias in the measured signal. Event-to-event variations in the amount of trapping broaden monoenergetic peaks and therefore degrade the energy resolution, even when the average charge loss is small. For a detector with characteristic drift dimension d and mean free trapping length λ, the fractional charge loss varies approximately as d/λ in the weak-trapping limit. Therefore, trapping becomes relevant for the spectral resolution once

$$\frac{d}{\lambda} \sim \frac{\Delta E}{E}. \tag{2.3.13}$$

For HPGe detectors with energy resolutions of order a few keV at MeV energies, this corresponds to relative effects of order 10^{-3}. Thus, in high-quality undamaged detectors, charge trapping typically contributes at the sub-keV to few-keV level, while stronger trapping, for example due to radiation damage, can lead to a significantly larger degradation.

2.4 Electronics

In this section, the electronics chain of LEGEND-200 is described according to [44]. The electronics chain of LEGEND-200 processes and stores the signals induced by moving charge in HPGe detectors for later analysis, and is subject to several constraints: the detector environment must be radiopure and operated at cryogenic temperatures, which limits the amount of active electronics that can be placed in close proximity to the detectors. At the same time, the signal cables should be kept as short as possible to preserve signal integrity and timing performance, since the rise time of the waveforms is of the order of 50 ns. A schematic of the electronics chain is shown in Figure 2.10.

The charge-sensitive amplifier (CSA) integrates the current pulse induced in the detector and produces an analog voltage signal proportional to the collected charge. This signal is then digitized by an analog-to-digital converter and stored by the data acquisition (DAQ) system.

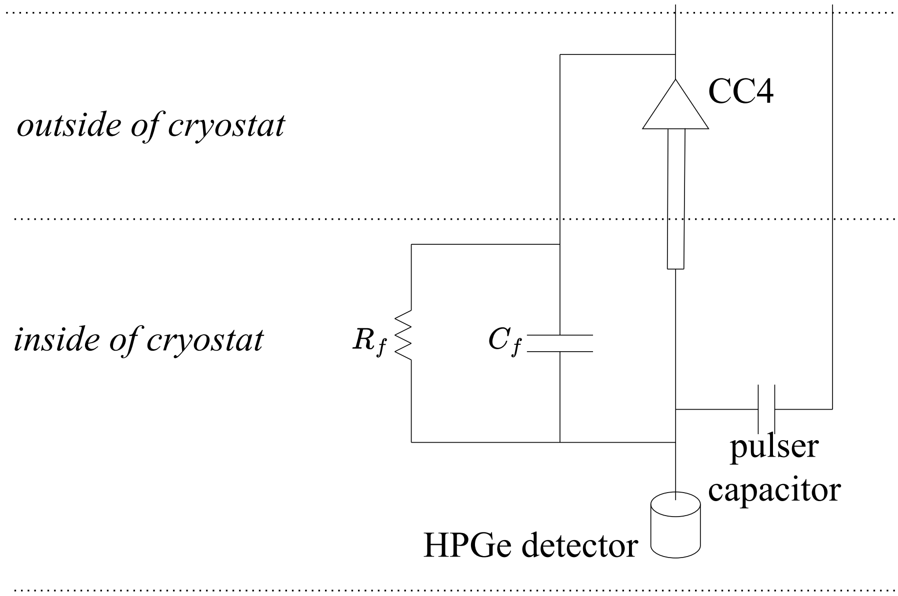

Figure 2.10: Schematic of the electronics chain in LEGEND-200. The low-mass front-end (LMFE) implements a charge-sensitive amplifier that integrates the induced current pulse. The signal is transmitted via low-mass coaxial cables to the CC4 preamplifier, which provides further amplification and drives the signal to the readout electronics. The pulser capacitor is used to inject test pulses with known amplitude and frequency.

2.4.1 Charge-sensitive amplifier

The charge-sensitive amplifier (CSA) used in LEGEND-200 is split into two stages: a radiopure Low-Mass Front-End (LMFE), located close to the HPGe detector, and a second-stage CC4 preamplifier board based on the GERDA readout electronics. It contains a feedback capacitor C_f and a feedback resistor R_f. The CSA integrates the input current, resulting in a voltage signal

$$V = \frac{Q}{C_f} \tag{2.4.1}$$

where Q is the collected charge. The feedback resistor provides a continuous discharge path for the capacitor, preventing saturation and producing an exponentially decaying tail of the pulse,

$$V(t) \propto e^{-t/\tau}, \qquad \tau = R_f \cdot C_f \tag{2.4.2}$$

A summary of example values of these parameters are listed in table 2.1

parameter	example value
Q [pC]	0.1 pC
R_f [GΩ]	1 GΩ at 87 K [45]
C_f [pF]	0.1 [46]
$\tau = R_f \cdot C_f$ [ns]	100

Table 2.1: Example values for the electronics parameters in the CSA. The value for Q is calculated for an energy deposition of 2039 keV, assuming 1 electron-hole pair is created per 2.95 eV.

The CC4 is located approximately 30 cm above the detector array and is connected to the LMFE by low-mass Axon pico-coaxial cables. These are miniature shielded coaxial cables used for the short, noise-sensitive connection between the LMFE and the second amplification stage. The CC4 then provides a differential output to drive the signal over an approximately 10 m long Kapton flat cable to the cryostat flange [45].

The CSA must have a high input impedance to ensure that the induced current is efficiently integrated, so that the pulse amplitude is proportional to the energy deposited by the detector.

2.4.2 Digitization and data acquisition (DAQ)

After amplification by the CSA, the signal is transmitted as an analog voltage signal to the FlashCam system, which performs the digitization and serves as the interface between the front-end electronics and the DAQ.

The analog signal is continuously sampled with a period of 16 ns (corresponding to a sampling frequency of 62.5 MHz). Each readout channel is digitized using multiple interleaved analog-to-digital converters (ADCs), whose outputs are combined to form a single waveform.

The digitized signal is then processed digitally. The raw CSA output contains a slowly decaying exponential tail caused by the finite feedback time constant of the preamplifier. In the digital signal-processing chain, a pole-zero correction is applied to compensate this decay before energy filtering, resulting in an approximately step-like charge waveform. The pole-zero correction is illustrated in figure 2.11

To monitor the stability of the detector and electronics response, test pulses corresponding to an energy of approximately 1 MeV are injected into the front-end electronics of each germanium detector every 20 s, corresponding to a repetition rate of 0.05 Hz.

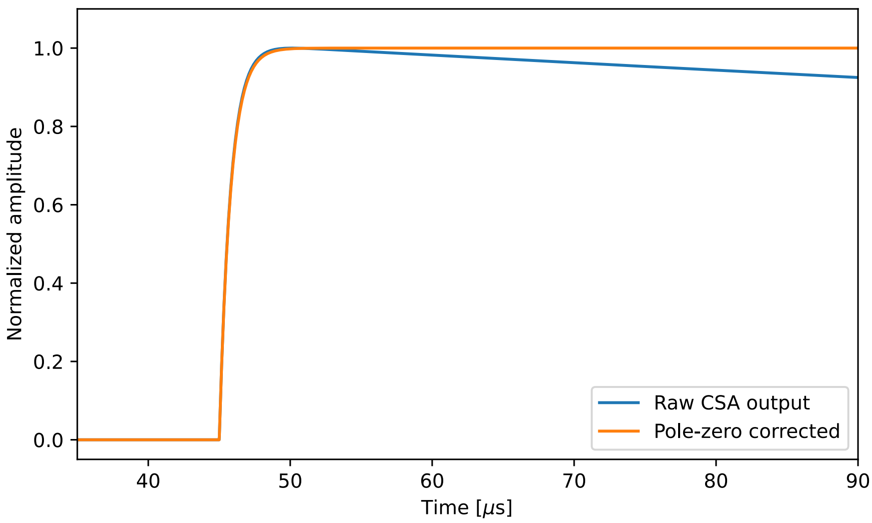

Figure 2.11: Illustration of pole-zero correction applied to a waveform with exponentially decaying tail from the CSA, resulting in a step-like waveform.

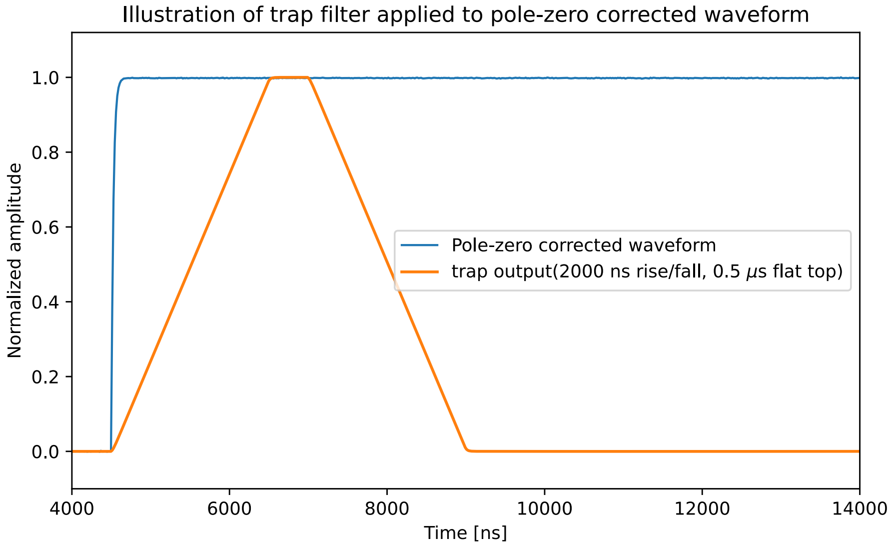

Figure 2.12: Illustration of a trapezoidal filter applied to a pole-zero corrected waveform.

2.5 Energy calibration in LEGEND-200

The energy deposited in an HPGe detector is reconstructed from the digitized charge waveform by applying digital shaping filters. For illustration, a simplified trapezoidal filter with rise and fall times of (2000 ns) and a flat-top duration of (500 ns) is shown in Figure 2.12. The amplitude of the shaped waveform, evaluated on the flat top, is proportional to the deposited energy. In the full LEGEND-200 reconstruction, the filtering procedure is more involved and includes several filters used for energy estimation, timing, and charge-trapping corrections. Since the DAQ records waveforms in arbitrary units, given by ADC counts, the detector response has to be calibrated using radiation sources with well-known gamma-ray energies. This calibration determines the relation between the measured pulse amplitude in ADC counts and the corresponding deposited energy [46, 47].
In weekly calibration runs ^{228}Th is used for the calibration of the energy scale for HPGe detectors, the monitoring of the gain stability and energy resolution, and for the tuning of the event selection criteria.

^{228}Th is suitable for calibration for several reasons:

- The energy spectrum of the decay-chain ranges from 0.0 - 2.6 MeV, which includes the $Q_{\beta\beta}$ value
- The energy spectrum contains multiple high-intensity γ lines that can be used to tune event-selection criteria
- The 2614 keV line from the decay of ^{208}Tl has a double escape peak (DEP) at 1592 keV, which can be used to tune event-selection criteria

It is important not to place the calibration source too close to the detector (to avoid pile-up) and not too far away (to get enough statistics in a reasonable time). During calibration runs one aims to uniformly expose the detector array to the calibration source such that enough statistics is achieved in all detectors.

The decay chain of ^{228}Th consists of 6 alpha and 4 beta decays, during which γ radiation is emitted. The charged α and β particles produced in the decay chain are strongly attenuated by the steel encapsulation. Consequently, the calibration spectrum measured by the HPGe detectors is dominated by γ radiation, which is much more penetrating and provides well-defined monoenergetic calibration lines.
One important high-intensity line in the spectrum is the $E_\gamma = 2614.5$ keV line from the beta decay of ^{208}Tl. The photon undergoes pair production inside the detector, creating an electron-positron pair. The electron deposits its energy resulting in a signal while the positron annihilates with an electron from the detector material producing two photons, each with an energy of 511 keV. This results in three prominent peaks in the energy spectrum:

- If both photons escape from the detector only the remaining energy is deposited in the detector, resulting in a **double-escape peak** at $E_\gamma - 2m_0c^2 = 1592.5$ keV, where $m_0c^2 = 511$ keV is the energy corresponding to the rest-mass of the electron and positron.
- If only one photon escapes the total deposited energy is that of the other photon and the the electron. This creates a **single escape peak** at $E_\gamma - m_0c^2 = 2103.5$ keV.
- If no photon escapes the full energy is deposited in the detector, visible in the **full energy peak** at $E_\gamma = 2614.5$ keV

Chapter 3

Background in LEGEND-200 and Pulse Shape Discrimination

3.1 Motivation

In LEGEND-200, the search for $0\nu\beta\beta$ decay relies on a combination of signal-identification and background-suppression techniques [27]. These include anti-coincidence cuts between different germanium detectors, the liquid-argon and muon veto, and pulse shape discrimination (PSD).

Signal events from $0\nu\beta\beta$ decay are expected to deposit their energy within a small volume of $1\,\mathrm{mm}^3$ inside a single detector and therefore typically appear as single-site events [48]. Many relevant background processes, in contrast, produce multi-site energy depositions or involve energy released outside the detector crystal. PSD exploits the fact that the topology of the energy deposition inside the detector is reflected in the shape of the measured waveform. By analysing the pulse shape, signal-like and background-like events can therefore be distinguished even when they have similar deposited energies. In this way, PSD provides one of the central analysis tools for background rejection in LEGEND-200. Its performance depends on a detailed understanding of how charge creation and transport inside the detector determine the observed signal.

This chapter introduces pulse shape discrimination as a central analysis tool in LEGEND-200 and discusses how different background classes affect pulse-shape observables, with particular emphasis on α-induced surface events.

3.2 Principles of Pulse Shape Discrimination

Pulse shape discrimination uses observables derived from the digitized detector waveforms to distinguish different event topologies. The relevant distinction for $0\nu\beta\beta$ searches is between single-site events (SSEs), which are signal-like, and background-like events such as multi-site events (MSE) or surface events. In LEGEND-200, PSD is only applied to detectors and data periods for which the PSD performance has been validated [49].

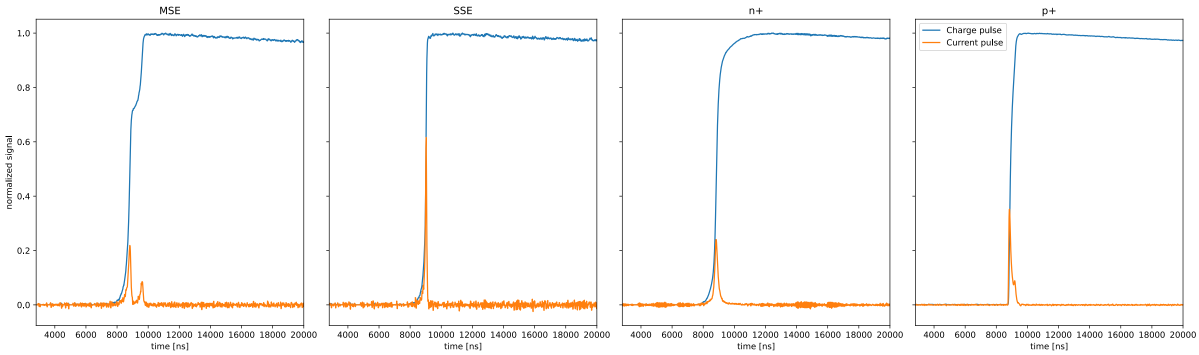

Figure 3.1: Example charge pulses (blue) together with the current pulses (orange), resulting from different event-toplogies. From left to right: single-site (SSE), multi-site (MSE), n+ events, and p+ events. Classification labels for the waveforms were created by Yuri van der Burg.

3.2.1 A/E parameter

The A/E parameter is defined as the ratio of the maximum current amplitude A to the reconstructed energy E. The current signal is obtained from the time derivative of the charge waveform. For a localized single-site energy deposition, the charge carriers are created in a small volume and their drift produces a relatively compact current pulse with a large maximum amplitude. For a multi-site event, the same total energy is distributed over several spatially separated interactions. The charge carriers then arrive over a broader time interval, which lowers the maximum current amplitude relative to the total collected charge. As a result, single-site events tend to have larger, narrowly distributed A/E values, while multi-site gamma events tend to populate lower A/E values.

3.2.2 Late charge (LQ) parameter

The late-charge parameter (LQ) is designed to identify events with delayed charge collection. Such delayed components are typical for surface events, especially alpha events on or near the p+ contact. In these regions, the electric field and charge-collection conditions differ from those in the detector bulk, so part of the charge can be collected later than in ordinary bulk events.

The LQ parameter quantifies the amount of charge collected in a late part of the waveform. It is defined as the integral of uncollected charge after the waveform has reached 80% of its maximum (referred to as `tp80`) [20]. Bulk single-site events usually have fast and complete charge collection and therefore small late-charge values. Surface alpha events can show an enhanced late component and are rejected by an LQ cut. In the LEGEND-200 alpha analysis, p+ surface alpha events are expected to have unusual pulse shapes and to be efficiently removed by PSD cuts [49]. Figure 3.2 illustrates how the LQ-parameter is calculated.

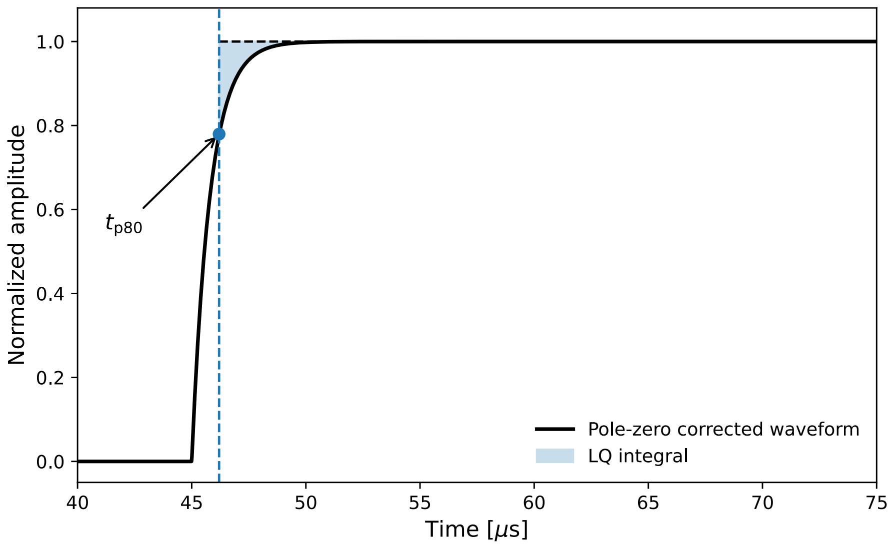

Figure 3.2: Schematic illustrating how the LQ-parameter is calculated.

3.3 Backgrounds and their pulse shape signatures

A low background index (BI) is essential for the sensitivity of LEGEND-200. The BI is usually expressed as the number of background events per unit energy, and exposure, and therefore quantifies the expected background rate in the region of interest around $Q_{\beta\beta}$.

The different background components in LEGEND-200 can be classified not only by their physical origin but also by their characteristic pulse-shape signatures. This connection is central for PSD, as it determines which observables are effective for suppressing a given background class.

The background model of LEGEND-200 contains several classes of sources. These include radioactive contaminants in or close to the HPGe detector array, radioactive impurities in the liquid argon, external gamma radiation from the cryostat and surrounding materials, cosmogenic and muon-induced contributions, and activity in other detector-support and instrumentation components [49]. In the data analysis, events are suppressed by a sequence of cuts, including data-quality cuts, multiplicity cuts, the muon veto, the liquid-argon veto, and PSD cuts.

3.3.1 Gamma background

Gamma radiation originates primarily from radioactive contaminants in materials surrounding the detector array, including isotopes from the ^{238}U and ^{232}Th decay chains, as well as ^{40}K and cosmogenic isotopes such as ^{60}Co. Gamma rays interact in germanium via photoelectric absorption, Compton scattering, or pair production.

A key feature of gamma-induced background is that it often leads to multi-site energy depositions. For example, a gamma ray may undergo multiple Compton scatterings before being fully absorbed, resulting in spatially separated interaction points within a single detector or across multiple detectors.

These multi-site events produce charge carriers that arrive at the electrodes over an extended time interval. Consequently, the induced current signal is broadened, and the maximum current amplitude is reduced compared to a localized single-site event with the same total deposited energy. This results in systematically lower A/E values for gamma-induced events, making the A/E parameter an effective discriminator.

Additional suppression is achieved through detector anti-coincidence cuts, which reject events depositing energy in multiple detectors, and through the liquid-argon veto, which tags events accompanied by energy deposition in the surrounding LAr [49].

3.3.2 Beta background

Beta background in LEGEND-200 is dominated by decays of ^{42}K, which is produced by the decay of ^{42}Ar in the liquid argon. Since ^{42}K ions are positively charged, they can drift in electric fields and accumulate on detector surfaces.

The resulting beta decays can occur either directly at the detector surface or in its immediate vicinity. Depending on the exact interaction location, these events can exhibit different pulse-shape characteristics. Energy depositions in the detector bulk tend to resemble single-site events and can therefore be difficult to distinguish from signal using A/E alone. In contrast, events occurring very close to the detector surface may experience modified charge-collection conditions, leading to distortions in the waveform.

In addition, the liquid-argon veto is highly effective for this background, because MeV-scale beta particles have ranges of order mm to cm in LAr. For example, a 1 MeV electron has a range of about 4 mm in LAr (from the NIST ESTAR database for electrons in argon [**NIST_ESTAR**]). Therefore, beta decays occurring in the LAr close to the detector can deposit part of their energy in the argon, producing scintillation light that can be tagged by the LAr veto.[49].

3.3.3 Muon and cosmogenic background

Prompt muon-induced events, i.e. energy depositions occurring in temporal coincidence with a muon or its immediate secondary shower particles, are suppressed by the water-Cherenkov muon veto. In addition, cosmic-muon-induced neutrons can activate the germanium detectors underground, most importantly through the production of ^{77}Ge and ^{77m}Ge by neutron capture on ^{76}Ge. These isotopes beta-decay with $Q_\beta \simeq 2.7$ MeV and can therefore contribute in the region around $Q_{\beta\beta}$. However, simulations for GERDA show that this delayed muon-induced component can be reduced by active background rejection and delayed coincidence cuts to a level well below the LEGEND-200 background goal. Longer-lived cosmogenic isotopes produced before underground storage, such as ^{60}Co, are expected to be small because the detectors are stored underground as in GERDA; residual contributions are included in the background model when relevant [49, 50].

3.3.4 Alpha background

Interaction of α particles in germanium

The rate of α-induced background events can vary significantly depending on detector type, detector location within the cryostat, and operating conditions. Alpha particles originate from radioactive contaminants on detector surfaces and nearby materials.
One possible source is ^{210}Pb which decays to ^{210}Po via two consecutive β^- decays, which eventually decays into ^{206}Pb under the emission of an alpha particle with an energy of 5.41 MeV [51].

When massive particles penetrate germanium they eventually get attenuated as they lose energy while traversing matter. For charged particles, the mean energy loss E per unit distance

x travelled, also called stopping power, can be roughly estimated with the Bethe-Bloc formula [52]:

$$-\frac{\mathrm{d}E}{\mathrm{d}x} = \frac{4\pi q^2 e^2}{m_0 c^2 \beta^2} NZ \left[\ln\left(\frac{2m_0 c^2 \beta^2}{I(1-\beta^2)} \right) - \beta^2 \right] \tag{3.3.1}$$

In this expression:

- $Z = 32$ and $N = 44$ are the atomic number and number density of the absorbing material (in our case ^{76}Ge).
- m_0 and e are the rest-mass and charge of the electron.
- I represents the average excitation and ionization potential of the absorber. For ^{76}Ge $I = 350\,\mathrm{eV}$ [53].
- $\beta = v/c$ is the velocity in units of the speed of light c and q the charge of the primary particle. Since an alpha particle consists of two neutrons and two protons, $q = 2e$

To calculate the range R an alpha particle with initial energy E_0 can penetrate into germanium, one has to integrate the inverse stopping power $S(E)$ over the range of energy:

$$R(0) = -\int_0^{E_0} \left(\frac{\mathrm{d}E}{\mathrm{d}x} \right)^{-1} \mathrm{d}E = \int_0^{E_0} \frac{\mathrm{d}E}{S(E)} \tag{3.3.2}$$

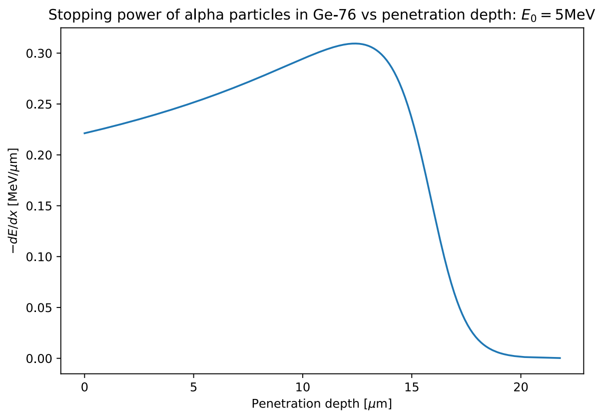

Figure 3.3: Stopping power $-\mathrm{d}E/\mathrm{d}x$ as a function of penetration depth for an alpha particle with initial kinetic energy $E_0 = 5\,\mathrm{MeV}$ in germanium. The particle penetrates approximately $20\,\mu\mathrm{m}$ before coming to rest.

The curve in figure 3.3 was obtained by calculating the stopping power $S(E) = -\mathrm{d}E/\mathrm{d}x$ of alpha particles in germanium from the Bethe–Bloch formula as a function of their kinetic energy. The penetration depth was then determined by numerically integrating the inverse stopping power

$$R(E) = \int_E^{E_0} \frac{\mathrm{d}E'}{S(E')},$$

which gives the depth reached when the alpha energy has decreased from its initial value E_0 to E. In this way, both the stopping power S and the penetration depth R can be expressed as a function of the alpha particles kinetic energy E. The total penetration depth corresponds to the point where the alpha particle has lost its full kinetic energy and comes to rest. For an alpha particle with initial kinetic energy $E_0 = 5$ MeV in germanium this is approximately 20 μm. However, it should be noted that this is just a rough estimation.

The n^+ contact, with a typical thickness of 1–2 mm, effectively absorbs α particles and prevents them from contributing to the detected signal. In contrast, the p+ contact and the passivated surface layer are only a few μm thick, allowing α particles to penetrate into the active volume. As a result, α-induced background events predominantly originate from regions near the p+ contact and the passivated surface.

Pulse-shape signatures of α events

The pulse-shape signature of α events is determined by two main features: the short range of the particle and the location of the energy deposition. Since α particles stop within only a few tens of micrometers in germanium, their energy deposition is highly localized and always occurs close to a detector surface. In this respect, α events are single-site-like in their spatial extent. However, unlike $0\nu\beta\beta$ events, they are not distributed throughout the detector bulk, but are confined to regions where the electric-field and charge-collection conditions can differ strongly from those in the bulk.

In particular, charge clouds originating from α interactions tend to move through the passivated surface. In this region, the effective mobility is reduced resulting in incomplete or delayed charge collection. This produces waveforms with a reduced component and an extended tail. Such delayed charge collection was observed in point-contact HPGe detectors in the Majorana Demonstrator and motivated the use of delayed-charge-recovery observables for rejecting passivated-surface α events [54]. In LEGEND-200, the related late-charge parameter LQ is used to identify events with charge collection at late times [27, 49].

Chapter 4

Pulse Shape Simulation

4.1 Motivation

Since PSD is based on the waveform shape, its interpretation requires a detailed understanding of how detector physics affects a measured signal. In HPGe detectors, the pulse shape is determined not only by the deposited energy and the interaction topology, but also by the interaction position and by detector-dependent properties such as geometry, electric field, impurity profile, temperature, and bias voltage. These quantities influence charge-cloud formation, charge drift, diffusion, self-repulsion, and finally signal induction at the electrodes. A pulse shape simulation (PSS) aims to model this full chain and to predict the waveform for a given set of physical and detector parameters. Such a simulation is essential for understanding the origin of signal-shape to discriminate between signal and background.

To model these processes, dedicated software frameworks have been developed that numerically describe the detector geometry and electric field, simulate charge transport, and calculate the induced signal. In the context of LEGEND and this work, the two most relevant frameworks are `SolidStateDetectors.jl` (SSD) [55] and EH-Drift [56]. Both provide tools for pulse shape simulation and form the basis for the studies presented in this chapter. Their main features and implementations are discussed in sections 4.2 and 4.3.

4.2 `SolidStateDetectors.jl`

In the LEGEND collaboration the main tool used for PSS is SSD, a software package written in the programming language julia. It allows to simulate detector geometry, electric potential and field calculation, and charge transport including charge cloud effects. Based on these inputs, the trajectories of charge carriers are calculated, from which the induced signal is derived in the ideal case (i.e. without detector response and noise). Furthermore, it allows to include charge trapping in the simulation. Figure 4.1 depicts the simulation chain in SSD from detector simulation to ideal PSS.

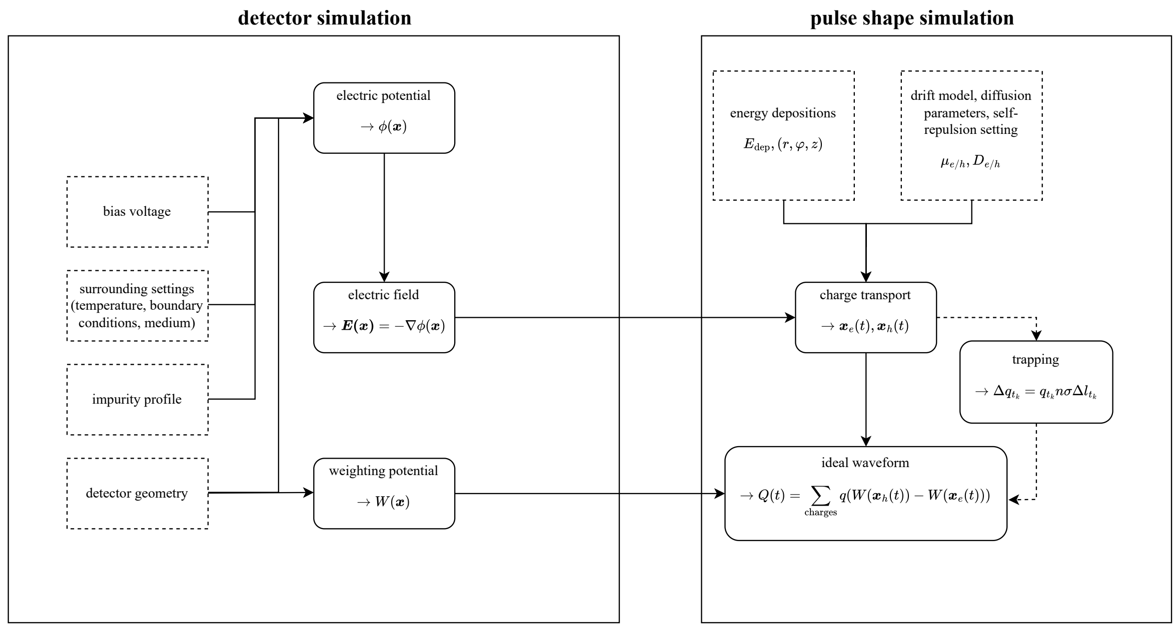

Figure 4.1: Flowchart of the simulation chain in SSD starting from detector simulation to the generation of ideal charge pulses. Dashed boxes denote simulation inputs, while solid rounded boxes represent processing steps performed by the simulation. Figure adapted from [57].

4.2.1 Detector simulation

The detector simulation starts with defining the detector geometry, impurity profile, bias voltage, and crystal temperature, based on which the electrostatic calculations are performed. These parameters are defined in a `yaml` config file.

4.2.2 Detector geometry

SSD uses a constructive solid geometry (CSG) approach to describe various geometries. In this framework, complex detector shapes are built from a set of simple volume primitives, which can then be combined and transformed to obtain the final geometry. Typical primitives include shapes such as boxes, tubes, cones, prisms, ellipsoids, polycones, or toroidal volumes. Each primitive is defined in its own local coordinate system and is initially centered around the origin. More elaborate detector components are then constructed by applying Boolean operations, namely the union, difference, and intersection of two or more primitives. The union operation allows multiple volumes to be merged into a single object, while the intersection keeps only the common overlapping region of the participating shapes. The difference operation is used to subtract one volume from another, which is particularly useful for introducing cavities, grooves, bore holes, or contact structures into an otherwise simple detector body. In this way, the detector bulk, electrodes, dead layers, passivation regions, and other structural parts can all be represented geometrically within the same formalism.

To position these objects correctly, primitives or whole sets of primitives can be translated and rotated. Translations are specified by a Cartesian displacement vector, whereas rotations can be given either by angles about coordinate axes or by a full rotation matrix.

Figure 4.2 schematically illustrates how simple primitives can be combined by Boolean operations to construct more complex detector geometries. As an example, the bulk of a PPC detector can be represented as the union of a cylindrical tube and a conical section. The tube is specified by its radius and height, whereas the cone is defined by its lower radius, upper radius, and height, rotated 360° around the vertical axis.

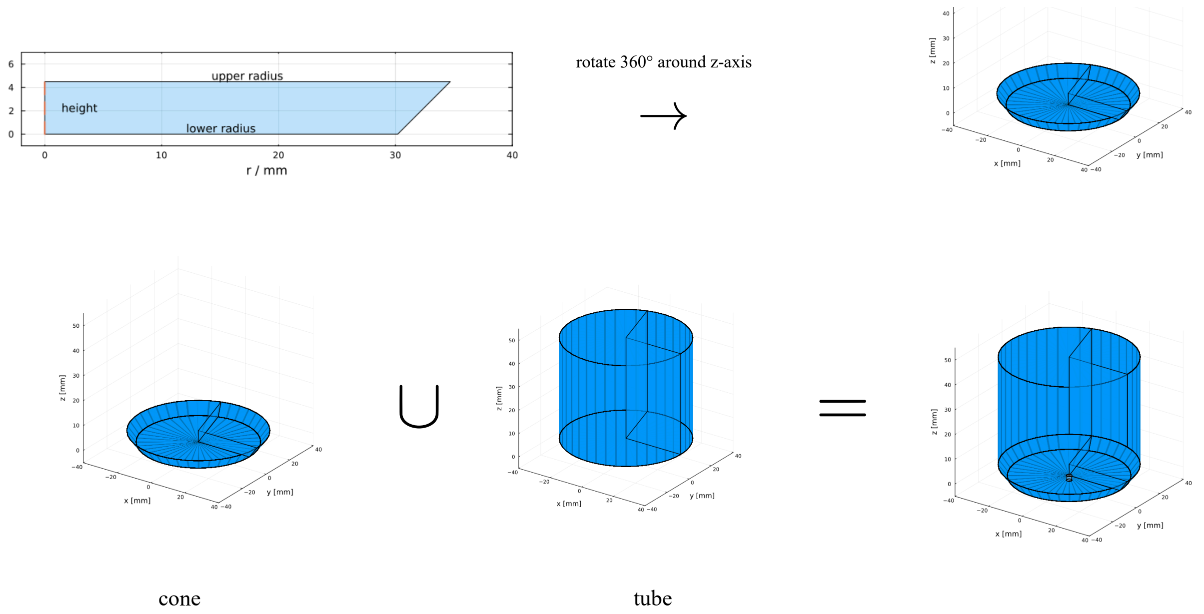

Figure 4.2: Illustration of how the detector bulk of a PPC detector can be constructed as the union of a cone and a cylinder. The cone is defined through a lower and an upper radius, a height, and a 360° rotation around the z-axis.

4.2.3 Impurity models

The impurity profile in HPGe detector is important for the electrostatic properties. SSD allows to use different impurity models that calculate the impurity density throughout the detector volume based on values that were measured during production. A user can define their own impurity model, or use one that is already defined, and pass the necessary parameters.

In SSD it is convention that for p-type semiconductors all impurity values ρ_{imp} are stored as negative numbers as the holes diffuse to the n-type region and thus the fixed electrons remain throughout the bulk.

cylindrical_impurity_model For PPC detectors, the relevant impurity model is the `cylindrical_impurity_model`, as to the colaboration the impurity density for two points in the vertical direction are available.

The user provides the initial impurity concentration $\rho_{\text{imp, }0}$ at $z = z_0$ and $r = r_0$ with a corresponding gradient in the r and z directions. Using the initial impurity concentrations and gradients, SSD then computes the impurity concentration at every point in the bulk of the detector.

Due to the production process for HPGe detectors in L200, the impurity concentrationn in radial direction is uniform and only the z-dependence is considered. During production, the impurity value $\rho_{\text{imp, }0}$ at $z = z_0$ and at a higher point in the crystal $\rho_{\text{imp, }1}$ at $z = z_1$ are measured. The user calculates the linear gradient as

$$\frac{\rho_{\text{imp, 1}} - \rho_{\text{imp, 0}}}{z_1 - z_0},$$

and passes it to the `yaml` config file. Typical values for $\rho_{\text{imp, 0,1}}$ are in the range of $10^9 - 10^{10}\ e/\text{cm}^3$

boule_impurity_model For ICPC detectors, the relevant impurity model is the `boule_impurity_model`, which describes the impurity density in the coordinate system of the original crystal boule. In this model, the impurity distribution is defined along the crystal growth direction, corresponding to the z-axis of the boule.

The impurity density is parameterized as a function of the boule coordinate z, using a linear combination of polynomials and an exponential. The parametrization used in the studies performed in this work is the linear parabolic exponential boule model, which has the following form:

$$\rho_{\text{imp}}(z) = a + b(z_0 - z) + c(z_0 - z)^2 + n \exp((z_0 - z - l)/m) \tag{4.2.1}$$

where a, b, n, l, and m are parameters obtained from measurements during crystal production. Since the detector is cut from the boule, its coordinate system does not necessarily coincide with the boule coordinates. Therefore, a translation between the two systems is required. This is implemented via the parameter z_0, which specifies the position of the detector origin in boule coordinates.

Furthermore, a scale f and offset t can be applied to the impurity $\rho_{\text{imp}}(z)$:

$$f \cdot \rho_{\text{imp}}(z) + t \tag{4.2.2}$$

These parameters are chosen such that the depletion voltage matches the one measured in the experiment.

This approach allows the impurity profile of the detector to be derived directly from the measured impurity distribution of the entire boule, taking into account the position and orientation of the detector within the crystal.

As for the PPC detector, typical impurity values are in the range of $10^9 - 10^{10}\ e/\text{cm}^3$.

4.2.4 Electric potential and field calculation

The electrostatic potential $\phi(\mathbf{x})$ is obtained by solving Poisson's equation with spatially varying permittivity,

$$\nabla \cdot (\varepsilon(\mathbf{x})\, \nabla\phi(\mathbf{x})) \;=\; -\rho_{\text{tot}}(\mathbf{x}), \qquad \varepsilon(\mathbf{x}) = \varepsilon_0\, \varepsilon_r(\mathbf{x}), \tag{4.2.3}$$

where ε_0 is the vacuum permittivity and $\varepsilon_r(\mathbf{x})$ is the relative dielectric constant of the local material. The total space charge density $\rho_{\text{tot}}(\mathbf{x})$ contains (i) the ionized impurity model in the semiconductor and (ii) optional fixed space-charge contributions (e.g. charged surface layers in passive regions).

The applied detector voltages enter as Dirichlet boundary conditions on the electrode/contact surfaces: for each contact i SSD enforces $\phi = \phi_i$ on grid points belonging to the corresponding contact surface. The computational domain is defined by a "world" volume surrounding the detector; cylindrical simulations may exploit φ symmetry and treat the azimuthal coordinate as periodic.

Material interfaces (e.g. HPGe-vacuum or HPGe-LAr) are handled via the spatially varying permittivity $\varepsilon_r(\mathbf{x})$. This enforces the electrostatic interface conditions, namely continuity of ϕ and the correct behaviour of the normal electric displacement field $\mathbf{D} = \varepsilon\mathbf{E}$ across permittivity jumps. Any additional free surface charge can be represented through a volumetric charge density in a thin layer.

The potential is computed on an adaptive 3D grid. SSD starts from an initial grid that resolves geometric features (contacts, surfaces, and material boundaries), then iteratively solves the discretized Poisson equation using successive over-relaxation (SOR) until convergence. Subsequent grid refinements insert additional ticks in regions where the potential difference between neighboring grid points exceeds a user-defined refinement criterion, while enforcing a minimum tick spacing to avoid over-refinement.

After convergence, the electric field is obtained by numerical differentiation,

$$\mathbf{E}(\mathbf{x}) = -\nabla\phi(\mathbf{x}), \tag{4.2.4}$$

and stored on the corresponding grid. In cylindrically symmetric (2D) simulations, the potential can be replicated to a full 2π azimuthal representation prior to field calculation in order to produce a 3D field.

At the interface between detector and surrounding medium, different dielectric constants modify the relation between the electric field $\boldsymbol{E}$ and the electric displacement field $\boldsymbol{D}$. The normal component of $\boldsymbol{D}$ satisfies the boundary condition

$$(\boldsymbol{D}_2 - \boldsymbol{D}_1) \cdot \boldsymbol{n}_{21} = \sigma_s \tag{4.2.5}$$

where σ_s denotes a possible free surface charge density at the interface, $\boldsymbol{D}_i$ denotes the electric displacement field in medium i, and $\boldsymbol{n}_{21}$ is the unit normal vector pointing from medium 1 to medium 2. In the absence of free surface charge, the normal component of $\boldsymbol{D}$ is continuous across the interface. Since $\boldsymbol{D} = \varepsilon\boldsymbol{E}$, a dielectric mismatch can therefore lead to a discontinuity in the normal component of $\boldsymbol{E}$. In the case of LEGEND-200, medium 1 corresponds to the HPGe detector material and medium 2 to the surrounding LAr.

For LAr $\varepsilon_r \sim 1.5$ [58] and for HPGe $\varepsilon_r \sim 16$ [59].

4.2.5 Charge transport

In `SolidStateDetectors.jl`, charge transport is simulated by tracking individual particles: the electron and hole components of each energy deposition are propagated as discrete charge packets in time steps of length Δt, which can be set by the user and defaults to 1 ns. For each event, the user choses the coordinate of the energy-deposition, including charge cloud parameters like radius, energy, and number of point-like charge-carriers within the cloud. All parameters are applied to the electron and hole clouds, which are propagated separately from the same initial position.

At each time step, the displacement of a charge packet is built from the contributions of drift, diffusion, and, self-repulsion, whereas including the effects of diffusion and self-repulsion is optional. In schematic form the drift-step $i+1$ is computed as

$$\boldsymbol{r}_{i+1} = \boldsymbol{r}_i + \Delta\boldsymbol{r}_{\text{drift+self-repulsion}} + \Delta\boldsymbol{r}_{\text{diffusion}} \tag{4.2.6}$$

where the drift step is computed from the local electric field, possibly modified by the field of the other charges in the cloud.

Drift + self-repulion

SSD simulates the displacement of drift and self-repulsion together. More explicitly, SSD first constructs an effective electric field

$$\boldsymbol{E}_{\text{tot}}(\boldsymbol{x}) = \boldsymbol{E}_{\text{det}}(\boldsymbol{x}) + \boldsymbol{E}_{\text{cloud}}(\boldsymbol{x}) \tag{4.2.7}$$

where $\boldsymbol{E}_{\text{det}}$ is the detector field obtained by interpolation on the precomputed field map. $\boldsymbol{E}_{\text{cloud}}$ is the contribution from self-repulsion and is calculated for every charge packet in a cloud as the Coulomb field generated by all other packets in the same cloud. This total field is then passed to the chosen charge-drift model, which returns the carrier velocity $\boldsymbol{v}_{e/h}$. The drift displacement is therefore

$$\Delta\boldsymbol{r}_{\text{drift}} = \boldsymbol{v}_{e/h} \cdot \Delta t \tag{4.2.8}$$

If the user choses to not include self-repulsion in the simulation, $\boldsymbol{E}_{\text{cloud}} = 0$.

SSD supports different drift models. In the simplest case, an electric-field drift model assuming Ohmic behaviour is used, such that

$$\boldsymbol{v}_{e/h} = \mu_{e/h}\boldsymbol{E}_{\text{tot}}. \tag{4.2.9}$$

In this model the drift velocity is parallel to the local electric field and the mobility is treated as isotropic. For HPGe detectors, however, SSD also implements the so-called ADL drift model, which accounts for the anisotropy of charge transport in the crystal, as described in section 2.3.1.

In the ADL model, the drift velocity is not assumed to be parallel to the electric field. Instead, the field is first expressed in the crystal coordinate system, whose orientation with respect to the detector geometry is specified by a rotation matrix. The anisotropy of the carrier motion is then described through parametrizations along the symmetry directions of the crystal together with effective-mass tensors. For holes, the drift along the principal crystallographic axes is parametrized using the empirical velocity laws for the ⟨100⟩ and ⟨111⟩ directions. For electrons, the model additionally includes the multi-valley structure of the conduction band via reciprocal mass tensors for the different valleys. In this way, the drift velocity becomes a function not only of the electric-field magnitude, but also of its orientation with respect to the crystal axes. As a consequence, the simulated trajectories can deviate from the field lines.

Diffusion

The diffusion contribution is treated stochastically as an isotropic random walk. After the drift step has been computed, SSD adds an isotropic random displacement. Its magnitude is determined either from fixed diffusion coefficients $D_{e/h}$ provided in the material properties (i.e. literature values), or, if supported by the chosen drift model, from the local mobility μ through

$$D_{e/h} = \mu_{e/h}\frac{k_B T}{q}$$

For a time step Δt, the diffusion length is taken as

$$\Delta r_{\text{diff}} = \sqrt{6D_{e/h}\Delta t} \tag{4.2.10}$$

The propagation of charge carriers, is repeated until the carriers are collected at an electrode, leave the active detector volume, or the maximum number of drift steps is reached. SSD also contains dedicated boundary handling: if a step crosses into a contact, the carrier is taken as collected; if it reaches a floating boundary, the step is projected onto the local surface, so that surface drift can be approximated. Electrons and holes are tracked independently and can therefore have different total drift times.

Overall, SSD simulates charge transport as the propagation of discrete charge packets in the combined detector and cloud field, with modular drift models and optional stochastic diffusion and self-repulsion. This approach is numerically efficient and sufficiently flexible to reproduce the main transport effects relevant for pulse-shape formation in HPGe detectors.

The output of the charge transport simulation are the trajectories $\boldsymbol{x}_{e/h}$ for electrons and holes respectively. A trajectory $\boldsymbol{x}_{e/h} = [\boldsymbol{r}_{t_1}, ..., \boldsymbol{r}_{t_N}]$ consists of 3D coordinates $\boldsymbol{r}_{\boldsymbol{t_i}}$ that are stored at each time-step during the simulation, where N is the number of time-steps the charges undergo during simulation.

4.2.6 Signal calculation

The signal calculation uses the electron and hole trajectories obtained from the charge-transport simulation as input. It is based on the Shockley-Ramo theorem [35], introduced in Section 2.2.4, which relates the motion of charge carriers inside the detector to the charge induced on a readout electrode. For a given contact k, the induced charge from one electron-hole pair is calculated as

$$Q_k(t) = q\left[W_k(\boldsymbol{x}_h(t)) - W_k(\boldsymbol{x}_e(t))\right], \tag{4.2.11}$$

where $Q_k(t)$ is the charge induced on contact k, W_k is the weighting potential of that contact, and $\boldsymbol{x}_{e/h}(t)$ are the electron and hole trajectories, and q denotes the absolute value of the elementary charge. For several charge carriers, the total induced charge is obtained by summing the individual contributions.

The weighting potential is calculated using the same field solver as for the electric potential ϕ, but with different boundary conditions. The readout contact is set to one, all other contacts are set to zero, and the space-charge density is set to zero throughout the detector. It acts as a geometry-dependent weighting function for the contribution of the carrier to contact k.

The length of an ideal waveform corresponds to the length of a trajectory $\boldsymbol{x}_{e/h}$, where each point in the trajectory $\boldsymbol{r}_{t_k}$ corresponds to a signal value $Q(t_k)$.
The simulated pulse is what is called an ideal waveform, which means that only the signal induced by the moving charges is simulated. In contrast, experimentally measured waveforms include additional effects such as a baseline offset, electronic noise, the finite bandwidth of the readout chain, and the response of the preamplifier. To obtain a more realistic approximation of the measured pulse shape, the ideal waveform is therefore embedded in a longer trace and convolved with an effective detector-response function. One way to model this response is with a convolution of a Gaussian-like bandwidth response with an exponential RC response, with the corresponding time constants tuned to each detector.

Charge trapping

Charge trapping degrades the signal during the charge transport. In the current version of SSD, charge trapping does not affect the transport of the charge carriers itself, but its effect is added during the signal-calculation after the simulation of the transport is finished and the trajectory is determined. In particular, the so-called Boggs charge trapping model [43] (cf. section 2.3.3) is implemented. At each time step t_k the induced charge q_{t_k} (calculated according to the Shockley-Ramo theorem) is reduced by Δq_{t_k}, which depends on the trapping cross-section σ, the density of trapping centers n, and the displacement length $|\Delta \boldsymbol{r}_{t_k}| = |\boldsymbol{r}_{i+1} - \boldsymbol{r}_i|$:

$$\Delta q_{t_k} = q_{t_k} n \sigma |\Delta \boldsymbol{r}_{t_k}| \tag{4.2.12}$$

4.3 EH-Drift

EH-Drift is a simulation framework written in `C` for charge transport and signal formation in HPGe detectors, with particular emphasis on passivated surface events and the influence of surface charge [56]. It builds on the `siggen` framework and extends it to model effects that are especially relevant for surface α interactions, including modified transport along the passivated surface, diffusion, self-repulsion, and the impact of additional surface charge (cf. 2.2.5) on the detector fields. The steps that EH-Drift undergoes in a full simulation are depicted in figure 4.3

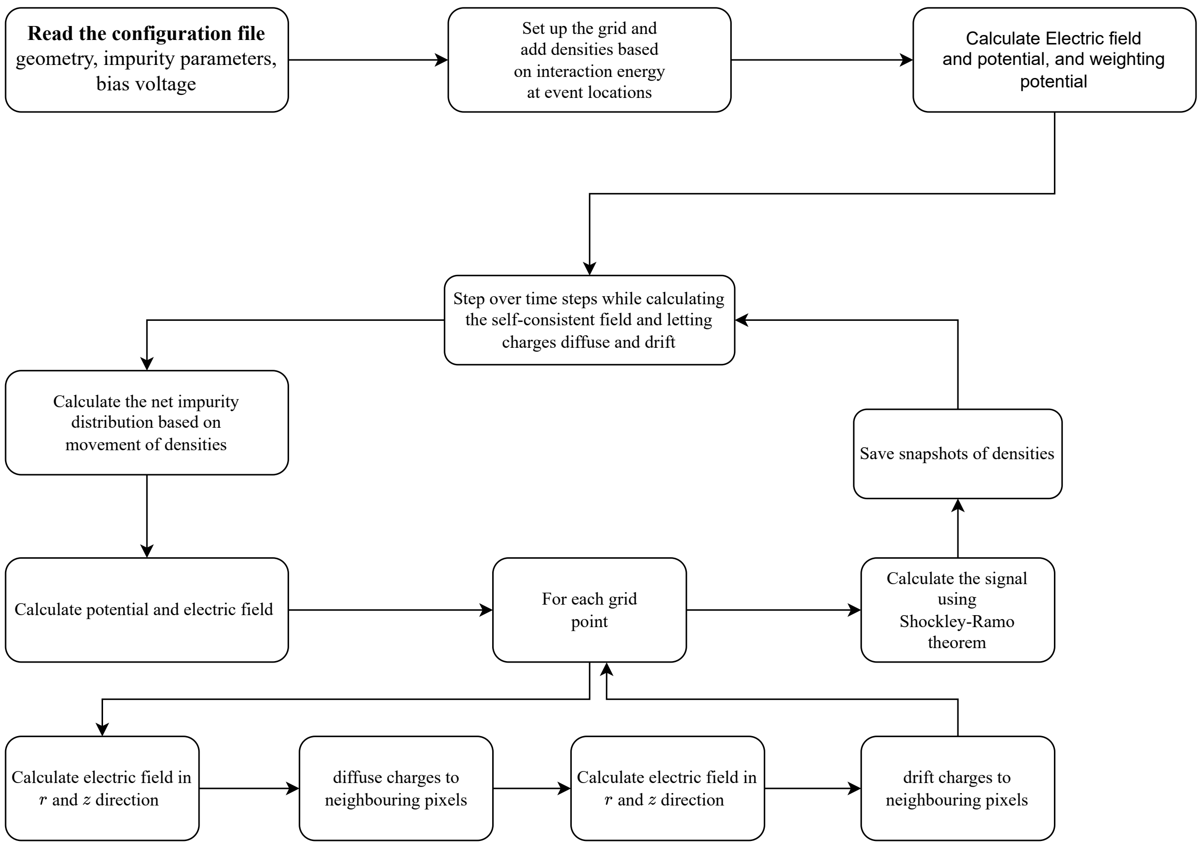

Figure 4.3: Flowchart illustrating the steps undergone in EH-Drift simulations. Figure from [56], with minor adaptations.

4.3.1 Grid initialization and detector simulation

The detector is represented on a two-dimensional (r, z) grid assuming azimuthal symmetry. For a PPC detector, the grid spans the detector cross section from the point contact at the bottom center to the outer radius and top surface. The electric potential and weighting potential are calculated on this grid from the detector geometry, the applied bias voltage, and the impurity profile. For EH-Drift an impurity model equivalent to the cylindrical_impurity_model in SSD with gradient in z direction is available, defined in the same way in the config file. The detector fields are initialized before waveform generation and then used throughout the drift calculation.

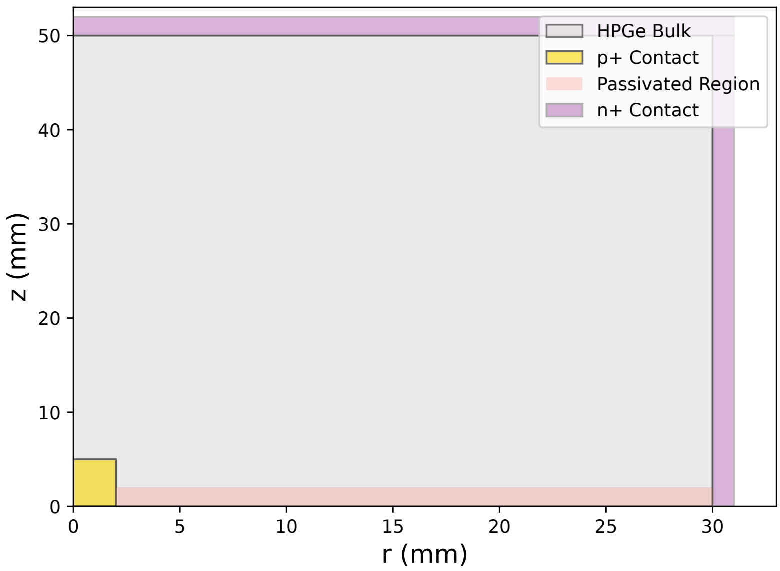

Figure 4.4: Representation of the 2-D grid in EH-Drift for a PPC detector. Figure taken from [56].

Because the numerical grid spacing is typically much larger than the physical thickness of the passivated layer, the passivated surface is implemented effectively as a dedicated region at the detector boundary. Additional surface charge can be specified by the user and is incorporated into the detector model through the field calculation, thereby modifying the electric field and the subsequent signal formation.

A crucial difference between SSD and EH-Drift lies in how the detector boundary is treated in the field calculation. In SSD, the computational domain extends beyond the crystal into the surrounding materials, so changes in the dielectric constant at interfaces such as HPGe–vacuum or HPGe–LAr are included explicitly in Poisson's equation. This allows the continuity of the electric potential and the appropriate behaviour of the normal component of the electric displacement field to be enforced directly across material boundaries. In contrast, the grid on which EH-Drift solves the potential only covers the detector itself and does not explicitly include the surrounding medium.

Instead, the boundary is treated effectively within the finite-difference scheme: conceptually, one introduces artificial grid points just outside the computational domain so that the finite-difference for Poisson's equation can still be evaluated at grid points on the detector boundary. The potential at these ghost points is then set equal to that of the corresponding mirrored interior or boundary points, i.e.

$$\phi(r, z = -1) = \phi(r, z = 0),$$

where $\phi(r, z = -1)$ denotes an artificial potential outside the detector and $\phi(r, z = 0)$ the potential at the detector boundary. This treatment imposes a reflecting Neumann boundary condition, $\partial\phi/\partial n = 0$. The situation is illustrated in figure 4.5.

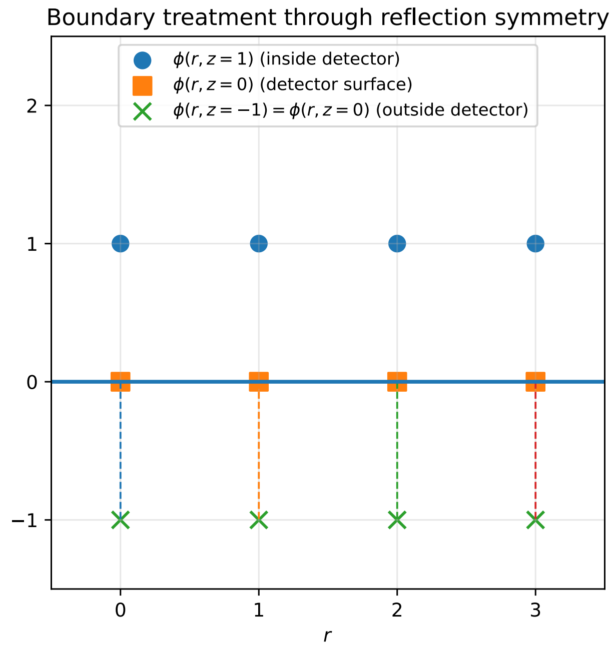

Figure 4.5: Illustration of how EH-Drift handels the potential calculation at the boundary by imposing reflection symmetry. This treatment results in electric fieldlines parallel to the detector surface.

As a result, EH-Drift does not solve the full exterior electrostatics in the same way as SSD, but approximates the influence of the detector boundary within the internal detector grid.

After the potential calculation, EH-Drift calculates the electric field according to equation 4.2.4.

4.3.2 Charge transport

EH-Drift models the motion of charge carriers on a cylindrical (r, z) grid and treats electrons and holes as separate time-dependent charge-density distributions. For a given interaction position and deposited energy, both carrier types are initialized on the grid and then propagated in discrete time steps. The initialized carrier density (both for electrons and holes) is proportional to the deposited energy divided by the energy needed to create an electron hole pair, which is approximately 2.95 eV (cf. 2.2.4).

The transport is formulated in a two-dimensional, azimuthally symmetric approximation, so that the charge cloud is represented as a ring-shaped density rather than as a fully three-dimensional distribution. The local electric field is obtained from the detector potential, and field-dependent drift velocities for electrons and holes are determined from tabulated transport parameterizations. The drift is modelled anisotropically, using the parametrization in equation 2.3.4.

At each time step, the charge densities are first broadened by diffusion and then moved through the detector according to the local drift field, with interpolation between neighboring grid cells to account for motion within a cell. Diffusion is therefore included directly in the charge-density evolution and causes the charge cloud to spread continuously during the transport. In addition, EH-Drift accounts for self-repulsion by updating the effective space-charge distribution from the evolving electron and hole densities and recalculating the electric field during the simulation. The subsequent drift step is then performed in this updated field, so that the carrier motion and the Coulomb interaction of the cloud are treated consistently.

Passivated surface modelling

A special treatment is applied to passivated regions. Charges that drift into a passivated surface are transferred to a dedicated surface-charge distribution, where they continue to propagate with a reduced effective drift velocity controlled by a user-defined surface-drift factor. Depending on the local field configuration, charges can also transfer between the surface layer and the adjacent bulk. This treatment is important for describing the delayed and broadened charge collection characteristic of surface events. The time-dependent electron and hole charge densities obtained from this transport simulation are then used for signal formation via the weighting potential, so that the final waveform naturally includes the combined effects of drift, diffusion, self-repulsion, and surface transport.

4.3.3 Signal calculation

The signal is calculated from the time-dependent electron and hole charge densities using the Shockley-Ramo theorem. At each time step during the transport simulation, the instantaneous carrier distributions are combined with the weighting field to determine the induced signal contribution from all charges present in the detector. The total waveform is therefore built up from the full spatial evolution of the electron and hole clouds rather than from single point-like carrier trajectories. The output is an ideal waveform that encodes the simulation of the charge transport. It has a step-like shape and is normalized so that the height of the waveform reflects the fraction of the initially deposited charge that is collected.

4.4 Simulating passivated surface events

In contrast to EH-Drift, there is currently no model implemented in SSD to simulate events drifting through the passivated surface. In this work, following the same conceptual approach as EH-Drift, surface event simulations were performed, using tools already implemented in SSD. In particular, the use of `passives` volumes and `virtual_drift_volumes` for this purpose was suggested by the authors of EH-Drift.

SSD allows to manipulate the drift velocity of charges moving through the passivated surface. This was implemented by defining a `virtual_drift_volumes` in the region where the passivated surface is expected. By overwriting the method `modulate_driftvectors` the simulated drift velocity is suppressed by a user-chosen factor. This results in a reduction of the overall step-vector, which includes the contributions of drift, diffusion, and self-repulsion.

The other major effect of the passivated surface that was included in the simulation was the effect of additional charge in the passivated surface. This was implemented by defining a `passives` volume, in which the user can define a charge density. The `passives` volume was placed at the bottom of the detector, ranging over the radial distances of the passivated region. Its thickness was chosen to be 20 μm, to reflect the thickness of the grid in EH-Drift, over which the surface charge was distributed.
The implementation of surface charge differs between the two frameworks. In EH-Drift, the surface charge is defined as a two-dimensional distribution on a circular sheet, whereas in SSD it

is represented as a volumetric charge distributed over a thin cylindrical layer with finite height. In the SSD simulations, the thickness of this `passives` region was chosen to correspond to the grid spacing used in EH-Drift ($20\,\mu$m), which is approximately one order of magnitude larger than the expected physical thickness of the passivated surface. The volumetric charge density was then adjusted such that the total integrated charge within this layer reproduces the total integrated surface charge density employed in EH-Drift.

Table 4.1 summarizes the main implementations of SSD, as a comparison to EH-Drift.

	SSD	EH-Drift
Detector grid	3D, adaptive	2D, fixed
Boundary conditions	permittivity jumps	reflection symmetry
Charge carrier representation	point-like, each representing collection of charges	densities across grid cells, one charge carrier per 2.95 eV
Surface charge	distributed over cylindrical `passives` volume (this work)	distributed over rectangular area
Passivated surface modelling	`virtual_drift_volumes`, `modulate_drift_vector`, user-defined surface to bulk velocity factor (this work)	splitting of lowest grid-points, user-defined surface to bulk velocity factor

Table 4.1: Overview of implementations in SSD and EH-Drift.

Chapter 5

Comparison of `SolidStateDetectors.jl` to EH-Drift

This chapter explains the work performed to compare SSD and EH-Drift for the simulation of passivated surface events. The comparison includes both the detector simulation, namely the calculation of the electric potential and electric field, and the subsequent pulse shape simulation. The primary focus is on PPC detectors, since their comparatively large passivated surface makes passivated surface effects particularly relevant. In addition, ICPC detectors are studied because they represent the only detector technology for LEGEND-1000. The simulations are based on detectors deployed in the experiment, using experimentally measured detector parameters as input.

5.1 Detector simulation

The parameters used for the detector simulation (geometry of the bulk and the contacts, bias voltage, and impurity values) were taken from legend metadata.

For the PPC detector, the config file was created manually for SSD, while for EH-Drift the config file created by the author was used. In both frameworks the `cylindrical_impurity_model` was used. The linear gradient in z-direction was manually calculated from the two impurity values provided. These numbers matched the ones used in EH-Drift.

For the ICPC detector, the config file was automatically generated by SSD. The `passives` volume and `virtual_drift_volumes` were manually added in the SSD config file. In SSD we use the `boule` impurity model, which is not available for EH-Drift, which uses the `cylindrical_impurity_model`.

As explained in sections 4.2.4 and 4.3.1, the handling of boundary conditions differs between the two frameworks, leading to different electric field behaviour near the detector surface due to induced surface charge σ_s at the interface between HPGe and LAr.

To test whether SSD is able to reproduce the field-calculation of EH-Drift with reflection symmetry, a world was defined that ends at the bottom of the detector, while imposing reflection symmetry at the boundary. The vertical components of the electric field were then compared

Simulation parameters

The detector simulations in both frameworks were based on experimentally determined parameters from detectors deployed in the LEGEND-200 experiment. Only the parameters directly relevant for the electric field calculation are summarized here; detailed geometry definitions are omitted for brevity.

Where possible, the same parameters were used in both frameworks. For the ICPC detector, EH-Drift uses a cylindrical impurity model, whereas in SSD the parabolic exponential boule impurity model was used (cf. equation 4.2.1 and expression 4.2.2). The relevant parameters are listed in table 5.1, and the parameters for the parabolic exponential model in table 5.2.

	PPC	ICPC
Name	P00698A	V07647A
Bias voltage [V]	3000	2700
Impurity model	cylindrical	SSD: parabolic exponential boule EH-Drift: cylindrical
Impurity at $z = 0$ [e/mm^3]	-1.11×10^7	-7.4×10^6
Impurity gradient (z) [e/mm^4]	9.62×10^4	3×10^4 (EH-Drift)

Table 5.1: Relevant simulation parameters for the PPC and ICPC detectors used in this work. For the ICPC detector, the impurity values are only defined for the cylindrical impurity model employed in EH-Drift, while SSD uses a parabolic exponential boule model, whose values are shown in table 5.2.

Parameter	Value
a [e/mm^3]	-7.923×10^6
b [e/mm^4]	0.0
c [e/mm^5]	-358.5
l [mm]	32.4
m [mm^3]	9.6
n [C/mm^3]	-231.6
z_0 [mm]	70.3
f [-]	0.93
t [e/mm^{-3}]	-3.169×10^5

Table 5.2: Parameters for the parabolic exponential boule impurity model (equation 4.2.1) used for the ICPC detector V07647A in SSD. The parameters f and t are the scale and offset applied to the impurity profile to match the experimentally measured depletion voltage (equation 4.2.2).

5.2 Pulse shape simulation

5.2.1 Simulation setup

Events were simulated on a two-dimensional (r, z) grid, with each event depositing an energy of 2039 keV. The simulations were performed using identical physical parameters in both frameworks wherever possible.

A surface-to-bulk velocity factor of 10^{-3} was applied in all simulations. For PPC detectors, three different surface charge densities were considered (-0.15, 0.0, and 0.15) $\times 10^{10} \frac{e}{\text{cm}^2}$, whereas for ICPC detectors only the case $\sigma = 0$ was studied, as surface charge effects are expected to be less significant. Charge diffusion and self-repulsion were included in all simulations. In SSD spherical charge clouds with 100 charge carriers were simulated, with the deposited energy equally distributed over the point-like charge carriers. The choice of 100 charge carriers was chosen as a compromise between computational efficiency and numerical accuracy. This trade-off is illustrated in figure 5.1, where a waveform of the same event was simulated three times, each time with a different amount of charge carriers per cloud.

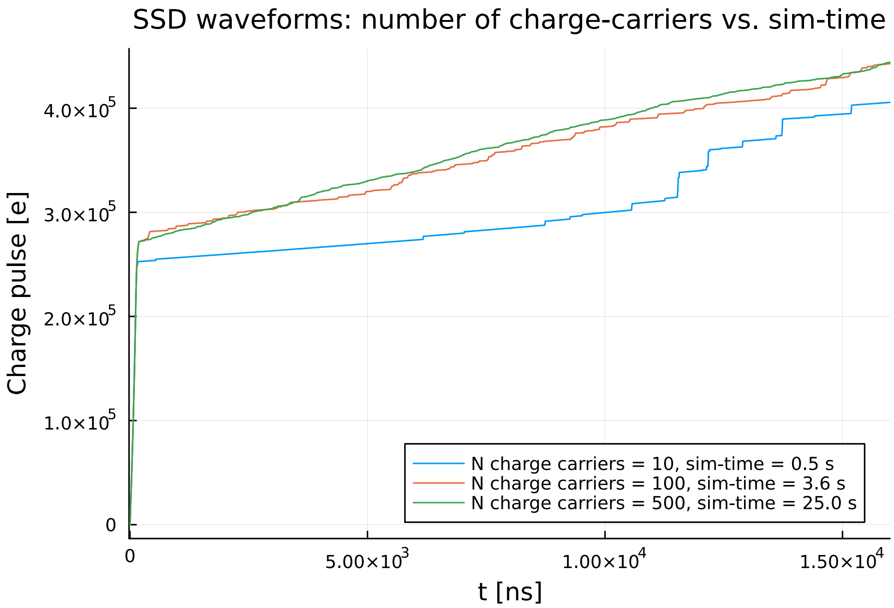

Figure 5.1: Simulated charge pulses for the same event with $E = 2039\,\mathrm{keV}$ near the passivated surface of a PPC detector, using different numbers N of point-like charge carriers per cloud. The corresponding simulation times are shown in the legend. Increasing N improves the sampling of charge-cloud effects, but also increases the computational cost. In this example, values larger than $N = 100$ lead only to small changes in the waveform while requiring substantially longer simulation times. Each simulation was run with 16000 simulation steps.

The spatial distribution of simulated events covers the full detector volume, with an increased sampling density near the passivated surface. This region is of particular interest, as waveform characteristics exhibit the strongest spatial dependence there.

For the studies with the detector V07647A waveforms that were kindly provided by the author of EH-Drift, Kevin Bhimani, were used. We simulated some additional waveforms ourselves in regions of interest. In SSD we then simulated events at the same locations in the detector.

5.2.2 Post-processing and comparison metrics

To enable a direct comparison between SSD and EH-Drift, several observables were defined based on the simulated charge pulses. The SSD waveforms were downsampled to a sampling interval of 16 ns to match both EH-Drift output and experimental conditions, except for the activeness study, where the sampling frequency of 1 ns, corresponding to the simulation time-step in SSD, was kept. Furthermore, the SSD charge pulses were normalized to their initially deposited energy, such that the signal values correspond to the fraction of collected charge. The output of EH-Drift already is in this form.

Activeness The activeness is defined as the ratio of collected to deposited energy,

$$\text{activeness} = \frac{E_{\text{collected}}}{E_{\text{deposited}}} \tag{5.2.1}$$

This quantity and its evaluation procedure follow the approach introduced in [56], where it was used in the context of EH-Drift simulations. The implementation used in this work is based on that study, with minor adaptations to interface also with the present simulation framework.

The activeness is estimated by applying a trapezoidal filter to the normalized charge pulses. To ensure consistent processing, SSD waveforms were extended with a flat tail such that all waveforms have identical length prior to filtering. The resulting activeness values were evaluated at each simulated (r, z) position and interpolated to obtain spatial maps.

In figure 5.2 the simulated waveforms of a typical passivated surface event, simulated with SSD and EH-Drift is shown, together with the output of the trapezoidal filter used to estimate the activeness.

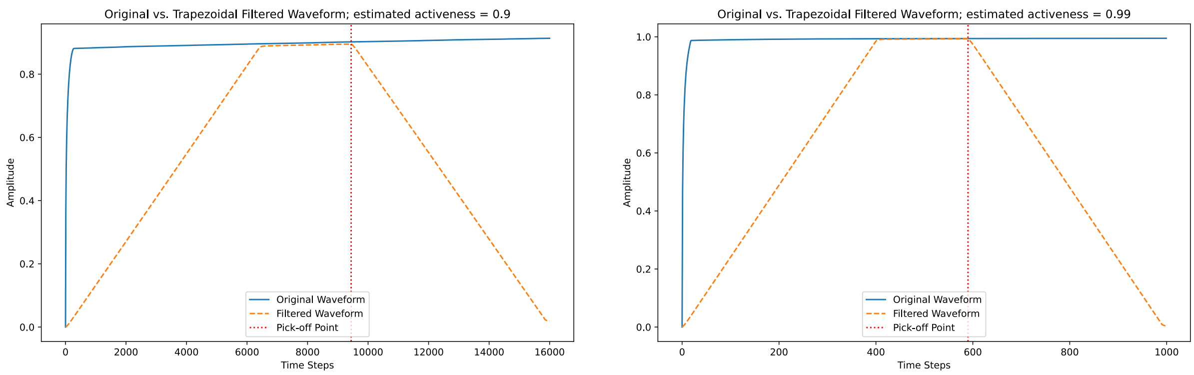

Figure 5.2: Example waveforms of an event near the passivated surface in a PPC detector, simulated with SSD (left) and EH-Drift (right). The blue curves show the ideal charge pulse, normalized to the initially deposited energy. The red dashed curve is the output of the trapezoidal filter, which is used to estimate the energy collection efficiency (activeness). In both simulation frameworks, the primary interaction of the event is located at $(r, z) = (11.0, 1.28)$ mm with a deposited energy of $E = 2039$ keV. In the SSD simulation one time-step corresponds to 1 ns, while in EH-Drift one time-step corresponds to 16 ns.

***A/E* parameter** To compute the A/E parameter, the charge pulses were first convolved with a Gaussian response function including an exponential tail with $\tau = 25$ ns, approximating the detector response. This smoothing suppresses numerical artifacts and enables a stable calculation of the current signal via differentiation. Since the charge pulses are normalized, the maximum current amplitude directly corresponds to the A/E value. The resulting A/E distributions were then compared between the two frameworks.

Waveform residuals and RMS A direct waveform comparison was performed by evaluating the residual between SSD and EH-Drift charge pulses. Prior to this, the smeared waveforms were temporally aligned using the position of their maximum current amplitude. The residual waveforms were analysed both visually and quantitatively using the root mean square (RMS) of the difference. The RMS values were mapped onto the (r, z) grid to assess spatial variations in the agreement between the two frameworks.

Chapter 6

Surface-event simulation results

This chapter presents the results of the comparison between `SolidStateDetectors.jl` and EH-Drift described in Chapter 5 for zero and negative surface charge. The results with positive surface charge are presented in the appendix. The results are organized by detector geometry.

6.1 PPC detector (P00698A)

6.1.1 Detector simulation

Analysing the vertical components of the electric field shows that imposing reflection symmetry in SSD reproduces the behvaiour from EH-Drift.

However, when the dielectric interface between HPGe and LAr is taken into account, the different dielectric constants modify the boundary condition relating the electric field $\boldsymbol{E}$ and the electric displacement field $\boldsymbol{D}$. As a result, the electric field near the passivated surface is distorted, and its vertical component points in the negative z direction, as shown in figure 6.1. This effect is crucial for the charge-transport simulation near the passivated surface.

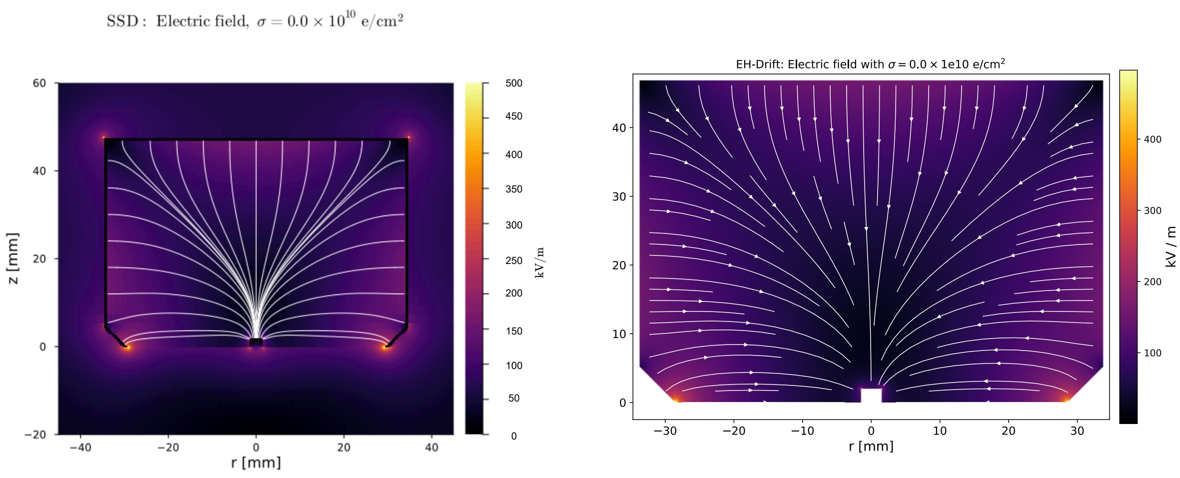

Figure 6.1: Comparison of the electric field in a PPC (P00698A) detector, calculated by SSD (left, using dielectric interfaces at detector boundaries) and EH-Drift (right), without adding additional surface charge to the passivated surface.

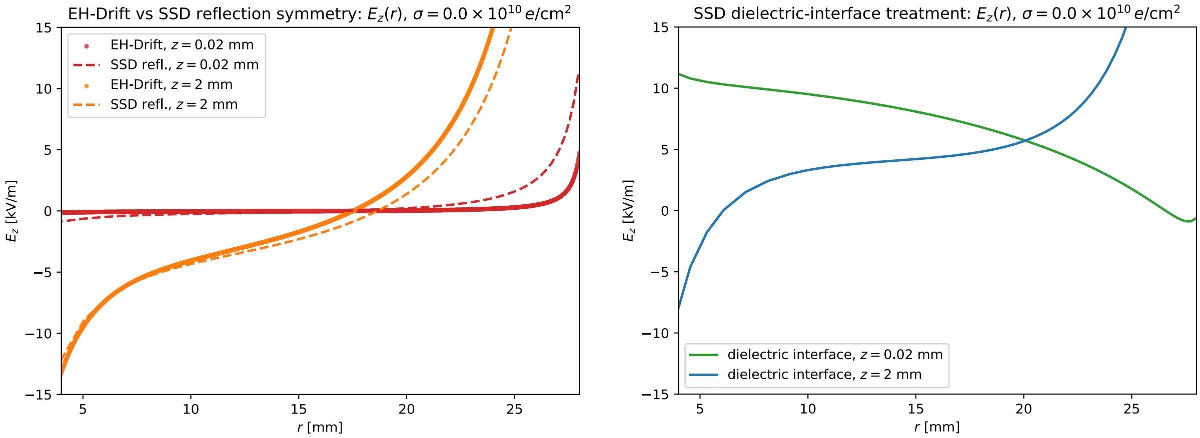

Figure 6.2: Vertical component of the electric field $E_z(r)$ in the vicinity of the passivated surface, calculated by EH-Drift and SSD. For EH-Drift reflection symmetry is imposed at the boundary (left plot, solid curves), while for SSD two boundary treatments are shown, reflection symmetry (left plot, dashed curves) and taking into account the dielectric interface (right plot, blue and green curves).

6.1.2 Pulse shape simulation

Waveform residuals and their RMS

The charge pulses obtained with EH-Drift and SSD, together with their residuals, are shown in Fig. 6.3. The z-coordinate of each simulated event is encoded in the color scale. Results are presented for three surface charge densities, $\sigma = (0.0, -0.15, +0.15) \times 10^{10}\mathrm{e/cm}^2$.

For the case without surface charge ($\sigma = 0$), the agreement between the two frameworks is generally good. The maximum absolute residual reaches approximately 0.03 for normalized waveforms. The agreement is best for events located at larger z values, i.e. deeper in the detector bulk, while larger deviations are observed for events close to the passivated surface.

Introducing a negative surface charge ($\sigma = -0.15 \times 10^{10}\mathrm{e/cm}^2$) leads to significantly larger discrepancies. The maximum residual increases to approximately 0.15, with elevated deviations extending several centimeters into the bulk. At larger depths (on the order of 10 cm), the agreement improves again, and residuals below 0.01 are observed.

Overall, the residuals exhibit a clear spatial dependence, with the largest discrepancies consistently occurring in regions close to the passivated surface, where the electric field configuration is most sensitive to the treatment of boundary conditions and additional surface charge effects.

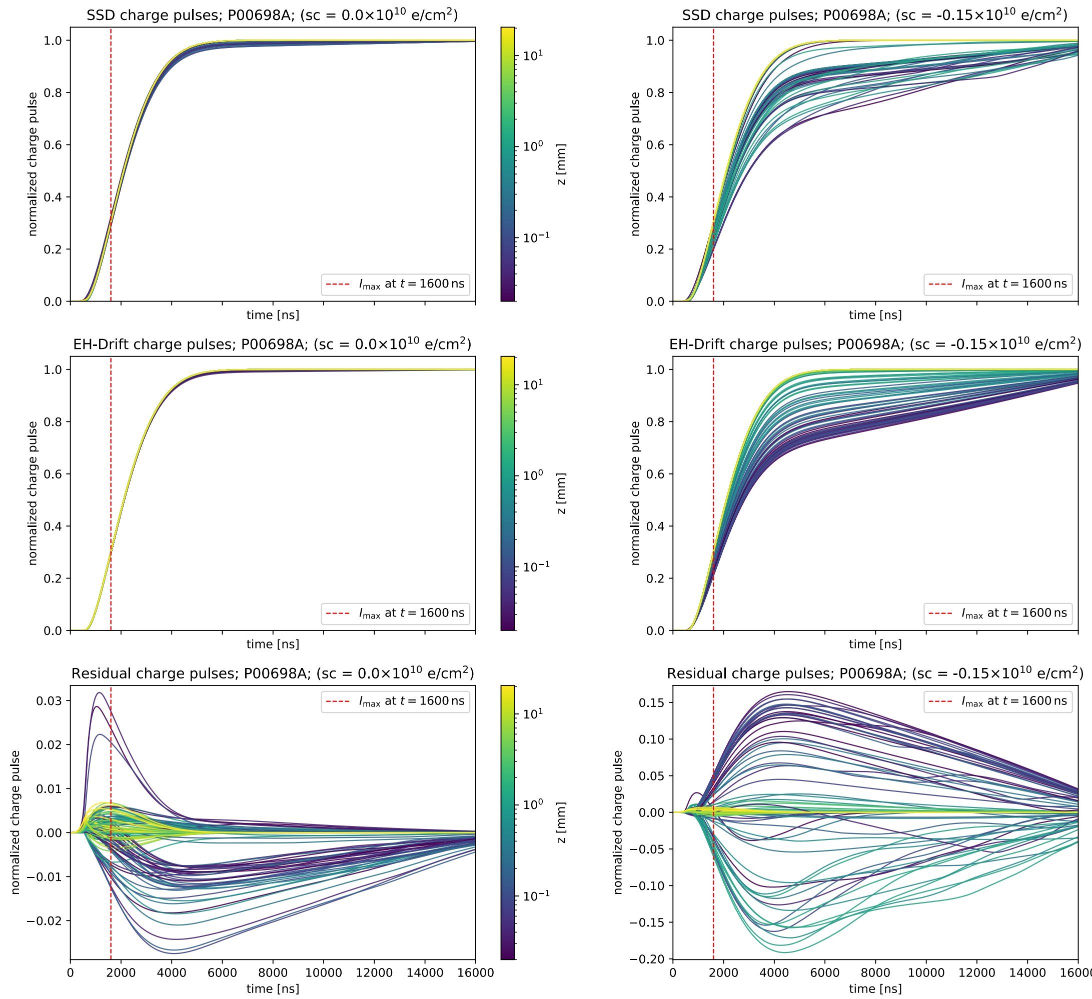

Figure 6.3: Charge pulses of SSD and EH-Drift and their residuals in a PPC detector (P00698A) for different values of surface charge. The waveforms are time-aligned to their maximum current amplitude (red dashed line) and the z coordinate of the event is color-coded. The residuals are calculated as SSD minus EH-Drift, which means regions where the residuals are negative, are regions where the EH-Drift waveform has a higher value than the SSD waveform. For each surface charge value, a total of 108 waveforms are plotted.

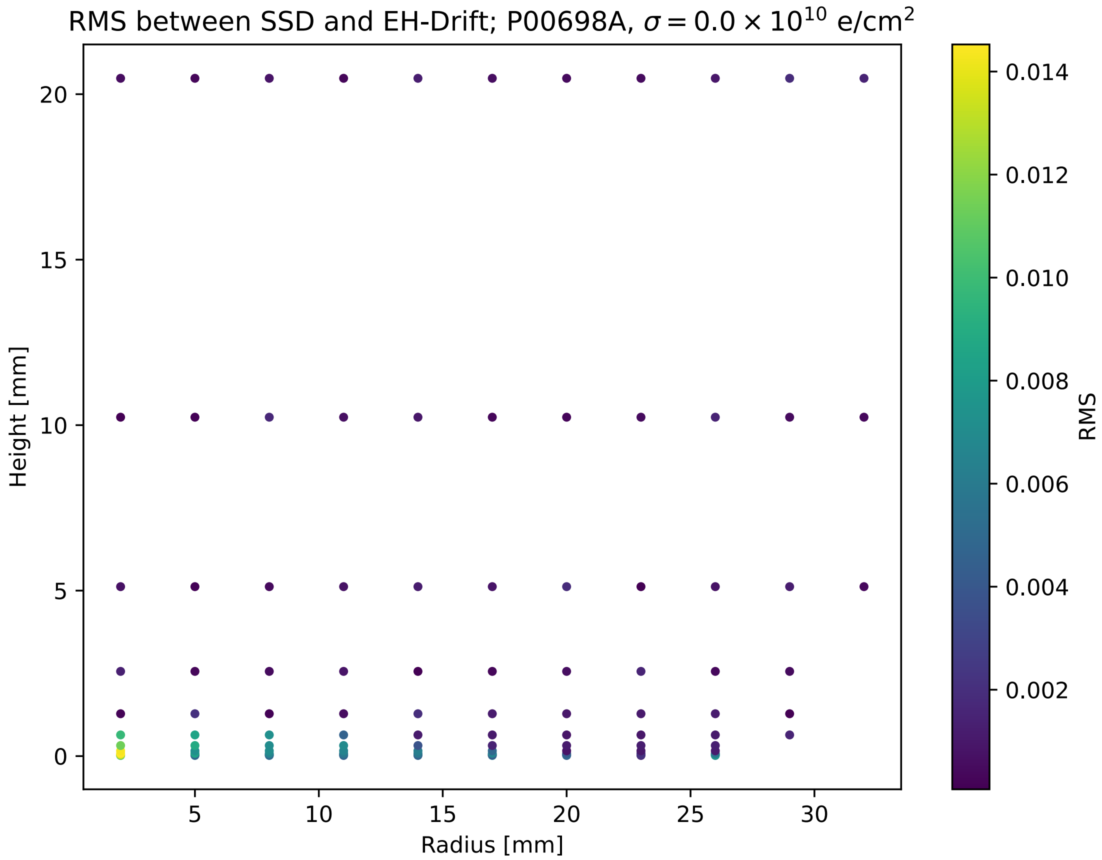

Figure 6.4: RMS map between SSD and EH-Drift for a PPC detector (P00698A) for zero (left) and negative (right) surface charge values.

A/E parameter

The spatial distribution of the A/E parameter for SSD and EH-Drift is shown in figure 6.5. In both frameworks, reduced A/E values are observed for events near the passivated surface.

For zero surface charge ($\sigma = 0$), this reduction is significantly stronger in SSD than in EH-Drift. While both frameworks show a localized suppression close to the surface, SSD predicts systematically lower A/E values and a stronger spatial gradient.

In the presence of negative surface charge ($\sigma = -0.15 \times 10^{10}\mathrm{e/cm}^2$), the suppression of A/E extends further into the detector bulk in both frameworks. This effect is considerably stronger in SSD, where the region of reduced A/E reaches deeper into the detector.

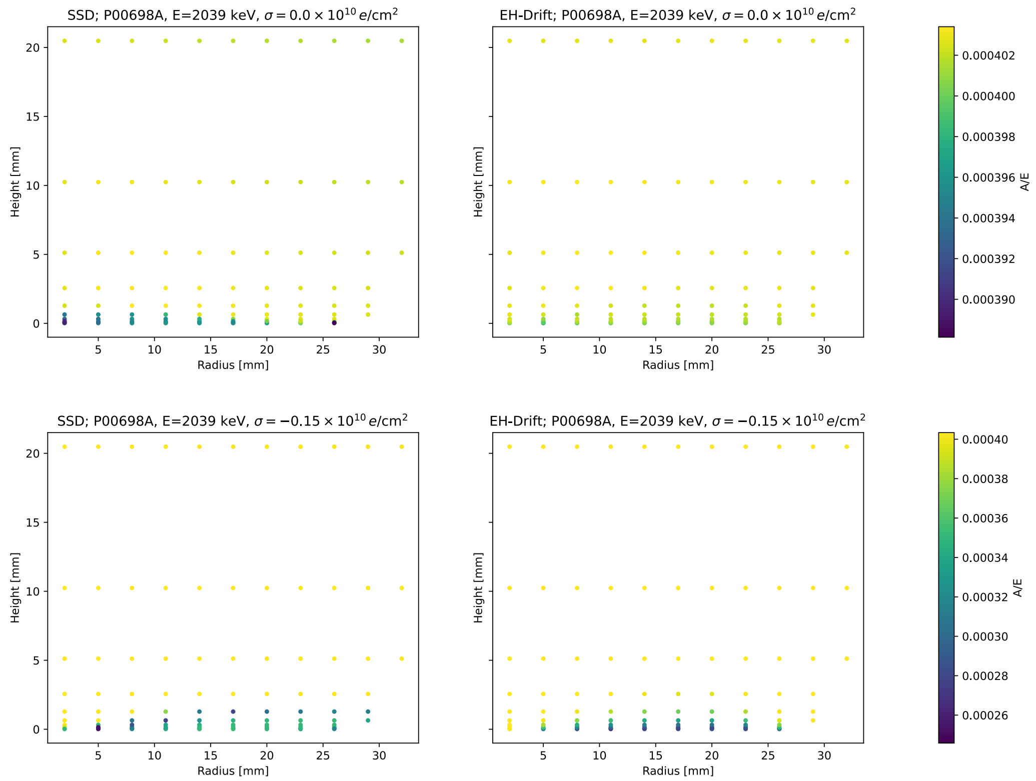

Figure 6.5: A/E parameter of events simulated in a PPC detector, comparing SSD and EH-Drift for different surface charge values. Events were simulated near the passivated surface and in the detector bulk.

Activeness

The interpolated activeness maps for SSD and EH-Drift are shown in figure 6.6. In both frameworks, a reduction in activeness is observed near the passivated surface, indicating incomplete charge collection for surface events.

For zero surface charge ($\sigma = 0$), SSD exhibits a higher reduction in activeness compared to EH-Drift. The region of incomplete charge collection is larger and extends further from the surface. This behaviour is consistent with the modified electric field near the detector boundary in SSD, which affects the drift paths and increases the probability of charge loss.

In the case of negative surface charge ($\sigma = -0.15 \times 10^{10}, \mathrm{e/cm^2}$), the reduction in activeness becomes more significant in both frameworks. However, the spatial extent of this effect is again larger in SSD, where the region of reduced activeness penetrates deeper into the detector bulk. This indicates a stronger influence of surface charge on charge transport when combined with the boundary treatment implemented in SSD.

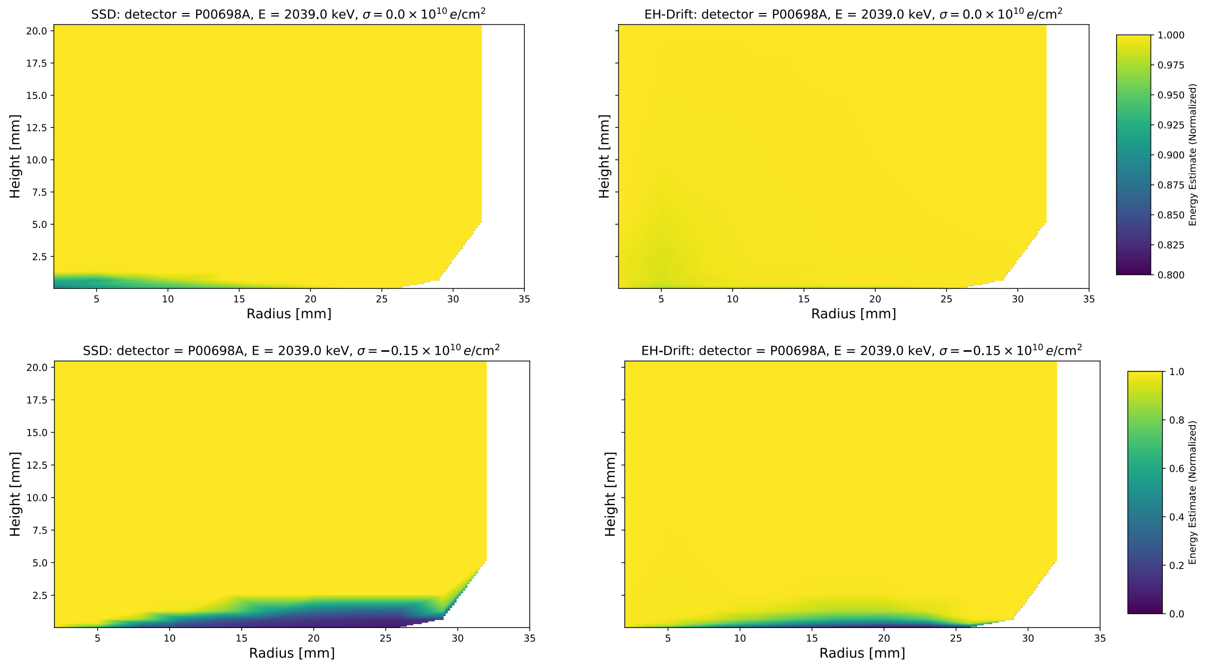

Figure 6.6: Activeness maps of SSD (left) and EH-Drift (right) for different surface charge values. Without adding additional surface charge ($\sigma = 0$) in the passivated region, a significantly energy degraded region is observed in SSD, due to the negative surface charge σ_s at the interface between HPGe and LAr, causing holes to drift through the passivated region. For the $\sigma < 0$ (bottom) energy degradation is higher in SSD than EH-Drift, since the effects of σ_s and σ add up.

Typical passivated surface events and their drift paths for different surface charge values in a PPC detector, as simulated in SSD, are shown in the appendix in figure 7.1.

6.2 ICPC detector (V07647A)

In this section, the simulation results for the ICPC detector are presented. In contrast to the PPC detector studied previously, surface-related effects are expected to be less pronounced due to the different detector geometry and electric field configuration. In particular, charge carriers generated near the passivated surface are not expected to drift through extended low-field surface regions as observed in PPC detectors.

The comparison between SSD and EH-Drift for ICPC detectors therefore focuses primarily on verifying the consistency of the detector and pulse shape simulations in the absence of strong surface-drift effects. Particular attention is nevertheless given to the treatment of events close to the passivated surface, since this region is most sensitive to differences in boundary conditions and charge transport models.

6.2.1 Limitations of the simulation setup

Before presenting the comparison results, several limitations of the present ICPC simulations must be discussed.

In SSD, no drift of charge carriers toward the passivated surface is observed for the ICPC geometry. This differs significantly from the PPC case, where charges generated near the detector surface drift through extended low-mobility regions along the passivated surface. Instead, the electric field configuration in the ICPC detector guides charge carriers predominantly through the detector bulk.

As a consequence, charge carriers initialized near the passivated surface do not exhibit the characteristic slow surface drift observed in PPC detectors. Surface-related effects on the waveform formation are therefore expected to be considerably weaker in the ICPC geometry.

Furthermore, numerical limitations occur in SSD, when events are initialized too close to the passivated surface. In such cases, individual point charges of the simulated charge cloud can leave the detector volume already during the first drift step. These charges are subsequently lost and no longer contribute to the induced signal, leading to artificially degraded waveforms. This behaviour is not interpreted as a physical effect of incomplete charge collection, but rather as a limitation of the present simulation approach. These limitations were not present in the simulations with the PPC detector. It could not be verified whether EH-Drift handles these situations differently.

Due to these effects, the present study does not fully probe charge transport in the immediate vicinity of the passivated surface for ICPC detectors. The comparison between SSD and EH-Drift is therefore effectively restricted to regions where stable charge transport within the detector volume is ensured.

6.2.2 Qualitative waveform comparison

We begin by comparing charge pulses simulated near the passivated surface for different surface charge densities, as shown in figure 6.7. In both frameworks, the waveform shapes exhibit only a weak dependence on the surface charge density.

This behaviour contrasts strongly with the PPC detector, where surface charge substantially modifies the charge transport near the passivated surface and leads to significant changes in the waveform shapes. For the ICPC detector, the influence of surface charge on pulse formation appears to be minor, indicating that surface-related drift effects are considerably less important for this detector geometry.

Some SSD waveforms exhibit degraded charge collection. However, this behaviour is not associated with physical slow surface drift, but originates from the simulation artifact discussed above, namely charge carriers leaving the detector volume during the drift simulation. Since this effect does not exhibit a systematic dependence on the surface charge density, it does not alter the conclusion that surface charge has only a minor impact on waveform formation in the ICPC detector.

Based on these observations, the following quantitative comparisons are restricted to the case of zero surface charge density ($\sigma = 0$).

6.2.3 Detector simulation

The electric fields calculated with SSD and EH-Drift for the ICPC detector are shown in Fig. 6.8. In contrast to the PPC detector, both frameworks yield very similar electric field configurations throughout the detector volume, including regions close to the passivated surface. No strong distortion of the electric field toward the passivated surface is observed in SSD, despite the inclusion of dielectric interfaces at the detector boundaries. This is consistent with the absence of significant surface drift effects in the waveform simulations. The electric field configuration in the ICPC geometry predominantly guides charge carriers through the detector bulk rather than along the passivated surface.Overall, the detector simulations indicate good agreement between SSD and EH-Drift for the ICPC detector. In particular, the strong near-surface differences

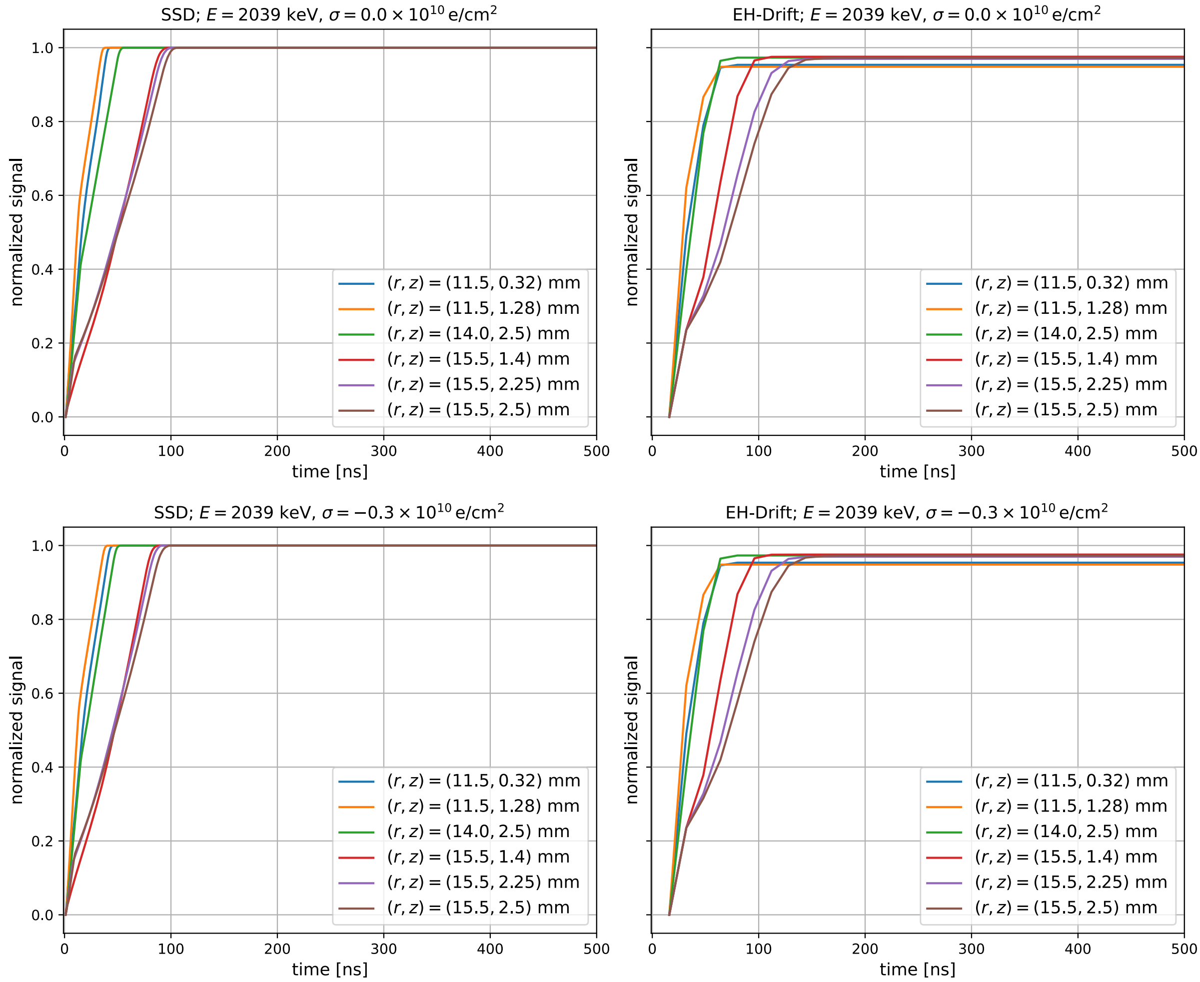

Figure 6.7: Charge pulses of events simulated near the passivated surface in an ICPC detector (V07647A) for different surface charge densities, comparing SSD and EH-Drift. In both frameworks, the waveform shapes exhibit only a weak dependence on the surface charge density, indicating that surface charge effects are minor for this detector geometry. Based on this observation, the following ICPC studies are restricted to the $\sigma = 0$ case.

observed in the PPC detector are not present for the ICPC geometry, suggesting that boundary-condition effects play a less important role in this case.

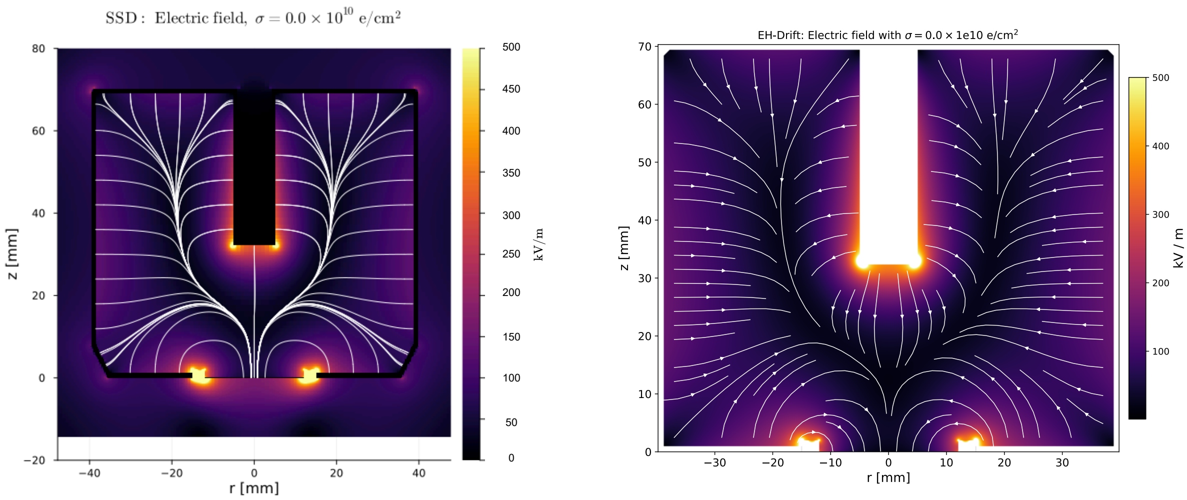

Figure 6.8: Comparison of the Electric field in a ICPC (V07647A) detector, calculated by SSD (left, using dielectric interfaces at detector boundaries) and EH-Drift (right), without adding additional surface charge to the passivated surface. The electric field-calculation appears to be consistent between the two frameworks.

6.2.4 Pulse shape simulation

Waveform residuals and their RMS

The comparison of charge pulses obtained with SSD and EH-Drift for the ICPC detector is shown in Fig. 6.9. The residuals between the normalized waveforms are very small across all simulated positions. The maximum deviations are within ± 0.006, indicating excellent agreement between the two frameworks.

The spatial distribution of the residuals does not exhibit a clear dependence on the event position. This is confirmed by the RMS map shown in Fig. 6.9. The RMS values are uniformly small throughout the detector volume, with values ranging from approximately 2×10^{-4} to 1.6×10^{-3}. The largest RMS values are observed in the detector bulk, although the magnitude remains negligible.

Overall, the waveform comparison demonstrates that SSD and EH-Drift yield nearly identical pulse shapes for the ICPC detector. In contrast to the PPC case, no significant discrepancies are observed near the passivated surface, indicating that surface-related effects are significantly less relevant for this detector geometry.

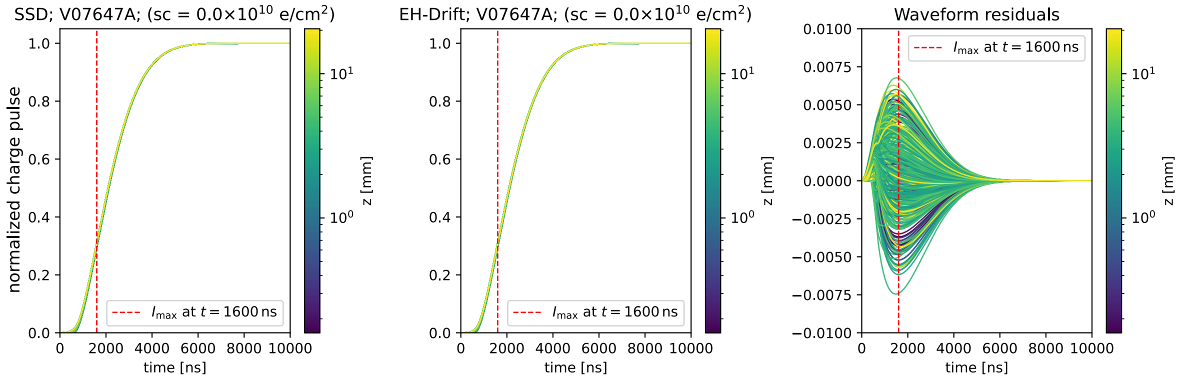

Figure 6.9: Charge pulses of SSD and EH-Drift and their residuals in an ICPC detector (V07647A). The z-coordinate of the event is color-coded; the magnitude of the residual waveform does not appear to depend on it.

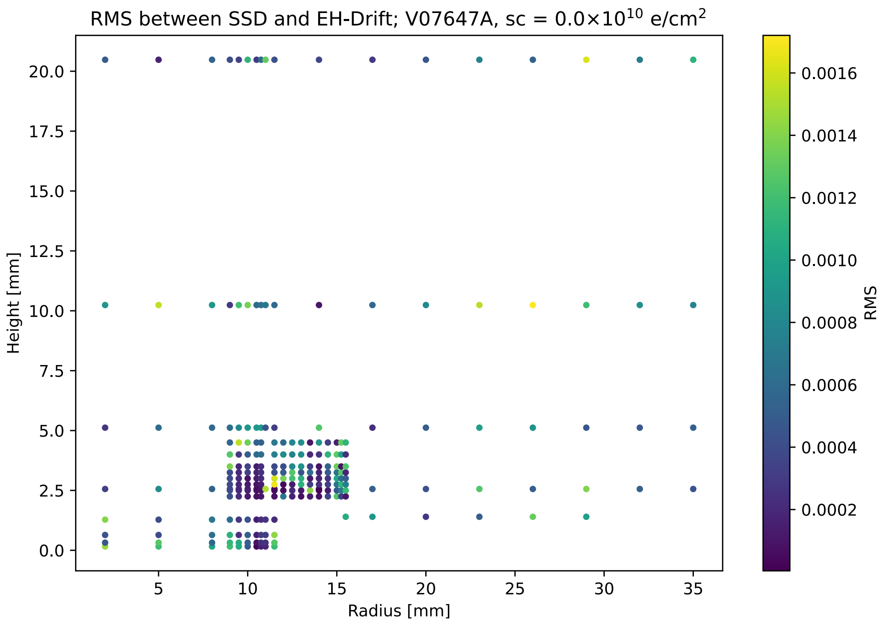

Figure 6.10: RMS of the residual waveforms between SSD and EH-Drift in an ICPC detector (V07647A).

A/E parameter

The spatial distribution of the A/E parameter is shown in figure 6.11. The results obtained with SSD and EH-Drift are nearly indistinguishable across the entire detector volume.

The A/E values lie in a narrow range between approximately 3.99×10^{-4} and 4.03×10^{-4} for both frameworks. The spatial patterns are highly consistent, with no significant deviations observed either in the detector bulk or near the passivated surface.

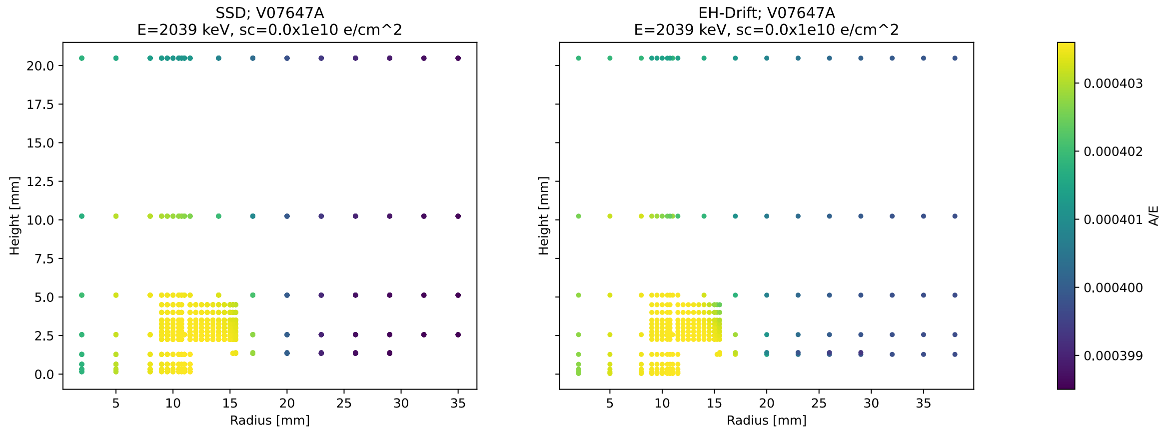

Figure 6.11: A/E values at 2039 keV in an ICPC (V07647A) detector, comparing SSD and EH-Drift.

Activeness

The activeness maps for SSD and EH-Drift are shown in figure 6.12. In SSD, full charge collection is observed throughout the entire detector volume, including regions close to the passivated surface.

In EH-Drift, the behaviour is largely consistent with SSD, with full energy collection in most of the detector. However, a localized region near the passivated surface exhibits reduced activeness of approximately 90%. Outside this region, the activeness remains close to 100%.

This discrepancy is small and spatially limited, but it indicates a difference in the treatment of charge transport close to the detector boundary. In SSD, charge carriers are not allowed to move through the passivated surface. In contrast, this behaviour could not be explicitly verified for EH-Drift. It is therefore possible that differences in boundary handling contribute to the observed deviation.

It should also be noted that in SSD, we were not able to initialize charge carriers arbitrarily close to the passivated surface, as this would lead to trajectories exiting the detector volume within one timestep. Such configurations were excluded from the present study to ensure a consistent comparison between both frameworks.

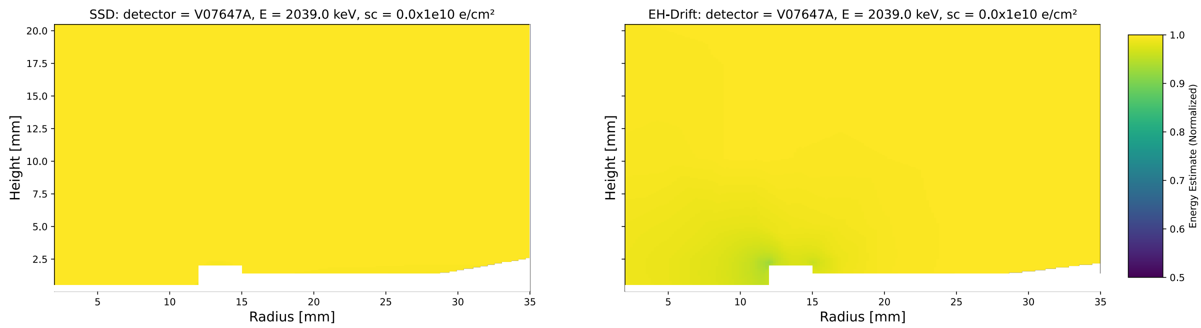

Figure 6.12: Linearly interpolated activeness maps of an ICPC detector (V07647A) for SSD and EH-Drift.

In summary, all comparison metrics show very good agreement between SSD and EH-Drift for the ICPC detector. Deviations are small and do not exhibit a clear spatial structure, indicating that boundary-condition effects, which dominate the PPC comparison, are of minor importance for this detector geometry.

It should be noted, however, that the present comparison is limited by the fact that events could not be placed arbitrarily close to the passivated surface in SSD without leading to unphysical charge transport outside the detector volume. As a result, the study does not fully probe the behaviour of both frameworks in the immediate vicinity of the passivated surface. It therefore cannot be excluded that larger differences may arise for events located closer to the surface than those considered here.

Chapter 7

Conclusion and outlook

In this thesis, pulse shape simulations of events close to the passivated surface of high-purity germanium detectors were studied using the SSD simulation framework and compared to simulations performed with EH-Drift. The main objective was to evaluate whether SSD can reproduce the surface-event behaviour previously studied with EH-Drift, and to identify differences in how the simulations are implemented and how they affect the simulated waveforms.

The study focused on two detector geometries relevant for the LEGEND experiment: a PPC detector and an ICPC detector. PPC detectors were investigated in detail because their comparatively large passivated surface makes them particularly sensitive to surface-related charge transport effects. ICPC detectors were included because they represent the detector technology foreseen for LEGEND-1000, although passivated surface-drift effects are expected to be less important for this geometry.

For the PPC detector, the comparison of the detector simulations showed that the treatment of the detector boundary has a significant influence on the electric field close to the passivated surface. When reflection symmetry is imposed in SSD, the vertical component of the electric field agrees well with the field calculated by EH-Drift. In contrast, when the dielectric interface between HPGe and LAr is taken into account, a dielectric mismatch between the electric and displacement field leads to a discontinuity in the normal component of the electric field. This modifies the electric field close to the passivated surface and changes the direction and strength of the field components relevant for surface charge transport. This difference is important because charge carriers generated close to the passivated surface can drift through regions of reduced mobility, leading to delayed charge collection and modified pulse shapes.

The pulse shape comparison for the PPC detector confirmed that both frameworks predict qualitatively similar surface-event behaviour. Events close to the passivated surface show slow pulse components and reduced charge collection, depending on the applied surface charge density. This indicates that SSD is able to reproduce the general physical mechanism of surface drift that is implemented in EH-Drift. However, quantitative differences were observed. The waveform residuals and their RMS values show that the agreement between the frameworks is good for events in the detector bulk, while larger discrepancies occur close to the passivated surface. These deviations are strongest for negative surface charge and are reduced, but still present, for positive surface charge. The spatial structure of the RMS maps indicates that the differences are not random numerical fluctuations, but are correlated with the near-surface region where the electric field is most sensitive to the boundary treatment.

The A/E distributions provide a complementary comparison of the simulated pulse shapes. Since A/E is related to the maximum current amplitude normalized by the deposited energy, it is sensitive to the time structure of the charge collection. In the PPC detector, reduced A/E values were observed close to the passivated surface in both frameworks. This is expected for surface events, where charge carriers may drift more slowly and the induced current is distributed over a longer time interval. The reduction is more visible in SSD, especially for zero and negative surface charge. This suggests that the effective surface-affected region is larger in SSD under the present simulation conditions. The activeness maps support this interpretation: reduced activeness near the passivated surface indicates incomplete charge collection, and the affected region extends further into the detector in SSD than in EH-Drift.

For the ICPC detector, the comparison led to a different conclusion. The electric field configurations obtained with SSD and EH-Drift are very similar, and no surface drift was observed in SSD. This is consistent with the ICPC geometry, where the field configuration guides charge carriers through the detector bulk rather than along the passivated surface. The simulated waveforms agree very well between the two frameworks, with residuals at the sub-percent level and uniformly small RMS values across the studied detector volume. The A/E distributions are nearly indistinguishable, and both frameworks predict values in a narrow range throughout the detector. The activeness is also close to one in both simulations, with only a small localized deviation near the passivated surface in EH-Drift.

The ICPC comparison is therefore consistent with the expectation that surface-related charge transport effects are much less relevant in this detector geometry than in PPC detectors. However, the study is limited by the fact that events could not be initialized arbitrarily close to the passivated surface in SSD. For such positions, parts of the simulated charge cloud could leave the detector volume within the first drift step, leading to artificial charge loss. These events were therefore not interpreted as physical surface events. At present, it is not clear whether this behaviour is caused by limitations in the way the ICPC surface configuration was implemented in SSD in this work, or by an issue in SSD itself. Consequently, the immediate vicinity of the passivated surface could not be fully probed.

Overall, the results show that SSD can reproduce the main qualitative features of passivated surface-event simulations known from EH-Drift. For PPC detectors, the agreement is good in the detector bulk, while significant differences remain close to the passivated surface. These differences are mainly attributed to the different treatment of boundary conditions and the resulting electric field configuration near the HPGe-LAr interface. For ICPC detectors, the agreement between the two frameworks is very good in all studied comparison metrics in the probed detector volume.

The results also show that the interpretation of surface-event simulations requires several observables. Waveform residuals provide a direct comparison of the simulated pulse shapes and are useful for identifying where the two frameworks disagree. The RMS of the residuals summarizes these differences spatially and highlights detector regions where the agreement is worse. The A/E parameter characterizes changes in the current-pulse amplitude and is therefore sensitive to slow charge collection. The activeness quantifies incomplete charge collection and identifies regions where energy degradation occurs. Taken together, these observables allow one to distinguish between differences in pulse shape, drift time, and total collected charge.

Several improvements could be pursued in future work. First, the treatment of boundary conditions in both frameworks should be investigated in more detail. In particular, a systematic study of the induced surface charge at dielectric interfaces and its dependence on detector geometry, bias voltage, and impurity profile would help to clarify the origin of the observed PPC differences. Second, the charge transport model near the passivated surface should be further validated, ideally using experimental surface-event data from calibration measurements. Such a comparison would make it possible to determine which boundary treatment more accurately describes real detector behaviour.

For ICPC detectors, future studies should focus on improving the numerical treatment of events initialized very close to the passivated surface. This could include smaller drift time steps, modified charge-cloud initialization, or a dedicated treatment of charge carriers close to detector boundaries. Such improvements would allow the immediate surface region to be studied more reliably. In addition, the comparison should be extended to more ICPC detectors with different geometries and impurity profiles to verify whether the weak surface sensitivity observed here is generally valid.

Finally, a comparison of the simulated surface-event observables to experimental data should be performed. Such a comparison is not straightforward for LEGEND physics data, since the interaction position of individual events is generally not known and events close to the passivated surface cannot be selected directly. A possible approach is to use α-induced events as a surface-enriched sample. Owing to the short range of α particles in germanium, events with reconstructed energies in the range 4 MeV $< E <$ 6 MeV can be attributed to interactions close to the detector surface, in particular near the p+ contact. However, the available statistics in the LEGEND physics data are limited. In the ICPC data set considered here, only one detector contains a sizeable sample, with 174 events in this energy region, while for PPC detectors only a few events per detector were found. This makes a quantitative validation of the surface-drift model using physics data alone difficult.

A more suitable strategy would therefore be to perform dedicated measurements in test stands using an external α source directed at well-defined detector surfaces. Such measurements would provide substantially higher statistics and better control over the interaction region. They would allow the simulated activeness, A/E distributions, waveform shapes, and drift-time behaviour to be compared directly to data. In this way, the surface-drift models implemented in SSD and EH-Drift could be validated and, if necessary, calibrated against experimental surface-event samples. This would be an important step toward using these simulations for reliable background modelling and pulse-shape-discrimination studies in LEGEND.

Bibliography

[1] M. E. Peskin. *Concepts of Elementary Particle Physics*. Oxford Master Series in Physics. Oxford University Press, Sept. 2019. ISBN: 978-0-19-881218-0. DOI: 10.1093/oso/9780198812180.001.0001.

[2] C. Giunti et al. *Fundamentals of Neutrino Physics and Astrophysics*. 2007. ISBN: 978-0-19-850871-7. DOI: 10.1093/acprof:oso/9780198508717.001.0001.

[3] I. Esteban et al. "NuFit-6.0: updated global analysis of three-flavor neutrino oscillations". In: *JHEP* 12 (2024), p. 216. DOI: 10.1007/JHEP12(2024)216. arXiv: 2410.05380 [hep-ph].

[4] K. Abe et al. "Constraint on the matter–antimatter symmetry-violating phase in neutrino oscillations". In: *Nature* 580.7803 (Apr. 2020), pp. 339–344. ISSN: 1476-4687. DOI: 10.1038/s41586-020-2177-0. URL: https://doi.org/10.1038/s41586-020-2177-0.

[5] J. A. Formaggio et al. "Direct measurements of neutrino mass". In: *Physics Reports* 914 (2021). Direct measurements of neutrino mass, pp. 1–54. ISSN: 0370-1573. DOI: https://doi.org/10.1016/j.physrep.2021.02.002. URL: https://www.sciencedirect.com/science/article/pii/S0370157321000636.

[6] M. Aker et al. "Direct neutrino-mass measurement based on 259 days of KATRIN data". In: *Science* 388.6743 (2025), adq9592. DOI: 10.1126/science.adq9592. arXiv: 2406.13516 [nucl-ex].

[7] P. Vogel et al. "Angular distribution of neutron inverse beta decay, $\overline{\nu}_e + \vec{p}\ e^+ + n$". In: *Phys. Rev. D* 60 (5 July 1999), p. 053003. DOI: 10.1103/PhysRevD.60.053003. URL: https://link.aps.org/doi/10.1103/PhysRevD.60.053003.

[8] D. Akimov et al. "Observation of coherent elastic neutrino-nucleus scattering". In: *Science* 357.6356 (2017), pp. 1123–1126. DOI: 10.1126/science.aao0990. eprint: https://www.science.org/doi/pdf/10.1126/science.aao0990. URL: https://www.science.org/doi/abs/10.1126/science.aao0990.

[9] E. Aprile et al. "First Indication of Solar ^{8}B Neutrinos via Coherent Elastic Neutrino-Nucleus Scattering with XENONnT". In: *Phys. Rev. Lett.* 133 (19 Nov. 2024), p. 191002. DOI: 10.1103/PhysRevLett.133.191002. URL: https://link.aps.org/doi/10.1103/PhysRevLett.133.191002.

[10] G. C. Branco et al. "Building the full Pontecorvo-Maki-Nakagawa-Sakata matrix from six independent Majorana-type phases". In: *Phys. Rev. D* 79 (1 Jan. 2009), p. 013001. DOI: 10.1103/PhysRevD.79.013001. URL: https://link.aps.org/doi/10.1103/PhysRevD.79.013001.

[11] R. Saakyan. "Two-Neutrino Double-Beta Decay". In: *Annual Review of Nuclear and Particle Science* 63 (Oct. 2013), pp. 503–529. DOI: 10.1146/annurev-nucl-102711-094904.

[12] M. Agostini et al. "Final Results of GERDA on the Two-Neutrino Double-β Decay Half-Life of Ge76". In: *Phys. Rev. Lett.* 131.14 (2023), p. 142501. DOI: 10.1103/PhysRevLett.131.142501. arXiv: 2308.09795 [nucl-ex].

[13] J. Schechter et al. "Neutrinoless double-β decay in SU(2)×U(1) theories". In: *Phys. Rev. D* 25 (11 June 1982), pp. 2951–2954. DOI: 10.1103/PhysRevD.25.2951. URL: https://link.aps.org/doi/10.1103/PhysRevD.25.2951.

[14] M. Hirsch et al. "Double beta decay in left-right symmetric models". In: *Phys. Lett. B* 374 (1996), pp. 7–12. DOI: 10.1016/0370-2693(96)00185-2. arXiv: hep-ph/9602306.

[15] V. Brdar et al. "Low scale left-right symmetry and naturally small neutrino mass". In: *Journal of High Energy Physics* 2019.2 (2019), p. 45. ISSN: 1029-8479. DOI: 10.1007/JHEP02(2019)045. URL: https://doi.org/10.1007/JHEP02(2019)045.

[16] J. Chakrabortty et al. "Neutrinoless double-β decay in TeV scale left-right symmetric models". In: *Journal of High Energy Physics* 2012.8 (2012), p. 8. ISSN: 1029-8479. DOI: 10.1007/JHEP08(2012)008. URL: https://doi.org/10.1007/JHEP08(2012)008.

[17] Particle Data Group. "Neutrinoless Double-Beta Decay". In: *Prog. Theor. Exp. Phys.* 2022 (2022), p. 083C01.

[18] A. Giuliani et al. "Double Beta Decay APPEC Committee Report". In: (Oct. 2019). arXiv: 1910.04688 [hep-ex].

[19] M. Macko. "The SuperNEMO Demonstrator: a unique technology for high-precision measurements of $\beta\beta$-decay modes". In: *PoS* EPS-HEP2025 (2026), p. 175. DOI: 10.22323/1.485.0175.

[20] I. J. Arnquist et al. "Final Result of the Majorana Demonstrator's Search for Neutrinoless Double-β Decay in ^{76}Ge". In: *Phys. Rev. Lett.* 130 (6 Feb. 2023), p. 062501. DOI: 10.1103/PhysRevLett.130.062501. URL: https://link.aps.org/doi/10.1103/PhysRevLett.130.062501.

[21] G. Anton et al. "Search for Neutrinoless Double-β Decay with the Complete EXO-200 Dataset". In: *Phys. Rev. Lett.* 123 (16 Oct. 2019), p. 161802. DOI: 10.1103/PhysRevLett.123.161802. URL: https://link.aps.org/doi/10.1103/PhysRevLett.123.161802.

[22] A. Gando et al. "Limit on Neutrinoless $\beta\beta$ Decay of ^{136}Xe from the First Phase of KamLAND-Zen and Comparison with the Positive Claim in ^{76}Ge". In: *Phys. Rev. Lett.* 110 (6 Feb. 2013), p. 062502. DOI: 10.1103/PhysRevLett.110.062502. URL: https://link.aps.org/doi/10.1103/PhysRevLett.110.062502.

[23] D. Q. Adams et al. "Improved Limit on Neutrinoless Double-Beta Decay in ^{130}Te with CUORE". In: *Phys. Rev. Lett.* 124 (12 Mar. 2020), p. 122501. DOI: 10.1103/PhysRevLett.124.122501. URL: https://link.aps.org/doi/10.1103/PhysRevLett.124.122501.

[24] C. Ransom. "Energy Calibration for the Gerda and Legend-200 Experiments". PhD thesis. Universität Zürich, 2021.

[25] P. Krause. *CAD renderings*. Internal documentation. 2024.

[26] R. Deckert. *Optical Modeling Results from In-situ Characterization Data*. Internal presentation, Technical University of Munich (TUM), LEGEND collaboration. 2026.

[27] N. Burlac. "Early results of the LEGEND-200 experiment". In: *Nuclear Instruments and Methods in Physics Research Section A: Accelerators, Spectrometers, Detectors and Associated Equipment* 1080 (2025), p. 170779. ISSN: 0168-9002. DOI: https://doi.org/10.1016/j.nima.2025.170779. URL: https://www.sciencedirect.com/science/article/pii/S0168900225005807.

[28] C. Romo-Luque. *Results of the LEGEND-200 experiment in the search for neutrinoless double beta decay*. Aug. 2025. DOI: 10.48550/arXiv.2508.18573.

[29] M. Agostini et al. "Pulse shape analysis in Gerda Phase II". In: *The European Physical Journal C* 82.4 (Apr. 2022), p. 284. ISSN: 1434-6052. DOI: 10.1140/epjc/s10052-022-10163-w. URL: https://doi.org/10.1140/epjc/s10052-022-10163-w.

[30] G. Müller et al. "Crystal Growth, Bulk: Methods". In: *Encyclopedia of Condensed Matter Physics*. Ed. by F. Bassani et al. Oxford: Elsevier, 2005, pp. 262–274. ISBN: 978-0-12-369401-0. DOI: https://doi.org/10.1016/B0-12-369401-9/00416-2. URL: https://www.sciencedirect.com/science/article/pii/B0123694019004162.

[31] K. Momma et al. "*VESTA3* for three-dimensional visualization of crystal, volumetric and morphology data". In: *Journal of Applied Crystallography* 44.6 (Dec. 2011), pp. 1272–1276. DOI: 10.1107/S0021889811038970. URL: https://doi.org/10.1107/S0021889811038970.

[32] Y. P. Varshni. "Temperature dependence of the energy gap in semiconductors". In: *Physica* 34.1 (1967), pp. 149–154. DOI: 10.1016/0031-8914(67)90062-6.

[33] Ioffe Institute. *Band structure and carrier concentration of Germanium (Ge)*. https://www.ioffe.ru/SVA/NSM/Semicond/Ge/bandstr.html. Accessed: 2026-06-25.

[34] H. Spieler. *Semiconductor Detector Systems*. Oxford University Press, 2005.

[35] Z. He. "Review of the Shockley–Ramo theorem and its application in semiconductor gamma-ray detectors". In: *Nuclear Instruments and Methods in Physics Research Section A: Accelerators, Spectrometers, Detectors and Associated Equipment* 463.1 (2001), pp. 250–267. ISSN: 0168-9002. DOI: https://doi.org/10.1016/S0168-9002(01)00223-6. URL: https://www.sciencedirect.com/science/article/pii/S0168900201002236.

[36] M. Ballester et al. "Charge Diffusion and Repulsion in Semiconductor Detectors". In: *Sensors* 24.22 (2024). ISSN: 1424-8220. DOI: 10.3390/s24227123. URL: https://www.mdpi.com/1424-8220/24/22/7123.

[37] L. Mihailescu et al. "The influence of anisotropic electron drift velocity on the signal shapes of closed-end HPGe detectors". In: *Nuclear Instruments and Methods in Physics Research Section A: Accelerators, Spectrometers, Detectors and Associated Equipment* 447.3 (2000), pp. 350–360. ISSN: 0168-9002. DOI: https://doi.org/10.1016/S0168-9002(99)01286-3. URL: https://www.sciencedirect.com/science/article/pii/S0168900299012863.

[38] D. Caughey et al. "Carrier mobilities in silicon empirically related to doping and field". In: *Proceedings of the IEEE* 55.12 (1967), pp. 2192–2193. DOI: 10.1109/PROC.1967.6123.

[39] B. Bruyneel et al. "Characterization of large volume HPGe detectors. Part I: Electron and hole mobility parameterization". In: *Nuclear Instruments and Methods in Physics Research Section A: Accelerators, Spectrometers, Detectors and Associated Equipment* 569.3 (2006), pp. 764–773. ISSN: 0168-9002. DOI: https://doi.org/10.1016/j.nima.2006.08.130. URL: https://www.sciencedirect.com/science/article/pii/S0168900206015166.

[40] D. A. Neamen. *Semiconductor Physics and Devices: Basic Principles*. 4th ed. McGraw-Hill, 2012. ISBN: 9780073529585.

[41] E. Gatti et al. "Dynamics of electrons in drift detectors". In: *Nuclear Instruments and Methods in Physics Research Section A: Accelerators, Spectrometers, Detectors and Associated Equipment* 253.3 (1987), pp. 393–399. ISSN: 0168-9002. DOI: https://doi.org/10.1016/0168-9002(87)90522-5. URL: https://www.sciencedirect.com/science/article/pii/0168900287905225.

[42] H. Mei et al. "The impact of neutral impurity concentration on charge drift mobility in n-type germanium". In: *Journal of Instrumentation* 12.07 (July 2017), P07003. DOI: 10.1088/1748-0221/12/07/P07003. URL: https://doi.org/10.1088/1748-0221/12/07/P07003.

[43] S. E. Boggs et al. "Numerical simulations of charge trapping in germanium strip detectors". In: *Nuclear Instruments and Methods in Physics Research Section A: Accelerators, Spectrometers, Detectors and Associated Equipment* 1057 (2023), p. 168756. ISSN: 0168-9002. DOI: https://doi.org/10.1016/j.nima.2023.168756. URL: https://www.sciencedirect.com/science/article/pii/S0168900223007477.

[44] M. Willers. *Workshop: HPGe electronics chain in LEGEND-200.* Internal presentation, Technical University of Munich (TUM) / Max Planck Institute (MPIK), LEGEND collaboration. 2024.

[45] M. Willers. "Signal Readout Electronics for LEGEND-200". In: *Journal of Physics: Conference Series* 1468 (2020), p. 012113. DOI: 10.1088/1742-6596/1468/1/012113. arXiv: 1911.05847 [physics.ins-det].

[46] H. Acharya et al. "Energy Calibration and Performance of HPGe Detectors in the LEGEND-200 Experiment". In: (May 2026). arXiv: 2605.22479 [physics.ins-det].

[47] L. Baudis et al. "Calibration sources for the LEGEND-200 experiment". In: *Journal of Instrumentation* 18.02 (Feb. 2023), P02001. DOI: 10.1088/1748-0221/18/02/P02001. URL: https://doi.org/10.1088/1748-0221/18/02/P02001.

[48] M. Agostini et al. "Final Results of GERDA on the Search for Neutrinoless Double-β Decay". In: *Phys. Rev. Lett.* 125 (25 Dec. 2020), p. 252502. DOI: 10.1103/PhysRevLett.125.252502. URL: https://link.aps.org/doi/10.1103/PhysRevLett.125.252502.

[49] S. Calgaro et al. *Background analysis for LEGEND-200 data release at Neutrino 2024.* LEGEND Note 24-007. Draft, internal use only. LEGEND Collaboration, 2025.

[50] C. Wiesinger et al. "Virtual depth by active background suppression: revisiting the cosmic muon induced background of GERDA Phase II". In: *The European Physical Journal C* 78 (2018), p. 597. DOI: 10.1140/epjc/s10052-018-6079-3. arXiv: 1802.05040 [physics.ins-det].

[51] Korea Atomic Energy Research Institute. *Table of Nuclides: Polonium-210.* https://atom.kaeri.re.kr/cgi-bin/nuclide?nuc=Po210. Accessed: 2026-06-24.

[52] G. Knoll. *Radiation Detection and Measurement (4th ed.)* Hoboken, NJ: John Wiley, 2010. ISBN: 978-0-470-13148-0.

[53] Particle Data Group. *Atomic and Nuclear Properties of Materials: Germanium (Ge).* 2010. URL: https://pdg.ge.infn.it/2010/AtomicNuclearProperties/HTML_PAGES/032.html (visited on 02/18/2026).

[54] J. Gruszko. "Surface Alpha Interactions in P-Type Point-Contact HPGe Detectors: Maximizing Sensitivity of ^{76}Ge Neutrinoless Double-Beta Decay Searches". PhD thesis. University of Washington, 2017.

[55] I. Abt et al. "Simulation of semiconductor detectors in 3D with SolidStateDetectors.jl". In: *Journal of Instrumentation* 16.08 (Aug. 2021), P08007. DOI: 10.1088/1748-0221/16/08/p08007. URL: https://doi.org/10.1088/1748-0221/16/08/p08007.

[56] K. H. Bhimani. "Advances in Germanium Detector Signal Modeling with GPU Computing and Deep Learning Techniques". PhD thesis. University of North Carolina at Chapel Hill, 2025.

[57] F. Hagemann. "Determination of the impurity density profile and charge carrier mobilities in a point-contact germanium detector using a novel Compton Scanner". PhD thesis. Technische Universität München, 2024.

[58] E. P. Bernard et al. “Thermodynamic stability of xenon-doped liquid argon detectors”. In: *Phys. Rev. C* 108 (4 Oct. 2023), p. 045503. DOI: 10.1103/PhysRevC.108.045503. URL: https://link.aps.org/doi/10.1103/PhysRevC.108.045503.

[59] T. G. Castner et al. “The low-frequency, low-temperature dielectric behavior of n-type germanium below the insulator-metal transition”. In: *Journal of Low Temperature Physics* 38.3 (Feb. 1980), pp. 447–473. ISSN: 1573-7357. DOI: 10.1007/BF00114337. URL: https://doi.org/10.1007/BF00114337.

Appendix

Passivated surface events PPC

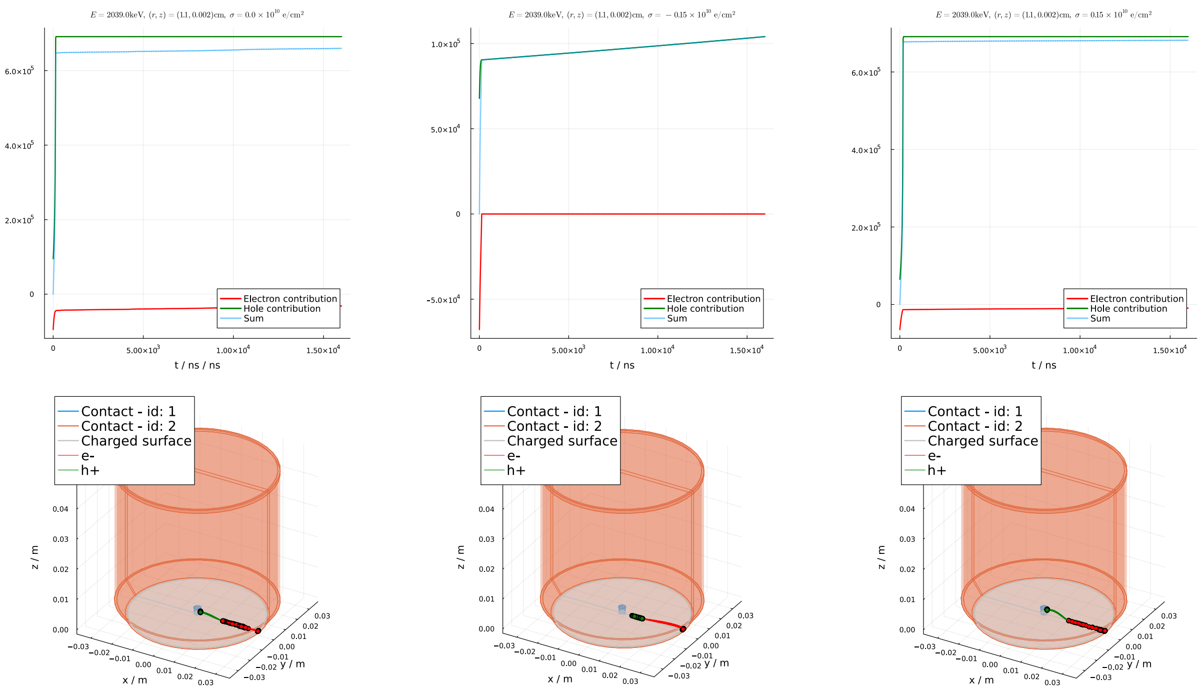

Figure 7.1: Electron and hole components of simulated passivated surface events in a PPC detector (P00698A), with their corresponding trajectories. For $\sigma = 0$ (left) electrons drift partially through the passivated surface, slightly reducing the signal. For $\sigma < 0$ (middle) holes, which dominate the signal, drift through the passivated surface, strongly degrading the signal. For $\sigma > 0$ (right) electrons drift through the passivated surface, but only slightly degrading the signal due to their relatively weak contribution. The drift velocity is reduced by a factor of 1000 inside the passivated region.

Results for $\sigma > 0$ in PPC detector

Waveform residuals

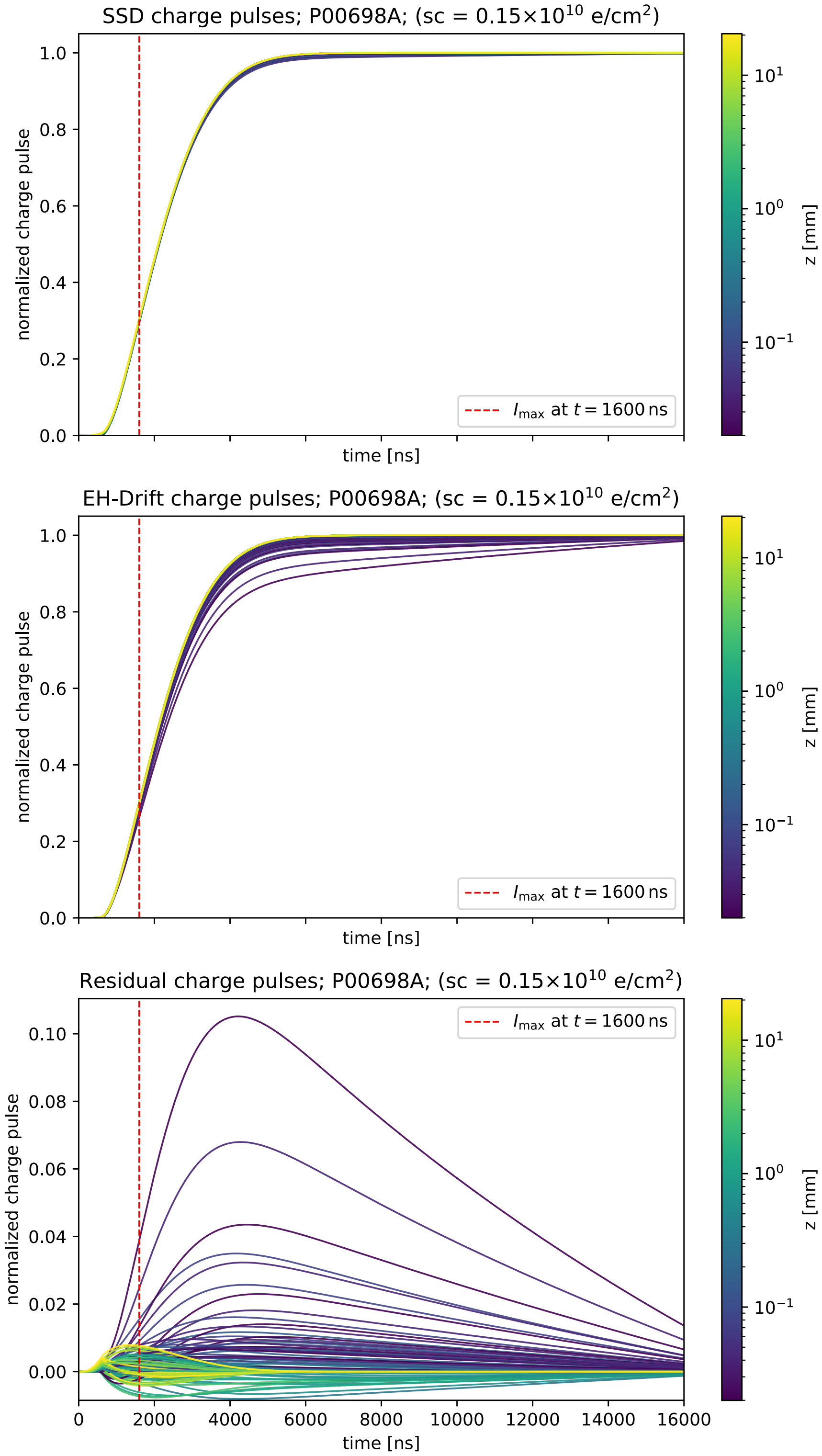

Figure 7.2: Charge pulses of identical events simulated with SSD and EH-Drift, and their residuals

RMS map

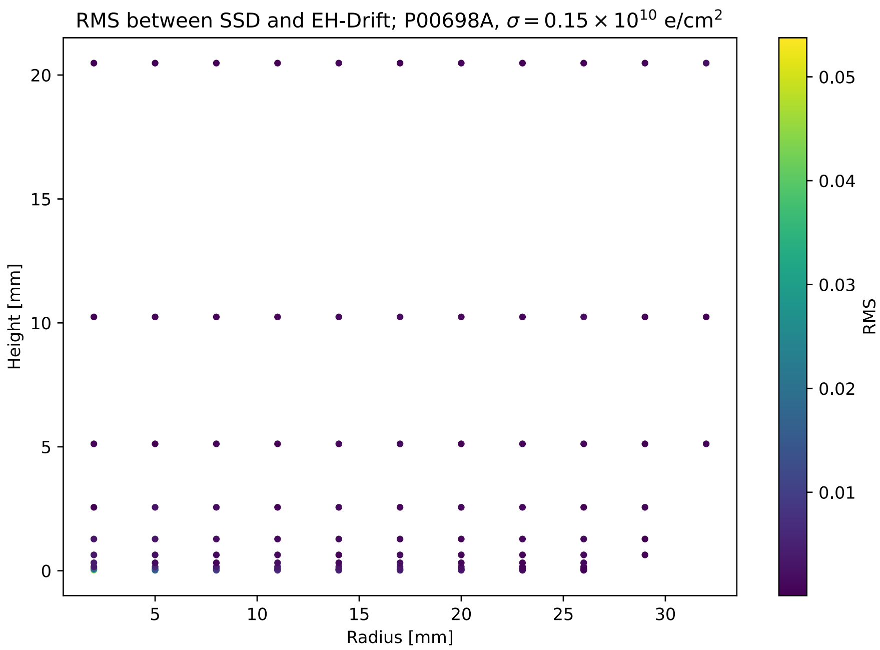

Figure 7.3: RMS map between SSD and EH-Drift for a PPC detector (P00698A) for positive surface charge.

A/E map

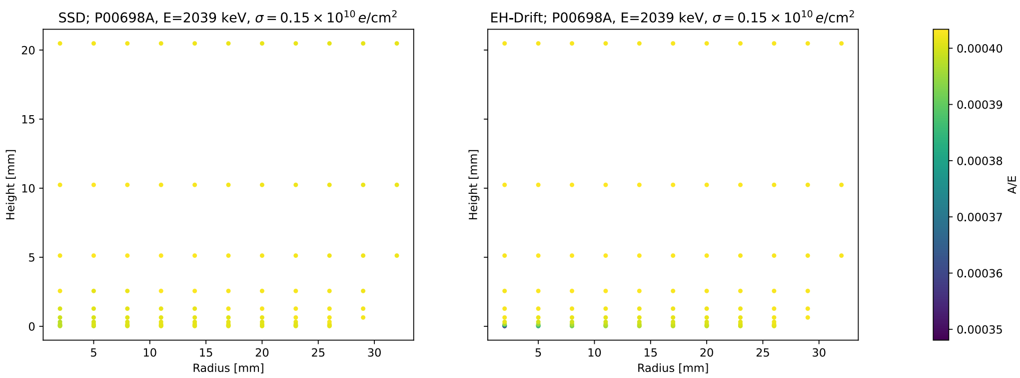

Figure 7.4: A/E values of waveforms simulated by SSD (top) and EH-Drift (bottom) for detector coordinates near the passivated surface and across the bulk, with positive surface charge.

Activeness

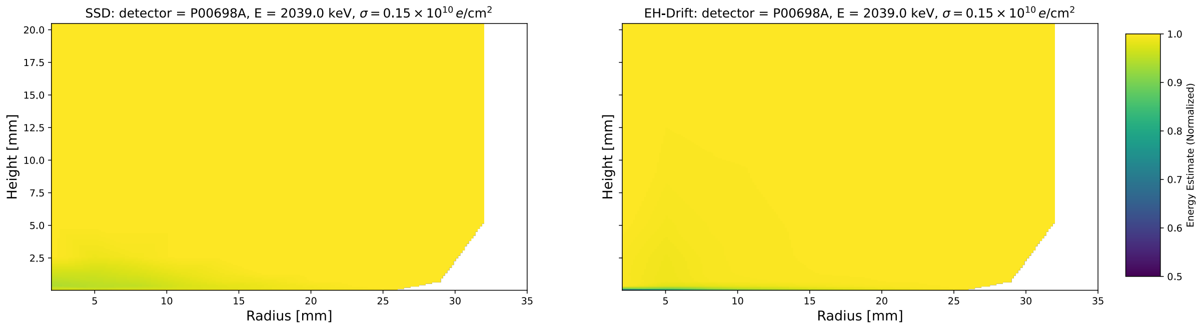

Figure 7.5: Interpolated activeness map for a PPC detector (P00698A) for positive surface charge.